

Study of dendritic spine compartmentalization.
A correlative fluorescence light microscopy-electron
microscopy approach.

Inauguraldissertation

zur
Erlangung der Würde eines Doktors der Philosophie
vorgelegt der
Philosophisch-Naturwissenschaftlichen Fakultät
der Universität Basel
von

Cyprien Vivien
Aus Flers, France

Basel, 2014



Original document stored on the publication server of the University of Basel (edoc.unibas.ch).
This work is licenced under the agreement "Attribution Non-Commercial
No Derivatives –2.5Switzerland". The complete text may be viewed at
<http://www.creativecommons.org/licenses/by-nc-nd/2.5/ch/deed.en>

Genehmigt von der Philosophisch-Naturwissenschaftlichen Fakultät

Auf Antrag von:

Prof. Dr. Peter Scheiffele

Prof. Dr. Michael Frotscher

Prof. Dr. Thomas Oertner

Basel, den 21. Februar 2012

Prof. Dr. Martin Spiess

Dekan

Table of contents

Summary	4
I. Introduction	7
A. Hippocampus.	7
B. Pyramidal neurons	9
C. Synapses.....	10
1. Structure	10
2. Synaptic plasticity	11
D. Dendritic spine.	12
1. Structure	12
a) Postsynaptic density	13
b) Cytoskeleton.	15
c) Organelles.	15
d) Spine geometry and synaptic function.	17
2. Compartmentalization.....	19
a) Spines act as chemical compartments.....	20
b) Spines act as electrical compartments.	23
II. Aim of the Thesis	25
III. Methods	26
A. Slice culture.....	26
B. Plasmid construct and transfection	27
C. Two-photon imaging.....	29
1. Experimental setup.....	31
2. Electrophysiology	32
3. Image acquisition and analysis	32
a) Measurement of coupling between dendritic spine and its parent's dendrite.	32
b) Measurement of coefficient of diffusion in dendrites.	34

c)	Estimation of spine volume.	34
D.	Serial block face scanning electron microscope.	35
E.	Correlative microscopy	36
1.	Recovery of the previously imaged neuron by DAB staining	37
2.	Embedding.....	38
3.	Recovery of previously imaged spines in the SBFSEM.	38
4.	Imaging and image analysis.....	40
F.	Estimation of spine neck resistance.	42
G.	Computation of Digitally Reconstructed Fluorescence Images (DRFI)	42
1.	Reconstruction of geometrical structures.....	43
2.	Computation of synthetic PSF	43
3.	Convolution	44
4.	Measurements of Spine Intensity in 2-Photon Images and DRFI.....	45
H.	Statistical analysis.	47
IV.	Results.....	48
A.	Direct measurement of coupling between dendritic spines and dendrites.....	48
B.	Correlative microscopy	50
C.	Analysis of ultrastructural reconstruction of dendritic spines in CA1 pyramidal neurons.	52
D.	Dendritic spine morphology predicts alexa diffusion out of the spine.	55
E.	Movements of larger and positively charged molecules are also slowed down inside spines.	60
F.	Estimation of dendritic spine neck resistance.	65
G.	Dendritic spines act as molecular enrichment devices.	67
H.	Activity induced change in diffusion.....	69
V.	Discussion.....	72
A.	Diffusion of molecules is slowed down inside dendritic spines.	72
B.	The controversy about spine neck resistance.	74

C. Dendritic spines possess a size filter.....	75
D. Dendritic spines concentrate particles.	76
E. Activity induced changes in diffusion speed.....	76
VI. Annexe	79
VII. References.....	86
VIII. List of abbreviations:	94
IX. Table of figures.....	95
X. Acknowledgments	97
XI. Curriculum vitae	98

Summary

Neurons communicate with each other through synapses. Most excitatory synapses contact small protrusions called dendritic spines. Spines are connected to dendrites by a very thin stalk called the “spine neck” which restricts diffusion between the spine head and its parent dendrite. In consequence, dendritic spines form biochemical micro-compartments. Compartmentalization inside spines is thought to be important for synaptic function, since strong compartmentalization could influence concentration of activated molecules close to synapses during repetitive synaptic stimulations, and also increase depolarization in spine heads. But it is not fully understood how and to what extent spines compartmentalize biochemical signalings.

With two-photon microscopy we measured diffusion coupling between spine heads and parent dendrites of CA1 pyramidal neurons using fluorescence recovery after photobleaching of Alexa dye. Since dendritic spines are below the diffraction limit of light microscopy, it is not possible to measure their detailed morphology with two-photon microscopy. To investigate how spines ultrastructure regulates diffusional coupling to the dendrite, we needed informations about diffusion time constant and spine morphology from the same spine.

We developed a correlative (two-photon microscopy / electron microscopy) approach to reconstruct the precise morphology of dendritic spines where diffusional coupling measurements took place. We found that the outer shape of dendritic spines predicts the diffusional coupling of small molecules. However their diffusional speed in the cytoplasm of spines is 5 times slower than in dendrites. The impact of dendritic spines on electrical compartmentalization depends on spine neck resistance. There is a controversy between studies focusing on dendritic spines morphology (low neck resistance estimates) and studies focusing on synaptic physiology (high neck resistance estimates). All estimates from morphology rested on the assumption that the cytoplasm inside spines and dendrites has homogenous diffusional properties and thus the same resistivity. Here we show that this assumption is not correct. In consequence, we estimate that spine necks resistance approaches 1 G Ω in some spines, sufficiently high to compartmentalize electrical signals.

For the correlative experiments we used Alexa, a small molecule (1 kDa) roughly the size of ATP or GTP. We were also interested to see if larger molecules like calmodulin (16 kDa) or PKA (38 kDa) behave in the same way. In contrast to Alexa, we found that the diffusional coupling of PA-GFP (27 kDa) and Dextran (70 kDa) could not be predicted from spine shapes. Thus, in addition to the high viscosity of the cytoplasm in all spines, some spines seem to contain an additional size filter that selectively blocks the diffusion of larger molecules. This filter might be important in regulating metaplasticity.

Theoretically, dye particles and other molecules should concentrate in high viscosity compartments. We tested this prediction by creating synthetic images based on 3D reconstructions from our EM data. Indeed, we found that spines appear too bright in the two photon images. Thus, the differences in diffusion speed between spines and dendrites result in different particles densities, making dendritic spines 'protein enrichment devices'. Finally, we found that the coefficient of diffusion in the cytoplasm is not a static value, but that the viscosity of the entire neuron increases in response to strong depolarization. In summary, dendritic spines appear to be even more complex than previously thought, as we found a new function and a new level of regulation in their functionality. In the light of our findings, the disagreement of previous estimates of spine neck resistance can be readily explained by local differences in cytoplasmic viscosity.

I. Introduction

The brain is composed of billions of interconnected cells organized in a very complex structure. Inputs are received from the environment and process to induce a response. Previous experiences can induce a more appropriated response; this ability is called learning and memory. Despite an explosion of scientific discoveries from the level of animal behaviors to the structure of single molecules, we barely start to understand how such a process is driven.

The brain is composed mainly of two types of cells: 90 % of glia cells and 10 % of neurons. Glia cells provide, support, nutrients and oxygen to neurons, insulate axons and also drive the brain immune response. Although it was though for a long time that glia cells do not play a role in the process and transmission of information, this idea is challenged by new discoveries showing that they do modulate neurotransmission (Parpura, Basarsky et al. 1994) (Yang, Ge et al. 2003). Neurons in the other hand accomplish the main activity of the brain: Processing of information through ensembles of neurons organized into neuronal networks is believed to drive behavior.

Information transmits through synapses which are very specialized structures located at the junction points between neurons. It has been shown that information transmission through synapses can be regulated by previous activity. This process called synaptic plasticity has been proposed as a mechanism to mediate learning and memory. One neuron can carry as much as 10 000 synapses and each synapse can be regulated independently and act as a single unit, increasing the computational power of the brain. Neurons have developed dendritic spines where synapses are located, most probably to establish synaptic independence, but it is not clear to what degree spines isolate synapses.

A. Hippocampus.

To investigate the compartmentalization of dendritic spines, we used a highly studied structure as a model system, the hippocampus. It is part of the forebrain and located in the medial temporal lobe and has been shown to play a central role in memory storage and spatial navigation (Rempel-Clower, Zola et al. 1996; Reed and Squire 1997; Milani, Uemura et al. 1998; Neves, Cooke et al. 2008). It is a highly organized network and it

is anatomically divided into several sub regions; CA1, CA2, CA3, dentate gyrus, subiculum, parasubiculum, perisubiculum, and entorhinal cortex.

The hippocampus has three major excitatory pathways running from the subiculum to the CA1 region. The perforant pathway runs from the subiculum to the granule cells of the dentate gyrus. The axons of the granule cells form a bundle, the mossy fiber pathway that runs to the pyramidal cells lying in the CA3 region of the hippocampus. The pyramidal cells in the CA3 regions send excitatory collaterals, to CA1 pyramidal cells through the Schaffer collateral or the commissural pathway. CA1 projections run outside the hippocampus, through subiculum and entorhinal cortex to several cortical and subcortical areas (Amaral and Witter 1989) (**Figure I-1**).

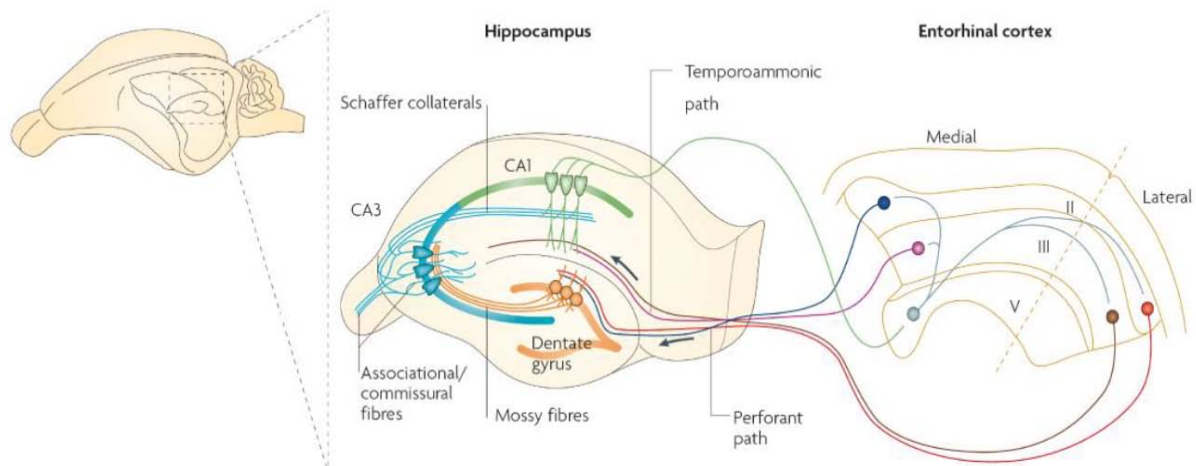


Figure I-1: The anatomy of the hippocampus.

Sensory information collected by neocortical areas is conveyed to the Entorhinal cortex, which is divided into different layers (here displayed are layers II, III and V). Each layer projects via the perforant path to a different subregion in the hippocampus. Direct projections terminate in the dentate gyrus, area CA3 and area CA1. From (Neves, Cooke et al. 2008)

Thanks to its highly organized structure, the hippocampus is an excellent system to study synaptic physiology. At the dentate gyrus was described for the first time synaptic plasticity (Bliss and Lomo 1973) and most of the studies in the decades that followed its original description have focused on the CA1 region. Nowadays a wealth of structural, histological, and physiological information is available for hippocampal CA1 pyramidal neurons.

B. Pyramidal neurons

Neurons are the functional block of the brain. They receive, process, transmit information through form of electrical activity. Neurons can be classified into many different types depending on their locations and functions, but they all share the same basic architecture. They are composed of three different elements:

- the soma or cell body where the nucleus and most organelles for protein synthesis are located
- dendrites are cellular processes with a tree-like branched structure where information is received.
- the axon is a fine, cable-like process where information is transmitted to postsynaptic cells. Axons can project over long distances to other parts of the brain.

CA1 pyramidal neurons possess two branching dendritic structures which emerge from the soma. The basal dendrites occupy the *stratum oriens*, the apical dendrites occupy the *stratum radiatum* (proximal apical) and the *stratum lacunosum-moleculare* (distal apical)Figure I-2.

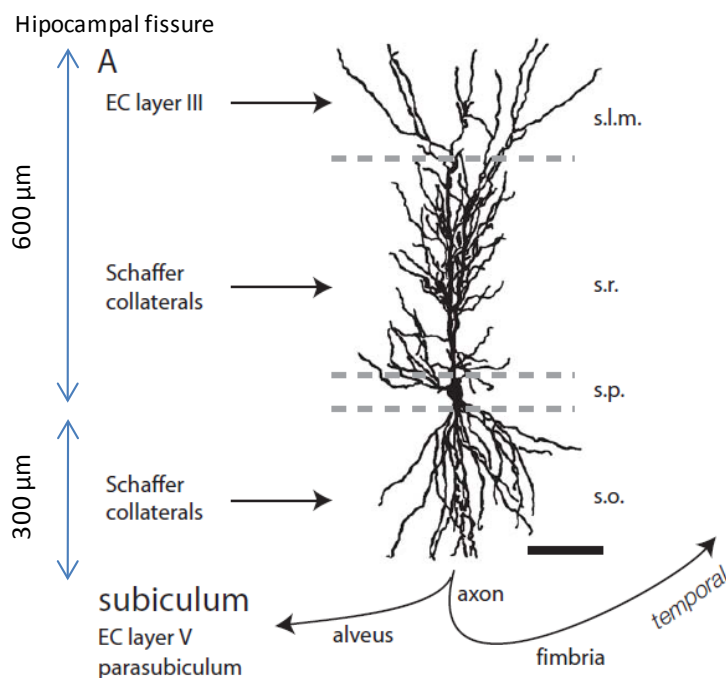


Figure I-2. CA1 pyramidal cell. CA1 pyramidal neurons dendritic tree is represented. The cell body is in the *stratum pyramidale* (s.p), basal dendrites in the *stratum oriens* (s.o) and apical dendrites in the *stratum radiatum* (s.r) and *stratum lacunosum-moleculare* (s.l.m) The major excitatory inputs in each layers and the major outputs are also indicated. Adapted from(Bannister and Larkman 1995).

In this study we focused on dendritic spines receiving synaptic input from the Schaffer collaterals on apical dendrites.

C. Synapses

1. Structure

There are two types of synapses, electrical and chemical.

Electrical synapses, also known as gap junctions consist of arrays of intercellular channels composed of integral membrane proteins called connexins in vertebrates, creating an electrical coupling between both neurons. Gap junction channels regulate the passage of ions and biological molecules between adjacent cells (Maeda and Tsukihara 2011). These synapses are rare among principal neurons (e.g., pyramidal neurons).

Most information is transmitted through chemical synapses. They are composed of three elements (**Figure I-3**):

- The pre synaptic element, called bouton, is a specialized area within the axon which contains neurotransmitters enclosed in small membrane-spheres called synaptic vesicles.
- the synaptic cleft is a widening of the space between the neurons membranes where the neurotransmitter is released and diffuse to bind to receptors located on the postsynaptic membrane.
- The postsynaptic element includes receptors where the neurotransmitter binds but also a postsynaptic density which is an aggregate of proteins important for the functionality of the synapse. Most receptors are ionotropic receptors. Their opening leads to an influx or efflux of ions, changing the transmembrane potential. Depending of the type of ions the flux can depolarize or hyperpolarize locally the inside of the neuron leading to an excitatory or inhibitory effect called excitatory or inhibitory postsynaptic potentials (EPSP, IPSP).

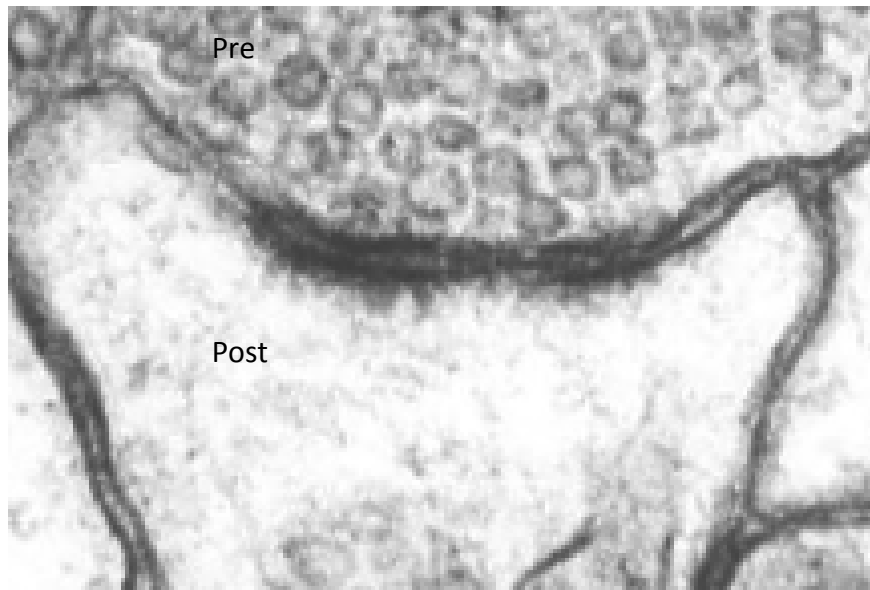


Figure I-3:Chemical synapse

Presynaptic terminal (pre) contains synaptic vesicles, a postsynaptic density appears postsynaptically (post). The synaptic clef contains also grey filamentous material (from <http://synapses.clm.utexas.edu>).

Synaptic potentials will propagate until the soma where they will be integrated at the level of the initial segment at the axon. If the integrated signal reaches the spiking threshold then an action potential (AP) is initiated and actively transmitted along the axon. The AP will also back propagate (bAP) along the dendrites and give a feedback to the synapse about the output status of the neuron.

2. Synaptic plasticity

During an EPSP calcium (Ca^{2+}) permeable channels open, leading to an increase of Ca^{2+} in the spine associated with the postsynapse. Pairing of postsynaptic bAPs with synaptic EPSP generates supralinear Ca^{2+} signals when the EPSP precedes the bAP and sublinear signals when the timing is reversed (Bloodgood and Sabatini 2007). Coincidence of postsynaptic bAPs and EPSPs and in consequence elevated calcium levels are crucial for regulation of synaptic efficiency (Markram, Lubke et al. 1997). Long-term potentiation and long-term depression are long lasting activity dependent changes in synaptic strength that are thought to be cellular and molecular mechanisms of memory formation and storage.

D. Dendritic spine.

Most excitatory synapses do not occur directly on dendrites but are located on small protrusions of it called spines (Gray 1959). Although they were discovered one century ago by Ramon y Cajal, their role is not fully understood. Many roles have been proposed for this tiny structure. Ramon y Cajal thought that spines connect axon and dendrite because spines would increase the amount of dendritic membrane available for synaptic contacts, similar to how intestinal villi increase the absorbance surface in the digestive system. This theory is now disregarded because there are almost no synaptic contacts directly on dendrites (Harris and Stevens 1989). Spine could also increase the connectivity between neurons. Dendrites could connect with more axon terminals than without spines by providing a wider selection of axons available to a dendrite to make synaptogenesis more selective (Stepanyants, Hof et al. 2002). This design would improve the wiring of a neuronal circuit, as axons could course through the nervous system in straight trajectories. The main hypothesis for the role of dendritic spines is that they act as biochemical compartments. Synapses on spines could be regulated independently and individual synapse could act as basic functional units of neuronal integration. In the following, I will list some evidence in favor of this hypothesis.

1. Structure

In pyramidal neurons spines typically consist of a bulbous head connected to the dendrite by a thin stalk called the 'spine neck'. Dendritic spines exist in a huge variety of shapes and sizes. The head can be spherical, cups shaped or completely irregular. The neck can be cylindrical, irregular, straight or bent. There is also a huge variety in size. Electron microscopy provided fine details of the morphology. Spine head volume ranges from 0.004 to 0.6 μm^3 with a diverse variety of shape. The narrow necks range in length from 0.08 to 1.58 μm and from 0.0038 to 0.46 μm in diameter (Harris and Stevens 1989). This huge variety can be found along a very short dendritic segment (**Figure I-4**).

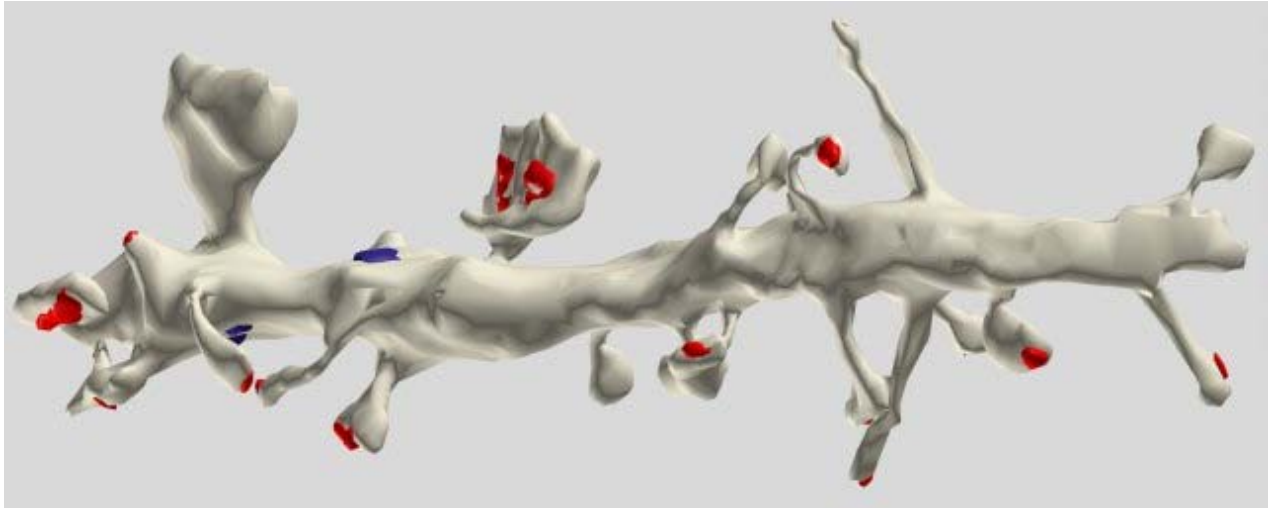


Figure I-4 3D reconstruction of dendrite from CA1 pyramidal cell.

A segment of pyramidal cell dendrite from *stratum radiatum* (CA1) with thin, stubby, and mushroom-shaped spines. Spines synapses colored in red, stem (or shaft) synapses colored in blue. (from <http://synapses.clm.utexas.edu>)

Typically, each dendritic spine carries the postsynaptic element of a single excitatory synapse. The head can be seen as a minimal cytoplasmic volume associated with the synapse; it contains neurotransmitter receptors and associated signaling proteins, as well as cytoskeletal elements. Organelles involved in protein synthesis, membrane trafficking and calcium metabolism are also present. Spines possess the entire molecular machinery indispensable for a proper functioning of the synapse.

a) Postsynaptic density

The postsynaptic density (PSD) is an electron dense thickening located at the membrane opposed to the location where synaptic vesicles are released, the active zone. The PSD of an excitatory synapse contains ionotropic and metabotropic glutamate receptors as well as voltage dependent channels. It contains also a variety of receptor tyrosine kinases and cell adhesion molecules which mediate a physical or communication link between the pre and post synaptic elements. At hippocampal Schaffer collateral synapses, the main glutamate receptors are α -amino-3-hydroxy-5-methyl-4-isoxazolepropionate (AMPA), N-methyl-D-aspartic acid (NMDA) and metabotropic receptors (Walikonis, Jensen et al. 2000).

AMPA is a heterotetrameric receptor made of the subunit GluR1-4 (Mayer 2011). These receptors carry the main electrical charges transfer at the synapse during synaptic transmission. Release of glutamate from the presynaptic element and binding to AMPA

receptors induces a rapid inward current of K⁺ and Na⁺. AMPA receptors lacking a GluR2 subunit are impermeable to calcium, but in CA1 pyramidal cell most of AMPA receptor contain GluR2 (Burnashev, Monyer et al. 1992),(Geiger, Melcher et al. 1995).

The NMDA receptor is also a heterotetrameric receptor, but highly permeable to calcium ions. It is composed of NR1 and NR2A-D subunits(Mayer 2011). NR2 subunits determine the calcium permeability and kinetics of the receptor. NMDA receptors require the binding of glutamate and glycine (co-agonist) for their activation. At the resting membrane voltage potential the channel pore is block by Mg²⁺ (Nowak, Bregestovski et al. 1984). Gradual membrane depolarization unblocks the channel to its maximum permeability to calcium ions at 0 mV (Grunditz, Holbro et al. 2008). The receptor is also permeable to sodium and potassium. The NMDA receptor acts as a coincidence detector, since there is only influx of calcium when release of glutamate is concomitant with depolarization of the postsynaptic membrane. Influx of calcium through this receptor is thought to be the main trigger for the induction of synaptic plasticity (Kennedy, Beale et al. 2005).

Metabotropic receptors are G-protein coupled receptors. They are subdivided into 3 groups depending of the coupled protein. Group I receptors are coupled to the phospholipase C/inositol-triphosphate signaling cascade and their activation can result in calcium release from internal stores. Group II and III are negatively coupled to adenylate cyclase which forms cAMP from ATP. In CA1 pyramidal neurons group I receptors are located postsynaptically and group II and III are located presynaptically and are involved in presynaptic inhibition (Shigemoto, Kinoshita et al. 1997).

Hundreds of molecules organized into a laminar structure are found in the PSD. Below the receptors is a layer of proteins important for anchoring and proper trafficking of receptors. Primary scaffolding proteins belong to the PSD-95 family which binds to NMDA receptors(Kornau, Schenker et al. 1995) . This family also links receptors to another lamina of signaling proteins important for plasticity. They play a role in the formation, stabilization and morphology of the synapse among them are the protein kinase A,C Ca²⁺/CaM-dependent protein kinase II and others small GTPase activating proteins. (Sheng and Hoogenraad 2007).

b) Cytoskeleton.

In contrast to the dendrite, spines possess a high concentration of actin filaments (F-actin). Actin has been shown to regulate the formation and the morphology of the spine. Altered polymerization/depolymerization states accompany change in head shape. The actin cytoskeleton is regulated by actin binding proteins, which can increase or decrease the rate of polymerization/depolymerisation, but also crosslink actin into higher level of organization. Tens of different actin binding proteins are found inside the spine and are responsible of diverse functions like vesicle or protein transport, regulation of spine morphology, or anchoring of membrane proteins like NMDA receptors (Dillon and Goda 2005). The motor protein Myosin is also found enriched at the PSD. Myosin can regulate the contractibility of actin and affects spine shape (Ryu, Liu et al. 2006).

c) Organelle.

Dendritic spines possess a multitude of intracellular organelles.

Endosome is found inside dendritic spines and is essential to dendritic and synaptic function, sorting membrane proteins for degradation and recycling. Recent studies have shown that postsynaptic endocytosis and exocytosis serve important roles in long-term depression (LTD) and long-term potentiation (LTP) (Man, Lin et al. 2000). Endosomes have been suggested to provide a local store of receptors at individual dendritic spines.

Polyribosomes and proteasomes are commonly found at the base of the spine (Steward and Levy 1982). It has been shown that spine plasticity requires the synthesis and degradation of proteins (Tanaka, Horiike et al. 2008). After induction of LTP, polyribosomes move from the dendrite to the spine (Bourne, Sorra et al. 2007), and could play a central role for the long-term maintenance of synaptic modification.

Smooth endoplasmic reticulum (SER) forms a continuous networks present in soma, axon and dendrite. In CA1 The SER extends into about 50% of spines and forms a laminated of SER called 'spine apparatus' in a small subset of them (20% of all spine)(Spacek and Harris 1997). It has been shown that calcium influx into spines through ionotropic channels can

trigger release from SER, extending the calcium elevation during synaptic transmission (Sabatini, Maravall et al. 2001). The presence or absence of a spine apparatus can influence synaptic plasticity and studies show that mice lacking synaptopodin, a protein essential for the formation of a spine apparatus present deficits in learning (Deller, Korte et al. 2003).

Mitochondria are rarely present inside dendritic spines. They are prominently located inside the dendrite where they produce ATP and also buffer calcium. The ATP produced in the dendrites likely diffuses into spines to provide sufficient energy for signal transduction. However, it has been shown that mitochondria can migrate into some spines during periods of intense activity (Li, Okamoto et al. 2004).

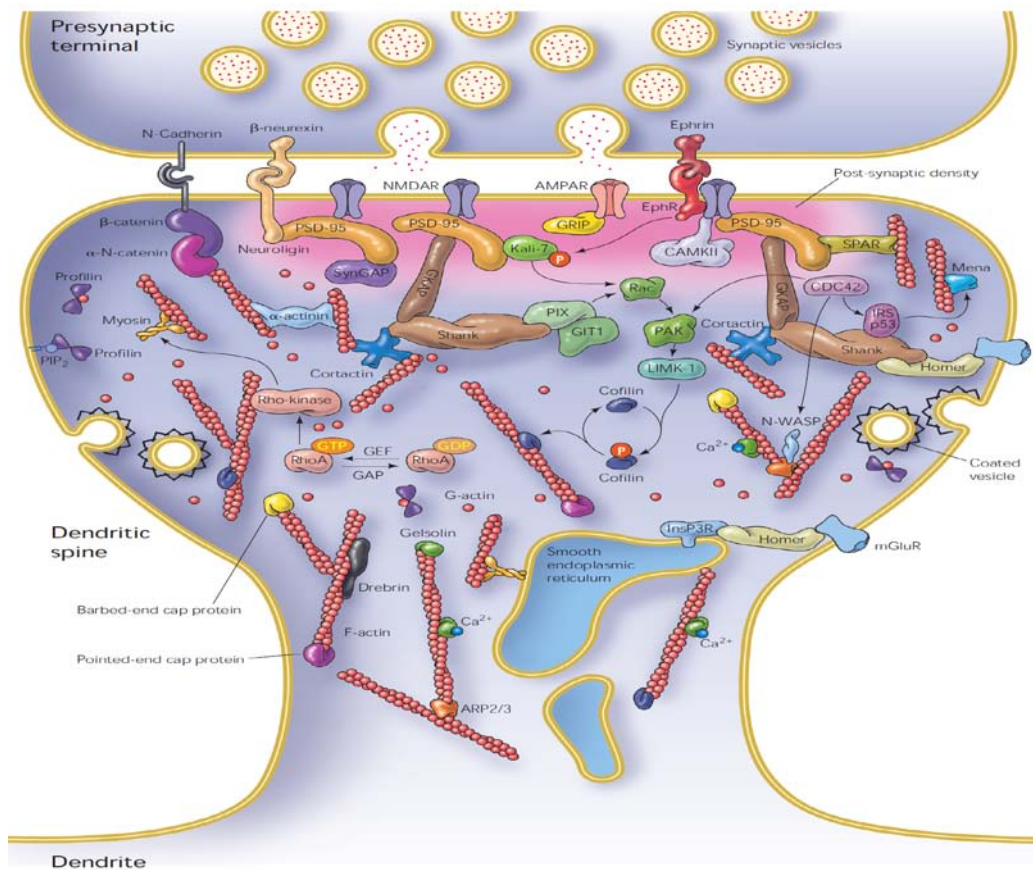


Figure I-5: Some important components of dendritic spines.

Spines are small protrusions at synaptic junctions that use the glutamate, which is released from synaptic vesicles clustered in the presynaptic terminal. Across from these glutamate release sites, AMPA and NMDA subtypes of glutamate receptors are clustered at the postsynaptic active zone within a dense matrix called the postsynaptic density (PSD; pink). Beyond the PSD lie subregions of spine membrane that contain G protein-coupled glutamate receptors (mGluR) and endocytic zones for recycling of membrane proteins. Receptors, in turn, connect to scaffolding molecules, such as PSD-95, which recruit signaling complexes (e.g., regulators of RhoGTPases, or protein kinases). Actin filaments provide the main structural basis for spine shape. Via a network of protein interactions, actin filaments indirectly link up with the neurotransmitter receptors and other transmembrane proteins that regulate spine shape and development, including Eph receptors, cadherins, and neuroligins. Actin-regulatory molecules such as profilin, drebrin, cofilin, and gelsolin control the extent and rate of actin polymerization. These, in turn, are regulated by signaling cascades through engagement of the transmembrane receptors. From (Calabrese, Wilson et al. 2006).

d) Spine geometry and synaptic function.

Dendritic spines present a very large distribution of different sizes and shapes. Since their role is to carry the postsynaptic element an important question is if there is any relationship between spine geometry and synaptic function. Using electron microscopy, different studies have shown that there is a strong correlation between some spine

morphological features and synaptic function. PSD area and spine head volume present a huge variability across spines (more than 20 fold), but interestingly there is a very good correlation between both parameters. These results are very robust among studies, and have been found in different type of neurons: Purkinje cells (Harris and Stevens 1988), CA1 pyramidal neurons(Harris and Stevens 1989), and neocortical pyramidal cells (Arellano, Benavides-Piccione et al. 2007). Immunogold labeling studies have shown that the number of AMPA and NMDA receptors per synapse is proportional to PSD area and spine volume (Nusser, Lujan et al. 1998; Takumi, Ramirez-Leon et al. 1999; Racca, Stephenson et al. 2000). This correlation does not stop at the synaptic cleft, since the PSD area is also correlated to the area of the active zone, the number of docked vesicles, and the number of presynaptic vesicles which is a good correlate of the quantity of neurotransmitter to be released per AP. In summary these studies show that there is correlation between synaptic strength and the size structural feature of synapses, in other words big spines carry strong synapses. This relation has been confirmed by physiological experiments using Glutamate uncaging. This technique allows the stimulation of single synapse located on dendritic spine, bypassing the presynaptic element. Those studies found a good correlation between spine head volume and uncaging evoked EPSP (Matsuzaki, Ellis-Davies et al. 2001), confirming the structural studies realized earlier.

The spine neck connects the synapse to its parent dendrite. Since it is the obligatory passage that molecules or ions have to diffuse through during synaptic activation, it is very important to know if there is also a correlation between spine neck morphology and synaptic strength. In Purkinje cells (Harris and Stevens 1988), CA1 pyramidal neurons(Harris and Stevens 1989), and neocortical pyramidal cells (Arellano, Benavides-Piccione et al. 2007) spine neck length and diameter are not correlated to each others. The morphology of the spine neck is also uncorrelated with spine head volume and the area of the PSD, suggesting that the spine head and neck can be regulated independently. In neocortical pyramidal neurons, on the other hand a weak correlation between spine neck diameter and spine head volume has been described (Arellano, Benavides-Piccione et al. 2007).

2. Compartmentalization

We have seen that a dendritic spine is a very complex structure carrying the synapse and its associated rich molecular machinery, important for its function and regulation. Each spine forms a tiny biochemical reactor in order to regulate each synapse independently. Plasticity is induced by the accumulation of diffusible molecules like calcium which activate the molecular machinery. Synapses are very closely spaced: Spine density (as correlate for synaptic density) has been estimated using serial section electron microscopy to be able to identify all spines regarding of size and position on the dendritic tree. Spine density range from two to four spines per micrometer of dendrite in CA1 pyramidal cells(Harris and Stevens 1989), but this density can go as high as ten spines per micrometer for Purkinje cells (Harris and Stevens 1988). Without strong compartmentalization created by dendritic spine, activated molecules at one synapse could diffuse freely within the dendrite and could reach inactive synapses within few milliseconds. Activity-dependent regulation of individual synapses would not be possible.

There are several factors that influence the compartmentalization of biochemical signals which include diffusion, intracellular binding and removal mechanisms:

- Diffusion is a probabilistic process due to thermal agitation, spreading molecules through random motion. Molecules equally distribute themselves from regions of higher concentration to regions of lower concentration. In case of a dendritic spine, the time of equilibration can be influenced by the anatomical structure and by the coefficient of diffusion of a certain molecule in the cytoplasm. The coefficient of diffusion depends of the size of the molecule and the cytosolic volume accessible to that molecule. Diffusion is inversely proportional to the hydrodynamic radius of a molecule, therefore to the cubic root of the mass. A molecule with a 100 times larger molecular weight would only be slowed down by a factor of 5. Ions which are surrounded by a hydration shell have an increased apparent radius, leading to a slowing down of their diffusion speed (they act like bigger molecules) (Hille 2001). The accessible cytosolic volume can be reduced due to the presence of intracellular organelles or molecular crowding. In the latter case the apparent diffusion coefficient for molecules would be decreased since

molecules would have to find their way between macromolecular complexes.

- Binding of molecules like second messengers or ions to their target can change their apparent diffusion speed. Depending on the affinity and the mobility of targeted molecules, we can see an increase or decrease in the spreading of the messengers.
- Removal mechanism can compete with free diffusion by pumping ions like calcium either out of the cytosol to the extracellular medium or inside organelle like SER.

The morphology of the spine with its huge head connected to the dendrite by a constricted neck suggests that spine would isolate synapse from their parent dendrite. The narrow neck could restrict the diffusion of molecules (e.g second messengers) but could also slow down the diffusion of ions and isolate the spine electrically. Dendritic spines could act as chemical, but also as electrical compartments.

a) Spines act as chemical compartments.

The first studies investigating biochemical compartmentalization of dendritic spines were computer simulations based on 3D reconstruction from serial sections electron microscopy (Westrum and Blackstad 1962; Gamble and Koch 1987)). A first direct measurement of spine compartmentalization became possible thanks to 2-photon microscopy which can resolve individual dendritic spines in highly scattering thick brain tissue. Using fluorescence recovery after photo-bleaching (FRAP), the authors were able to directly measure the diffusional coupling between spine heads and their parent' dendrites in hippocampal slices. They found that small synthetic fluorophores take 20 to 200 ms to cover the small distance between the spine head and the dendrite. This is around 100 times slower than expected (Svoboda, Tank et al. 1996). Longer spine displayed slower recovery in average suggesting a role of spine neck geometry, but long time constants could also be found in spines with short neck. Similar timings were also found in cortical slices but in vivo, diffusion time constant were found to be much broader, with a distribution ranging from 0.27 to 2.42s (Grunditz, Holbro et al. 2008) . Moreover, following spine head compartmentalization over time, a recent study showed that dendritic spine can experience

drastic changes (more than 10 fold) in their diffusional coupling over short period of time (minutes) without a measurable change (at least by light microscopy) in spine morphology. The authors suggested that neck diameter, which is the only parameter not resolvable with two-photon microscopy, must account for that change (Bloodgood and Sabatini 2005). So the diffusional coupling across the spine neck is highly variable, spanning three orders of magnitude, and can be regulated at the level of a single spine but it is not clear what factors influence such heterogeneity. It could be the spine morphology or properties of the cytoplasm that change inside the spine. The situation could be even more complex for interacting molecules that play a role in synaptic function (e.g. calcium, small second messengers, kinases , phosphatases).

Calcium is a very ubiquitous second messenger and the main trigger to induce synaptic plasticity. Upon synaptic activation calcium enters into the spine and activates signaling pathways which locally regulate synaptic transmission. The confinement of calcium transient to individual spine has been shown directly by imaging techniques (Yuste and Denk 1995) using two-photon microscopy (**Figure I-6**). Calcium enters into the spine through three different ways: NMDA receptors, voltage sensitive calcium channels (VSCC), and release from internal stores. Once inside the spine, calcium ions behave differently than small fluorophores. Most of the calcium is taken up by endogenous binding protein and only 5% stays free (Sabatini, Oertner et al. 2002). Since most of the endogenous buffers are immobile, binding slows down calcium diffusion considerably. Calcium signal time course is influence by channel kinetics and by extrusion mechanism across the plasma membrane and through the SER. Since both extrusion and binding are extremely fast processes, spine neck geometry is thought to have little impact on the diffusion of free calcium ions out of the spine. (Sabatini, Oertner et al. 2002). It could control, however, the residence time of Ca-activated second messenger molecules at the active synapse.

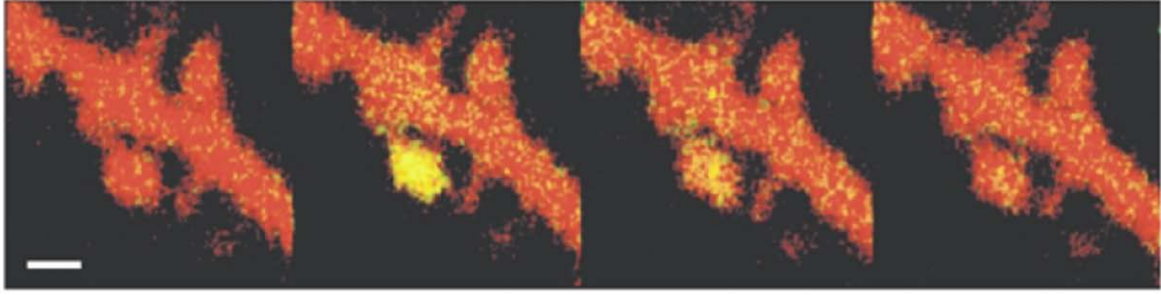


Figure I-6: Calcium transient in a dendritic spine of a CA1 pyramidal cell.

Calcium response to a single presynaptic action potential. Four frames (128 x 128 pixels) were acquired at a rate of 3.9Hz(256 ms per frame). Presynaptic axons were stimulated after the first frame. Images are overlays of the anatomical image (Alexa 594, red) and the calcium-sensitive channel (Fluo5F, green; yellow in overlay). The signal from the green channel is displayed only within the dendrite using a binary mask generated from the anatomical image. Scale bar is 1 μm (Oertner 2002).

The spatial spreading of activated signaling molecules at the single spine level has been studied thanks to recent advances of imaging technology based on fluorescence energy transfer (Yasuda and Murakoshi 2011). This technique can monitor interaction between two molecules tagged with two different fluorophores, or a conformational change of a protein tagged with two fluorophores (Miyawaki 2003). Activity of CaMKII and small GTPase proteins HRas, RhoA, and Cdc42 in single spine activated with glutamate uncaging has been monitored. CaMKII which is one of the most abundant proteins in spine and very important for the induction of synaptic plasticity stays active during around 10s and does not diffuse through the spine neck within this time window (Lee, Escobedo-Lozoya et al. 2009). CaMKII will lead to the activation of small GTPases which activities and spreading are very heterogeneous. Small GTPases can stay active up to 30min and although these proteins have similar structure and diffusion coefficient, they possess a different diffusion profile upon activation. H-ras and RhoA diffuse out of the spine along their parents dendrites over 5-10 μm whereas Cdc42 stays inside the spine (Murakoshi, Wang et al. 2011). A group nicely showed that the diffusion of active h-ras can locally lower the threshold for induction of LTP (Harvey and Svoboda 2007).

We have seen that numbers of important signaling molecules activated during synaptic transmission are highly compartmentalized inside the spine. Compartmentalization of signaling complexes, e.g. CaMKII is probably responsible for the ability of a spine synapse to be independently regulated. The compartmentalization of small diffusible signaling

messengers like cAMP or IP3 is not yet known, but they could be very sensible to the geometry of the spine. The ability of a subset of signaling proteins to escape the spine could be responsible for summation of biochemical signals in the dendrite, favoring clustering of synchronously active inputs.

b) Spines act as electrical compartments.

In neurons, electrical signals are carried by the movement of ions which presumably diffuse freely (in contrast to some of the signaling molecules discussed before). The idea that spines could have an effect on the movement of ions was first proposed in 1952 by Chang (Chang 1952) who suggested that dendritic spines could act as electrical compartments. This first paper was supported by a number of theoretical studies (Koch and Poggio 1983; Wilson 1984; Segev and Rall 1988). The potential effect on electrical signaling depends on spine neck resistivity which could attenuate the EPSP. This attenuation would decrease the impact of the synapse, and a larger number of synapses would have to be activated at the same time to trigger an action potential. However, studies estimating the biophysical properties of spines in their basal state based on electron microscopic reconstructions of spine geometries and diffusional coupling through spine necks concluded that most spine necks are not thin and long enough (spine neck resistances are too small) to significantly modulate synaptic currents (Harris and Stevens 1989; Svoboda, Tank et al. 1996).

But even if the spine neck resistivity is not sufficiently large to affect the size of synaptic currents at the soma, it could still enable strong local depolarization of the spine head itself.

Since spines contain VSCCs, a voltage difference between spine head and dendrite may selectively activate VSCCs and NMDA receptors in the head, further boosting local depolarization in the spine head. An increasing number of studies using sophisticated imaging techniques, calcium and voltage imaging to monitor synaptic function concluded that spines can have an effect on electrical signaling (Araya, Jiang et al. 2006; Grunditz, Holbro et al. 2008; Bloodgood, Giessel et al. 2009; Palmer and Stuart 2009). The level of spine neck resistance could then influence calcium kinetics and amplitude by controlling the voltage in the spine and permit regulation of synaptic signaling cascades.

In conclusion, we have seen that dendritic spines compartmentalize otherwise freely diffusible molecules. It has to be taken into account that the diffusion of many signaling molecules is strongly influenced by the mobility of their binding partners. In addition electrical compartmentalization produced by spine morphology could increase local membrane depolarization, boost the entrance of calcium into the spine head, and thus influence plasticity.

II. Aim of the Thesis

Dendritic spine compartmentalization is thought to be important for synaptic function, since strong compartmentalization could increase the concentration of activated molecules close to the synapse during repetitive synaptic stimulations, and also increase depolarization in the spine head. But it is not fully understood how and to what extent spines compartmentalize biochemical signaling. Compartmentalization and morphology of dendritic spines have been demonstrated to be extremely variable.

The aim of our study was to investigate whether information about spine ultrastructure is sufficient to predict diffusional coupling with the dendrite.

To answer that question we developed a correlative approach to gain information about diffusional coupling and morphology of individual spine. We found that compartmentalization of small molecules can be predicted from spine morphology and also that their diffusion speed is slowed down inside spines compare to dendrites. This discovery could explain a controversy between studies investigating the role of dendritic spines as an electrical compartments.

Since the diffusional coupling of alexa can be predicted by spine morphology. We used Alexa dye as a correlate for spine morphology to investigate the compartmentalization of larger molecules. We observed that larger molecules are regulated independently of spine morphology.

Theoretically, dye particles and other molecules should concentrate in high viscosity compartments. We tested this prediction by creating synthetic images based on 3D reconstructions from our EM data. We found that spines under two photon images appear too bright, thus dendritic spines act as enrichment devices.

By integrating informations from diffusion and ultrastructure measurements on the same dendritic spines we have gained new insights on the regulation of compartmentalization in dendritic spines. These insights could help to resolve contradiction in previous studies and also supplement the model of dendritic spine functionality.

III. Methods

A. Slice culture

Dendritic spine compartmentalization was investigated in hippocampal organotypic slices prepared from Wistar rats. This method developed in the nineties (Stoppini, Buchs et al. 1991) is the method of choice to maintain explants of central nervous tissue for long term with a high degree of cellular differentiation and organization (Gahwiler, Thompson et al. 2001) . The major characteristic of this technique is the use of semiporous membranes to culture the explants which are maintained at the interface between a culture medium and a CO₂ enriched environment. Compared to other technique like roller tube culture where the explants flatten into a monolayer, interface cultures stay thicker and retain their three dimensional structure. Since cultures are prepared from 5 days old postnatal rats where the cellular and tissue organization is already well advanced, the original local circuitry remains intact (**Figure III-1**). Although cultures develop in isolation from the outside world, explants continue to develop at a similar rate compared to in vivo. Development of synaptic transmission and dendritic morphology are similar that acute slice prepare from the same age as the culture but connectivity is higher (De Simoni, Griesinger et al. 2003).

Tissue slices were prepared from 5 day old Wistar rats under sterile conditions. The brain was removed, hippocampus was dissected and placed onto tissue chopper (Mcllwain). Slices of 400 µm were cut and collected in Petri dish containing chilled MEM. The single slices were then transferred to humidified membrane insert (Millicel-CM, Millipore 0.4 mm pore size), which was placed in culture plates with 750 µl MEM. The medium was replaced every 2-3 days. The dissection medium contained 1 mM CaCl₂, 5 mM MgCl₂, 10 mM glucose, 4 mM KCl, 26 mM NaHCO₃, 2 mM kynurenic acid and 1mL phenol red. The medium was vacuum filtered and stored at 4 °C. MEM contained 20% Horse Serum, 1 mM L-glutamine, 0.00125% ascorbic acid, 1 µg/ml insulin, 1 mM CaCl₂, 2 mM MgSO₄, 13 mM D-glucose and 1µg/ml retinol. The medium was vacuum filtered and stored at 4 °C.

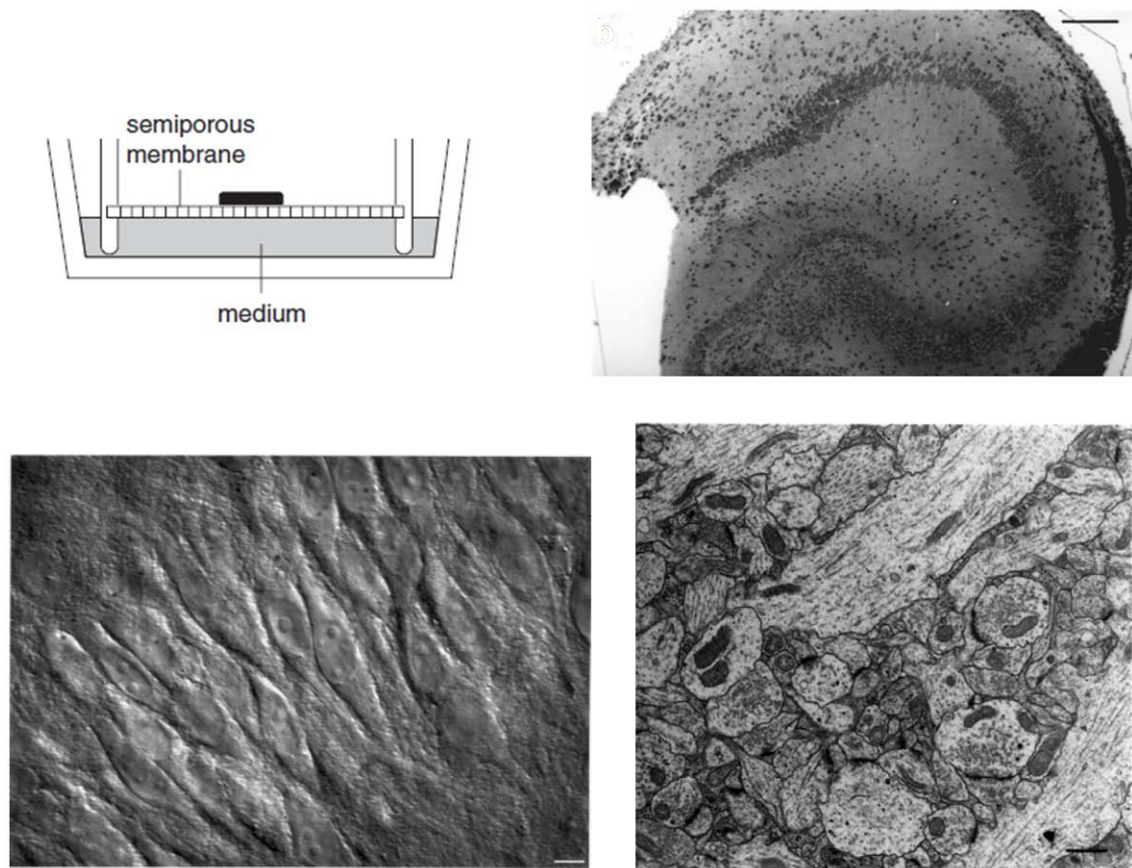


Figure III-1: Hippocampal slice cultures.

(a). The slice is placed directly on a semiporous membrane, and medium is added to the bottom of the culture dish. In these stationary cultures, the slices are immersed in the medium on one side and accessible to oxygen from the other side. (b). Semithin section stained with methylene blue/Azur II and cut in a plane parallel to the membrane. Note the well preserved anatomical organization of the hippocampal slice culture. (c) Living pyramidal cells in hippocampal slice culture. Differential interference contrast (bar = 15 μm). (d) Electron microscopic images of *stratum radiatum* in the CA1 area of a 4 week old hippocampal slice culture. Modified from (Gahwiler, Thompson et al. 2001).

B. Plasmid construct and transfection

5-6 days old hippocampal organotypic slice cultures were biolistically transfected with expression cassettes of appropriate proteins using a Helios Gene Gun (BioRad).

Expression cassettes were generated by cloning cDNAs of appropriate proteins into a neuron specific expression vector. The human synapsin 1 gene promoter was used to enable neuron-restricted transgene expression (Kugler, Meyn et al. 2001). The tandem dimer of a monomeric red fluorescent protein (tidimer2RFP) from Roger Tsien was used as a volume marker (Campbell, Tour et al. 2002). A photoactivable green fluorescence protein (PA-GFP) was used to measure the diffusion coupling between a spine and its parents

dendrite. PA-GFP was made from EGFP by substituting threonine 203 to histidine (T203H) (Patterson and Lippincott-Schwartz 2002). It contains also an A206K mutation to disrupt dimerization.

Plasmids are then introduced into the cell where the expression cassette is integrated into the genome of the host neuron and corresponding proteins can be expressed. Biolistic transfection, was first developed as a method of gene transfer into plant cells (Klein, Wolf et al. 1992) through the cell wall. It later became a very popular transfection method in neuroscience as it is well suitable for neuronal organotypic slice cultures (McAllister 2004; O'Brien and Lummis 2006). Biolistic transfection is efficient, reliable, and optimal to have a sparse transfection to be able to assess fine morphology of single neuron in intact brain slice. The DNA is attached to a tiny biologically inert particle (usually gold). By accelerating such DNA-particle complex and placing the target tissue within the acceleration path, DNA is effectively introduced into the cell. For introducing the plasmids into the cells we used Helios Gene Gun (BioRad). This hand-held device accelerates DNA-coated gold particles that are precipitated on the inner wall of a plastic tube (cartridge) by pressurized helium. The bullets are made this way. 8 µg Plasmid-DNA and 27 µl nupherin (3 mg / ml) were diluted to a total volume of 100 µl. After incubating at RT for 15 min the DNA was stacked to nupherin. 4 mg gold was suspended in 20 µl spermidine (250 mM) by vortexing and sonicating. Afterwards, the DNA-nupherin mix was added to the gold. To precipitate the DNA 120 µl CaCl₂ (1 M) was added slowly to the DNA-gold solution. After incubating at RT for 10 min the gold was spin down. The supernatant was removed and discarded. The DNA-gold particles were washed three times with ethanol and dissolved in 3 µl PVP ethanol (0.04 mg / ml) solution. A tube (25 cm) was loaded with this solution and dried in the Tubing Prep Station. Afterwards, it was cut into ≈ 50 cartridges with the Tubing Cutter. The cartridges were stored with a desiccant pellet at 4 °C. We used 13.79 bar helium pulse to sweep the DNA- coated gold microcarriers from the inner wall of the cartridge directly into the hippocampal organotypic slice cultures. Protein expression increase slowly, and after 1-2 weeks we used the transfected cells for experiments.

C. Two-photon imaging

Neurons are organized into a complex network. To fully understand their physiology it is preferable to study them in their intact environment. Using microscopy to image into such a thick tissue is challenging because brain tissue is highly scattering.

Traditional microscopic techniques use a linear absorption process where a molecule is excited by the absorption of one photon. The molecule emits a photon of longer wavelength and return to its ground state (**Figure III-2.a**). The absorption occurs within the entire excitation light cone (**Figure III-2.b**). In confocal microscopy a pinhole rejects fluorescence from off-focus locations, but above and below the focal plane the entire specimen is illuminated and damaged. Moreover, the pinhole rejects photon coming from the focus that are scattered on their way back resulting in loss of information. Increasing the excitation to compensate for signal loss leads to even more damage and phototoxicity. This technique is only optimal for thin tissue.

Two photon microscopy was invented about 20 years ago and uses a non-linear absorption process (Denk, Strickler et al. 1990). Two photons of low energy are absorbed simultaneously (within 0.5 fs) by a molecule. Their energy is summed up to bring it to an excited state. A photon of shorter wavelength is emitted when the molecule returns to its ground state. The rate of such absorption depends on the second power of the light intensity. In a focused laser beam, the intensity is highest in the focus and drops off quadratically with distance, resulting in a drop of excitation with the 4th power of distance. As a result, fluorophores are excited almost exclusively in a tiny diffraction limited focal volume that can be as small as $0.1 \mu\text{m}^3$ (Zipfel, Williams et al. 2003) . All emitted photons can be collected, since they all originate from that volume. In contrast to confocal microscopy there is no need to use pinholes to reject out-of-focus fluorescence. The undesirable effects of bleaching and photo toxicity are also restricted to the focal volume. In addition, the wavelength used for two photon excitation is longer than in case of one-photon fluorescence. Photons of longer wavelength interact less with matter and are less absorbed by endogenous chromophores, in consequence they get less scattered and can go deeper into the tissue. Moreover, since the scattered excitation photons are too dilute for 2-photon excitation and too low energy to create 1-photon excitation, they cannot cause appreciable fluorescence. Because of these advantages, 2PE laser scanning microscopy is a powerful new technology that is contributing to discoveries in neurobiology on many

spatiotemporal scales. Since this method enables calcium measurements in highly scattering brain tissue, it is especially useful for anatomic and functional imaging of such tiny structures as single synapses (Svoboda and Yasuda 2006).

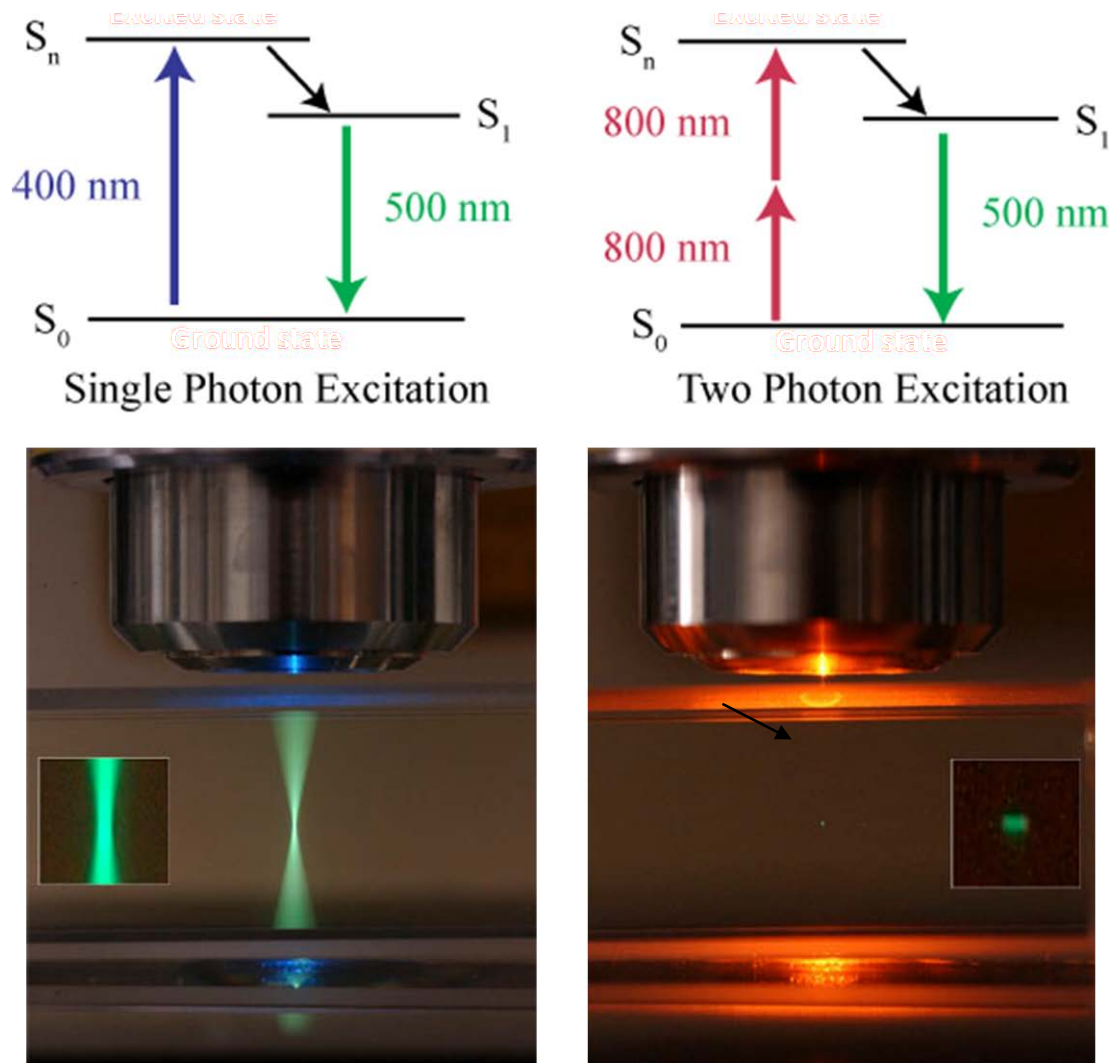


Figure III-2: One versus two photons fluorescence.

(a) Simplified Jablonski diagram for one and two photon transition, based on wavelength of the incoming photon(s). Values chosen for simplicity, a range of wavelengths can generate TPE, dependent on the specific dye's absorption cross section. (b) The blue laser excites an entire column of sample whereas the IR pulse laser excites only a small spot of sample. (from <http://mcb.berkeley.edu/labs2/robey/content/2-photon-imaging>)

1. Experimental setup

Live imaging experiments were done on a custom-built dual beam two-photon laser scanning microscope. It is based on a BX51WI microscope (Olympus) equipped with a LUMPF/IR 60X 0.9 NA, Olympus objective controlled by an open source software Scanimage (Pologruto, Sabatini et al. 2003). Two ultrafast IR lasers (Chameleon-Ultra, Coherent) controlled by Pockel's cells (350-80, Conoptics) were combined by polarizing optics (Thorlabs). One laser was tuned to 960 nm for two-photons imaging PA-GFP and RFP or 810 nm for Alexa Fluor 594. The second laser was tuned to 750 nm for two-photon photoactivation (2PLPA) of PA-GFP (Schneider, Barozzi et al. 2005). Fluorescence was detected in epi and transfluorescence (achromatic aplanatic condenser, 1.4 NA, Olympus) modes using 4 photomultiplier tubes (R3896, Hamamatsu). We used 725DCXR dichroic mirrors and E700SP blocking filters to reflect emitted photons into a secondary beam splitter, containing a 560DCXR dichroic, 525/50 (525 ± 25 nm, green) and 610/75 (610 ± 37.5 nm, red) band pass filters (AHF Analysentechnik) (**Figure III-3**).

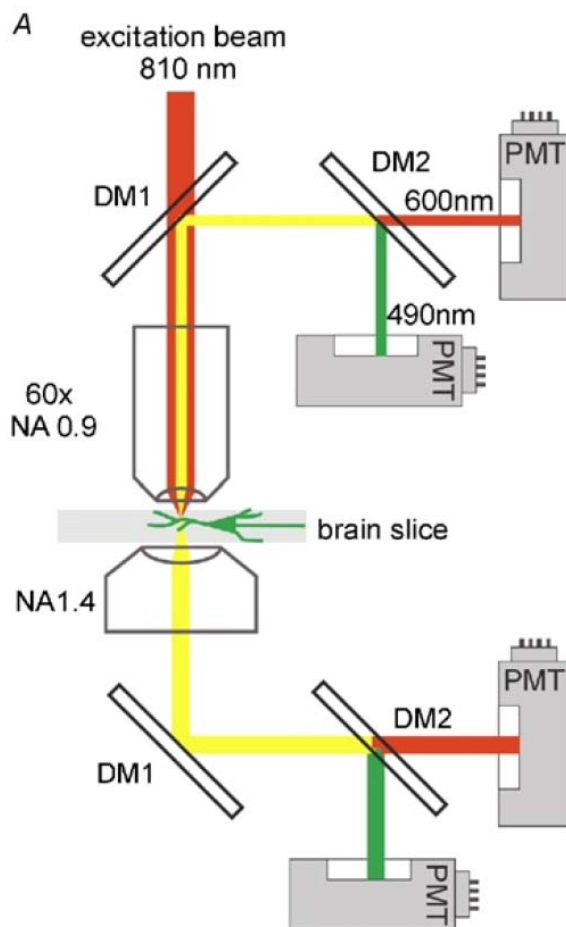


Figure III-3: Scheme of fluorescence detection system used in two-photon setup.

An infrared laser beam (810 nm) is used to excite fluorescence in the preparation (scan mirrors not shown). Emitted photons are collected through the objective and through the condenser. Primary dichroic mirrors (DM1) separate the emitted photons from the excitation beam, secondary dichroic mirrors (DM2) are used to direct photons from the green and the red fluorescent dye to different photomultipliers (PMTs). Lenses and filters are omitted for clarity (Oertner 2002).

2. Electrophysiology

Slice cultures were superfused with artificial cerebrospinal fluid (ACSF) at room temperature containing (in mM) 127 NaCl, 25 NaHCO₃, 25 D-glucose, 2.5 KCl, 1 MgCl₂, 2 CaCl₂, 1.25 NaH₂PO₄, 0.05 chloroadenosine. Cells were filled with a synthetic dye during whole-cell voltage clamp recordings using an Axopatch 200B amplifier (Axon Instruments). Pipettes were pulled from borosilicate glass capillary tubing to yield tips of 4-6 MΩ resistance and were filled with (in mM): 135 Kgluconate, 10 HEPES, 10 sodium phosphocreatine, 3 sodium ascorbate, 4 MgCl₂, 4 Na₂-ATP, 0.4 Na-GTP and 0.030 Alexa Fluor 594 or/and, 1mg/ml of neurobiotin. pH and osmolarity were adjusted to 7.3 and 290mOsm respectively. In some experiments 1mM NBD-M-TMA a cationic dye was included in the intracellular solutions (Aavula, Ali et al. 2006).

3. Image acquisition and analysis

a) Measurement of coupling between dendritic spine and its parent's dendrite.

To measure coupling between dendritic spine head and its parent's dendrite we used a technique called fluorescence recovery after photobleaching (FRAP) or photo-activation. A neuron was filled with the synthetic fluorophore Alexa-fluor 594 through a patch pipette. After 10 min the neuron was filled with the dye and it was possible to image individual dendrites with spines using 2-dimensional scan mode (Frame scan) (**Figure III-4**). Typical format of a xy-frame was 128*128 pixel scanning at 2 ms / line. Spines with a head clearly separated from the dendrite were selected for diffusion measurements to avoid bleaching part of the dendrite. To monitor fluorescence in the spine head with a fast time resolution, we use line scans at 500Hz. Baseline fluorescence was measured for 128 ms. The power was then briefly increased (0.5ms) to bleach 30% of the baseline and set to its initial value to monitor the recovery (**Figure III-4.b**). The fluorescence was monitored at power levels that did not produce noticeable bleaching (**Figure III-4.c**). Analysis software custom written in Matlab was used to optimize the different parameters for every experiment and for online analysis. The time course of recovery was well fitted by a single exponential recovery (**Figure**

III-4.d). Since bleaching is an irreversible process, fluorescence recovery represents the exchange of bleached alexa molecules by unbleached molecules from the dendrite by diffusion and $\tau_{\text{equilibrium}}$ (τ_{equ}) reflects the time constant of diffusional equilibration through the neck. To ensure adequate signal-to-noise ratio in the exponential fit, only fluorescence decrease whose amplitude was above two times the standard deviation of fluorescence in the baseline period were included in the analysis. The same selection process was used for PA-GFP or RFP expressing cells. In case of photoactivation of PA-GFP, the brief increase in fluorescence was followed by a decay which again represents the exchange of activated PA-GFP from the spine head with non-fluorescent PA-GFP molecules from the dendrite.

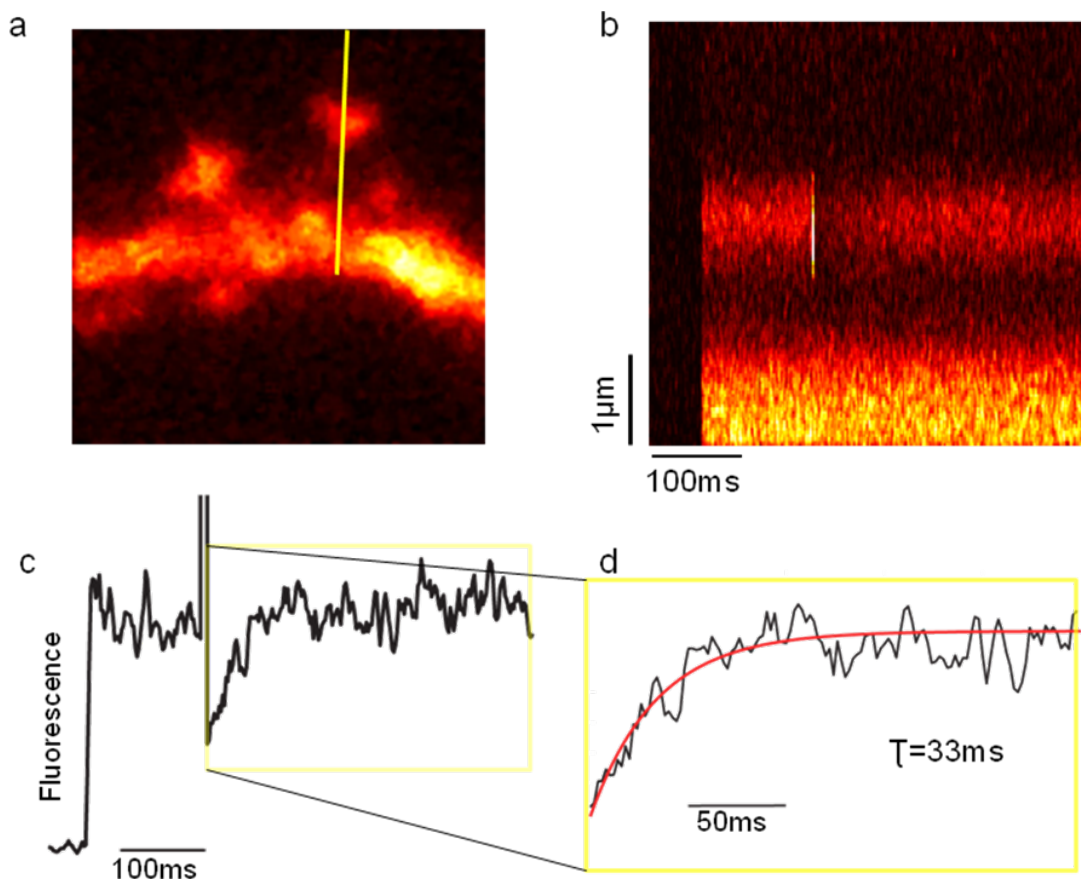


Figure III-4: Measuring diffusional coupling by bleaching spine head fluorescence.

(a) Frame scan mode was used to select a dendritic spine separated from the dendrite for a FRAP experiment. The yellow line represents the lines-can used in figure b. (b) Line-scan profile. Ordinate represent the distance along the line scanned, and abscise represent the time. We can see the short laser pulse bleaching the fluorescence in the spine head. (c) Fluorescence average integrated in the spine head over time. Note fluorescence recovery to the baseline. (d) A single exponential was fitted to the recovery.

b) Measurement of coefficient of diffusion in dendrites.

To estimate the diffusion coefficient of fluorophore within CA1 hippocampal pyramidal dendrites, we performed FRAP experiments in the dendrite. The decrease in fluorescence induced by a FRAP pulse was measured as a function of space along the dendrite and fitted with Gaussian functions. The standard deviation of the Gaussian (spread of bleached fluorophore along the dendrite, $\sigma(t)$), is related to the diffusion coefficient D of the fluorescent molecule by $D=(1/2).d[\sigma^2(t)]/dt$. Thus, D is given by the slope of plot $\sigma^2/2$ versus time (Soler-Llavina and Sabatini 2006). The fluorescence of Alexa was measured in line-scan mode along the dendrite for high temporal resolution (500Hz). A Gaussian fit was calculated for every trace.

c) Estimation of spine volume.

Assuming homogenous distribution of Alexa-Fluor 594 in the cytoplasm, the integrated fluorescence intensity (red channel) of a spine is proportional to its cytoplasmic volume (Svoboda, 2004) ((Holtmaat, Trachtenberg et al. 2005)). For each cell, a calibration measurement was taken by scanning the laser across the proximal apical dendrite, a cellular compartment large enough to contain the entire point-spread function (PSF) of our microscope, to get the maximum fluorescence intensity (f_{max}). This calibration measurement was typically taken at a different depth (z_{cal}) than the spine image (z_{spine}), and attenuation of the laser was corrected using an experimentally determined attenuation function

To measure the absolute volume of a spine (V_{spine}), we first calculated the Gaussian intensity distribution a hypothetical PSF-sized object would produce if imaged at the same zoom factor and the same depth than the spine (f_{sim}). The integrated intensity of f_{sim} (sum of all pixel values within a region of interest, $\iint f_{sim}$) was then compared to the integrated intensity of the spine image in the center plane ($\iint f_{spine}$). The volume of the spine is related to the spine intensity as follows:

$$V_{spine} = \iint f_{spine} * V_{PSF} / \iint f_{sim}$$

The volume of the PFS ($V_{PSF} = 0.38 \mu m^3$) was determined using fluorescent beads (0.1 μm , Molecular Probes).

D. Serial block face scanning electron microscope.

To reconstruct the detailed 3D structure of dendritic spine, we used a newly developed electron microscope technique called serial block face scanning. This microscope is a scanning electron microscope combined with an ultramicrotome directly placed inside the chamber of the microscope. The tissue embedded in resin is placed inside the chamber. The SEM will take an image of the surface of the block using back scattered electrons to form an image. A diamond knife will then cut an ultrathin section off the top of the block. The block is moved upwards to stay in focus, and another image is taken. This cycle can be automatically repeated as many times as needed to take a full 3D stack of a desired volume. The different pictures forming the stack are perfectly aligned (**Figure III-5**) (Denk and Horstmann 2004).

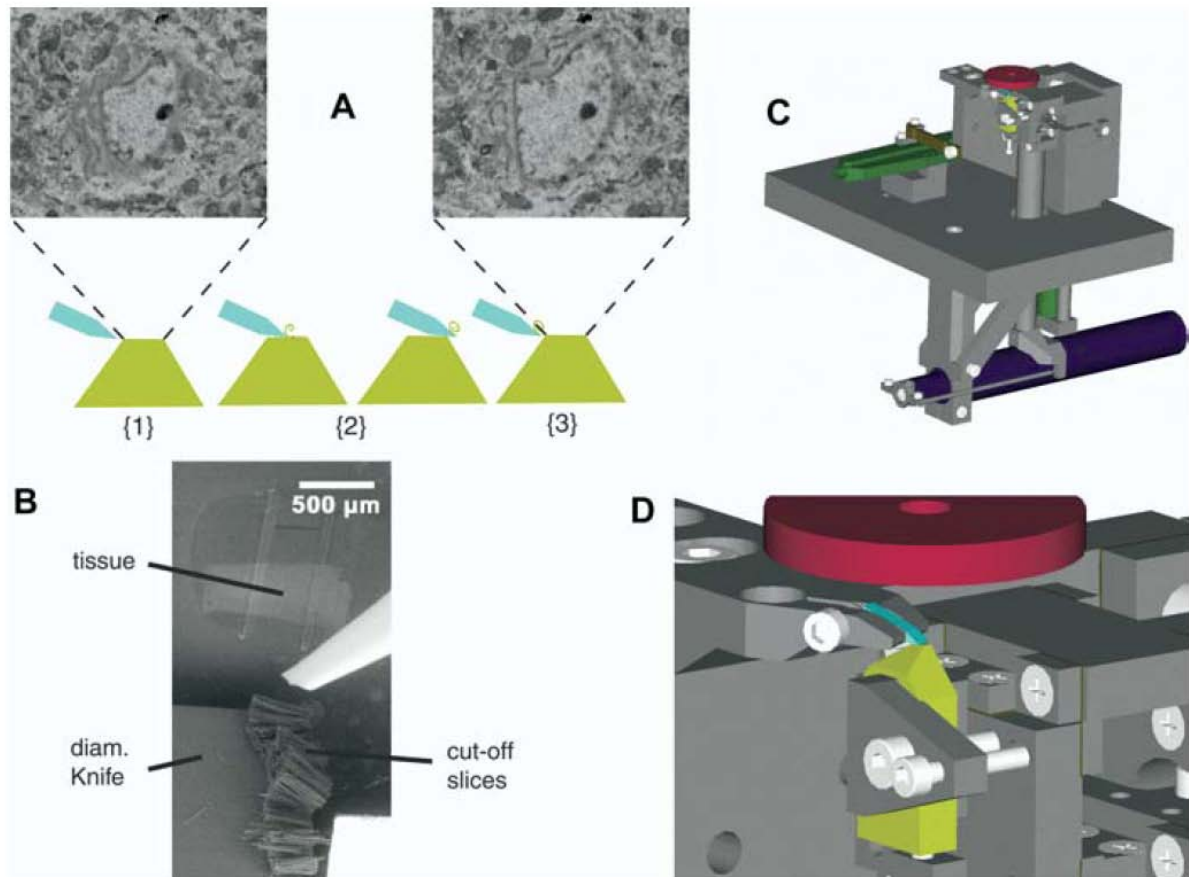


Figure III-5: Serial block face SEM

(a) Principle of SBFSEM operation: 1) a SEM image is taken of the surface of the plastic embedded tissue preparation (2) then with a diamond knife (blue) an ultrathin slice is cut off the top of the block (3) After retraction of the knife the next picture is taken. (b) usually cut-off slices pile up on the top of the knife, protruding into the picture from the right is a puffer pipette occasionally used to remove debris from the knife. (c and d) The mechanical design for the in-chamber microtome is shown in an overview (c) and a close-up of knife and sample (d) in renderings. Most parts are nonmagnetic stainless steel (grey). A large motion leveraged piezo actuator (green part on the left) drives the knife holder back and forth. The custom diamond knife (light blue) is clamped in a special holder. The sample (amber) advance is driven via a lever by a direct current motor driven micrometer (dark blue). From (Denk and Horstmann 2004)

E. Correlative microscopy

To gain a better understanding of the mechanisms regulating the compartmentalization inside dendritic spines, we needed to combine the diffusion measurements recorded with two-photon microscopy with the detailed morphology of the previously imaged spine, reconstructed from electron microscopy. It can be challenging to recover a single spine with a volume of less than $0.1 \mu\text{m}^3$ in a tissue of more than $1\,000\,000$

μm^3 . One needs to mark specifically the spine of interest and know exactly where that mark is located in the tissue. We developed the following procedure:

1. Recovery of the previously imaged neuron by DAB staining

To measure the diffusional coupling between the spine head and its parent dendrite we filled the cell with a fluorescent dye. At the same time, the cell was filled with neurobiotin at a concentration of 1mg/ml. Neurobiotin diffused freely inside the neuron during the experiment. At the end of the experiment (after around 30 min), the pipette was retracted while monitoring patch parameters. The goal was to avoid ripping a hole in the membrane while retracting the pipette. Otherwise, the large calcium influx could induce changes in the morphology of the dendrite and spines that were previously imaged.

The tissue was incubated over night in an ice cold solution of 1% paraformaldehyde, 1% glutaraldehyde and 1 μM of tetrodotoxine (to block spiking during the fixation process) in 0.1M phosphate buffer.

The following day, the tissue was processed for the recovery of the previously imaged neuron using a Diaminobenzidine (DAB) staining against neurobiotin. The protocol can be briefly described as follow:

- slices were washed 6-8 times in phosphate buffer at 0.1M(pH=7.4)
- To increase the penetration of the DAB in the tissue, the tissue was immersed into liquid nitrogen to produce micro-fractures. Before the tissue was successively incubated in 10% and 30% sucrose solution for cryoprotection.
- Endogenous peroxidase activity was blocked by washing the tissue in 3% H_2O_2 . The tissue was then washed to remove all traces of H_2O_2 , as H_2O_2 would interfere with the DAB staining.
- We then proceeded with the DAB staining. DAB gives a black precipitate in presence of Horse radish peroxidase. This enzyme is coupled with avidin which has a very strong affinity for biotin. In consequence the complex avidin/enzyme will only be localized in the dendrite filled with biotin and a black precipitate will form after addition of DAB. This black precipitates is opaque to photon and reflects incoming electrons, resulting in high contrast and a white appearance in SBFSEM. The complex avidin/enzyme was

incubated over night at 4 C. After washing the complex from the tissue, DAB was added and incubated for 20 min. H₂O₂ was then added to induce the formation of the black precipitate. The reaction was monitored under the microscope and stopped by transferring the slices to 0.1M PB.

2. Embedding

The sample needs then to be stained and transferred into a solid state to preserve the structure and allow the tissue to be cut in very thin section for electron microscopy. Here is a brief procedure for the embedding:

- Tissue is washed in cacodylate buffer.
- Post-fixation in osmium at 1% for 40 min will fix and stain membranes
- Section are washed in distilled water
- Second staining in 1% uranyl acetate
- The tissue is then dehydrated in graded alcohol series
- Infusion with a “plastic” formulation followed by polymerization in the oven at 60 °C for 48 hours

3. Recovery of previously image spine in the SBFSEM.

After staining with heavy metal and embedding into the resin it was still possible to visualize the neuron of interest using a conventional light microscope. An area of about 1mm² was marked around the neuron and trimmed with a thin razor blade. The resulting small cube was glued on a translucent stub. This stub was used to hold the sample in the ultramicrotome for trimming and also in the SBFSEM for imaging. The sample was trimmed precisely using an ultramicrotome until the dendrite of interest was isolated into a small volume. The final volume was a trapezoid shape with a size of 200 to 300 μm. This was done by cutting edges of the block until the area of interest (the previously imaged piece of dendrite) remained in the center of the block. Going back and forth several times between the ultramicrotome and the light microscope was necessary. The top of the block was also trimmed to bring the dendrite of interest as close as possible to the surface. When the trimming was finished, the precise location of the dendrite in the block was documented by taking images with the light microscope. The coordinates of the dendrite of interest relative

to the sides of the block were used in the SBFSEM to find the exact position of the dendrite
(Figure III-6.)

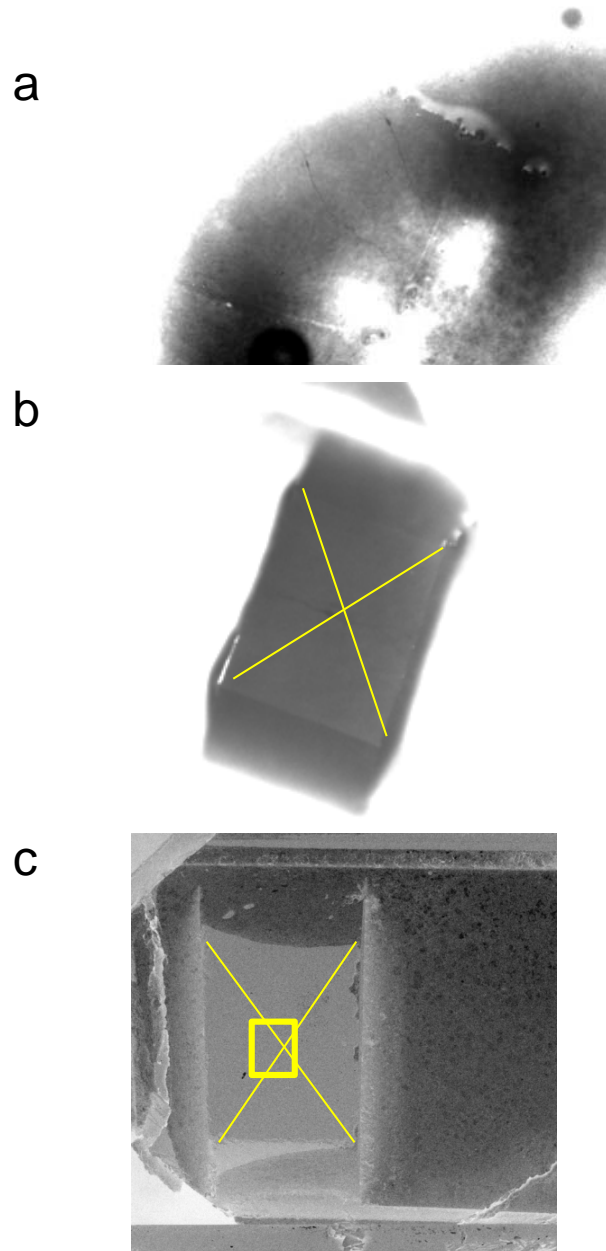


Figure III-6: Correlative between light and electron microscopy.

(a) Neuron of interest was visible under light microscopy. (b) After trimming, the precise location of the dendrite of interest was documented. (light microscopy) (c) Position of the dendrite of interest was recovered in the SBFSEM. (Electron microscopy)

4. Imaging and image analysis.

Once the location of the dendrite of interest was localized, an area of few tens of μm^2 was selected. This area was imaged between two consecutive cuts. If the neuropil was not visible on the surface of the block, low resolution pictures and/or consecutive slices without imaging were used to speed up the process of finding the region of interest. Once the tissue of interest was visible, the following parameters were used for automatic sectioning:

- resolution: 0.011 μm per pixel in x y and 50 nm in z
- image size: 8192 * 8192 pixel
- magnification: 1600
- time per pixel: 7 μs , thus 1 image took 8 minutes

Once the dendrite of interest was imaged, the resulting stack could be analyzed. One stack can easily exceed 50 GByte, so preprocessing of the data set was an essential first step. After down sampling by a factor of 4, we could open the entire stack in Imaris using a fast PC with 64 GByte of RAM. Since the contrast between the stained dendrite and the surrounding tissue is very high, automatic segmentation and 3D rendering in Imaris was trivial. Structural features like branching points or characteristic spines helped us to find the previously imaged region of dendrite. This location was recorded and used to crop the full resolution data set. The final data set containing only the dendrite of interest at full resolution was typically 10-20 GByte.

The DAB staining was not perfectly uniform inside the dendrite. Intracellular organelles such as mitochondria were not stained. In addition, there were also spherical zones ('blobs') where the DAB reaction apparently had not proceeded. Therefore, we used two different segmentation methods: Automatic thresholding to generate the coarse dendritic morphology, and manual contour tracing for spines where the precise shape and volume was of interest. The spine head volume and morphological features of the spine neck (diameter and length) were extracted from the 3D reconstruction using inbuilt measurement tools in Imaris. For large-scale reconstruction of the dendrite, we used an automatic thresholding method. The intensity of the threshold was set on one slice to fit the

stained area. This threshold was then applied to every slice for automatic 3D reconstruction (Figure III-7)

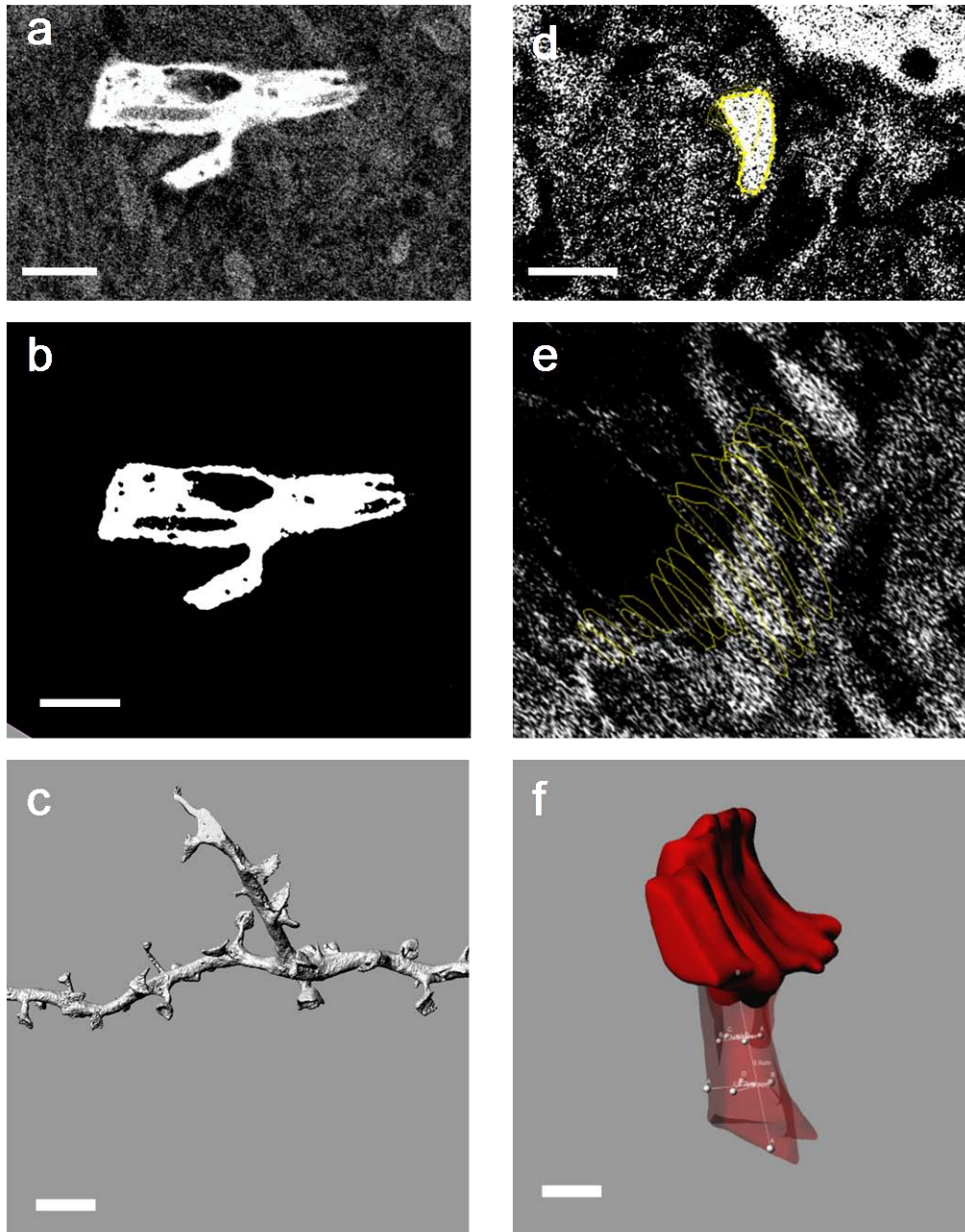


Figure III-7: 3D EM reconstruction.

(a)(b)(c) Automatic reconstruction. (a) Piece of dendrite with a spine visible. Raw EM image. Scale bar, 1 μm (b) Automatic segmentation of the stained area by setting the intensity of the threshold. Scale bar, 1 μm (c) The entire dendrite was automatically reconstructed by applying the segmentation on every slices. Scale bar, 4 μm .

(d)(e)(f) Manual reconstruction. (d)(e) Manual contour tracing. Scale bar, 1 μm . (f) 3D reconstruction of the entire dendritic spine. Volume of the spine head and spine neck morphology were measured. Scale bar, 0.3 μm .

The preparation of the tissue included fixation and dehydration procedures which could shrink the tissue. To correct for any modification in the size of the tissue we applied a shrinkage correction using our correlative data set. Once the two photon microscope and the SBFSEM were calibrated, we measured the same distance between different spines in the maximum intensity projection from a two-photon image stack and in the 3D EM reconstruction. Since maximum intensity projections were 2D whereas the EM reconstruction was 3D, we used Pythagoras' theorem to calculate the correct distance.

F. Estimation of spine neck resistance.

We estimated the resistance of the spine neck according to the cable equation.

$$R_{\text{neck}} = \rho_i \text{ spine } L/A$$

ρ_i is the cytoplasmic resistivity in $\Omega \cdot \text{cm}$, L is the spine neck length, A is the cross sectional area of the spine neck. Estimates of ρ_i range from 200 to 400 in $\Omega \cdot \text{cm}$ (Fromherz and Muller 1994). We used $\rho_i = 250$ in $\Omega \cdot \text{cm}$; with $\rho_i = 200$ in $\Omega \cdot \text{cm}$, R is decreased by a factor of 1.25, and with $\rho_i = 400$ in $\Omega \cdot \text{cm}$ R_n is increased by a factor of 1.6. We calculated ρ_i in the spine assuming a linear relationship between the decrease in D_{alexa} and the increase in ρ_i (Svoboda, Tank et al. 1996)(Berg 1993). $\rho_{i \text{ spine}} = \rho_{i \text{ dendrite}} * (D_{\text{alexa}}(\text{dendrite}) / (D_{\text{alexa}}(\text{spine})))$.

G. Computation of Digitally Reconstructed Fluorescence Images (DRFI)

The computation of Digitally Reconstructed Fluorescence Images (DRFI) enabled us to compare the fluorescence intensity distribution from live tissue to a prediction based on EM morphology. DRFI use the geometrical correct shape of neural structures combined with a synthetic Points Spread Function (PSF) and represent then assuming a homogenous distribution of fluorophores within the neural structures. The computation of DRFIs itself is a convolution of the PSF (as kernel) and the geometrical correct representation of the object as image. This part of the project was done in close collaboration with Clemens Blumer, PhD student in the computer science department of the University of Basel (with Prof. T. Vetter).

1. Reconstruction of geometrical structures

We used images from SBFS-EM in which the volume of one CA1 pyramidal cell was labeled. In these images, geometrical correct dendritic morphology could be automatically reconstructed. We corrected the reconstruction manually for artifacts (at object surface and enclosed artifacts). Enclosed artifacts (blobs) are regions where the labeling did not work successfully. Furthermore, we ensured that in the reconstruction the volume of enclosed mitochondria was excluded from the reconstructed volume, since mitochondria were also not filled with fluorescent dye. **Figure III-8** shows a flowchart of the reconstruction process.

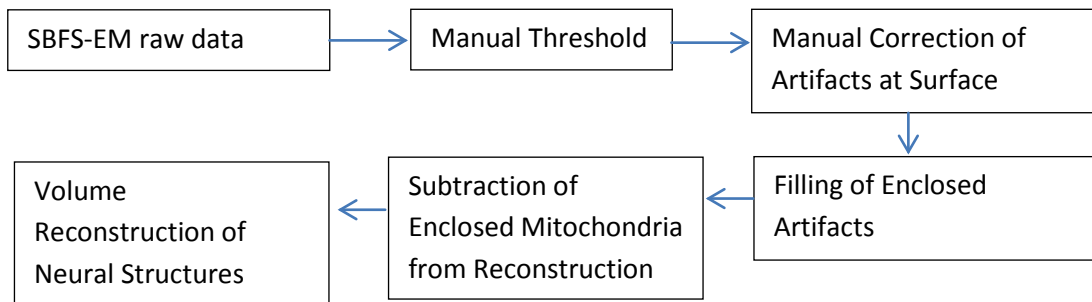


Figure III-8: Volume reconstruction of dendritic structure from SBF-SEM raw data.

Flowchart representing the different steps before the convolution of 3D reconstructed neural structures.

2. Computation of synthetic PSF

The point spread function of microscope like two-Photon Microscopy can be approximated by a 3D Gaussian distribution (Zhang 07). Furthermore, It has been showed that the different sigma of the distribution for the x-, y- and z-axis (where as the z-axis is parallel to the laser direction) is given by the parameters of the microscope (Zipfel, Williams et al. 2003). Therefore the synthetic PSF is defined by a 3D Gaussian distribution and parameters of the imaging system as follow:

$$PSF(x, y, z) = g_{\sigma_p, \sigma_z}(x, y, z) = \exp\left(-\frac{x^2 + y^2}{2\sigma_p^2} - \frac{z^2}{2\sigma_z^2}\right)$$

$$\sigma_p = \begin{cases} \frac{0.320\lambda}{2NA}, & NA \leq 0.7 \\ \frac{0.325\lambda}{2NA^{0.91}}, & NA > 0.7 \end{cases}$$

$$\sigma_z = \frac{0.532\lambda}{2(n - \sqrt{n^2 - NA^2})}$$

The constants are given by (Zipfel, Williams et al. 2003)

3. Convolution

The final computation of the DRFI was done by convolution of reconstructed dendrites with the synthetic PSF. Both can be sampled with high spatial precision. Therefore, also high resolution DRFI is feasible. In the convolved images, absolute intensities cannot be compared with real two-photon microscopy. Therefore, only normalized intensities should be compared (e.g. normalized by average dendritic intensity).

Figure 2 shows the different data we used. It shows the raw data and the manual threshold overlaid (A/B and C/D), the final reconstruction (with enclosed mitochondria in pink, E), the synthetic PSF (viewed from top and side, F and G) and the DRFI (given by the convolution) More details about the process of DRFI generation can be found in our contribution to the Workshop “Microscopic Image Analysis with Applications in Biology (MIAAB)”, (Blumer 11).

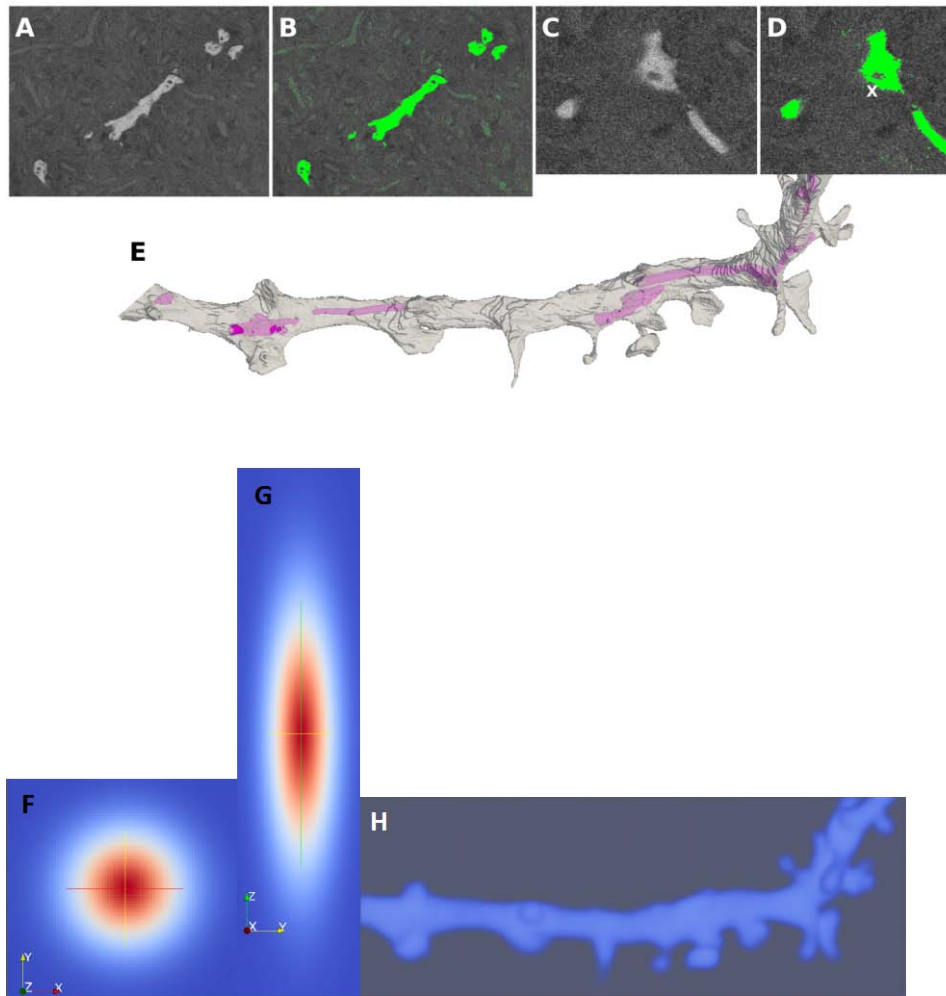


Figure III-9: Images used for computation of the DRFI

(A)(C) Represent SBFS-EM raw data. (B)(D). Manual threshold overlaid. Noted that mitochondria are excluded from the reconstruction. (e) EM reconstruction with mitochondria enclosed in the dendrite. (F) and (G) represent the synthetic PSF (viewed from top and side, F and G).(H) DRFI after convolution with the synthetic PSF. Courtesy of Clemens Blumer

4. Measurements of Spine Intensity in 2-Photon Images and DRFI

We performed manual measurements of spine intensities for our studies. The goal was to compare spine-to-dendrite intensity ratios from real data to our synthetic data. The (normalized) spine intensity values were measured with the following procedure:

1. Measure average dendrite intensity in dataset

The average dendrite intensity was estimated by computing the average intensity along a part of the backbone (centerline) of the dendrite. This ensures that all spine intensities within the dataset were normalized with the same value and the average

dendrite intensity was less dependent on the selected voxels as it represents a larger region.

2. Measure spine intensity in different slices, using local maxima

In (typically) 3 slices a small region (4x4 voxels) the average intensity was computed. This corresponds to the average intensity of a 4x4x3 voxel region. The box was placed at the local highest intensities for the spine but as far away as possible from the dendrite. By this procedure the measurement takes place in the center of the spine head.

3. Normalize spine intensity with average dendrite intensity

The measured spine intensity is normalized with the average dendrite intensity of the dataset. Then a comparison between measurements from 2-Photon Microscopy and DRFI was possible.

To compare measurements between 2-Photon Microscopy data and the corresponding DRFI the reconstruction was manually aligned to the fluorescence image. Then the intensities were measured with the steps described above. The measurement was difficult for vertical oriented spines. Therefore, we measured only spines with a horizontal orientation. (**Figure III-10**) gives an overview about the selection of spines to be measured. (**Figure III-11**) gives an overview about the steps to do a measurement in a 2-Photon Microscopy image or a DRFI.

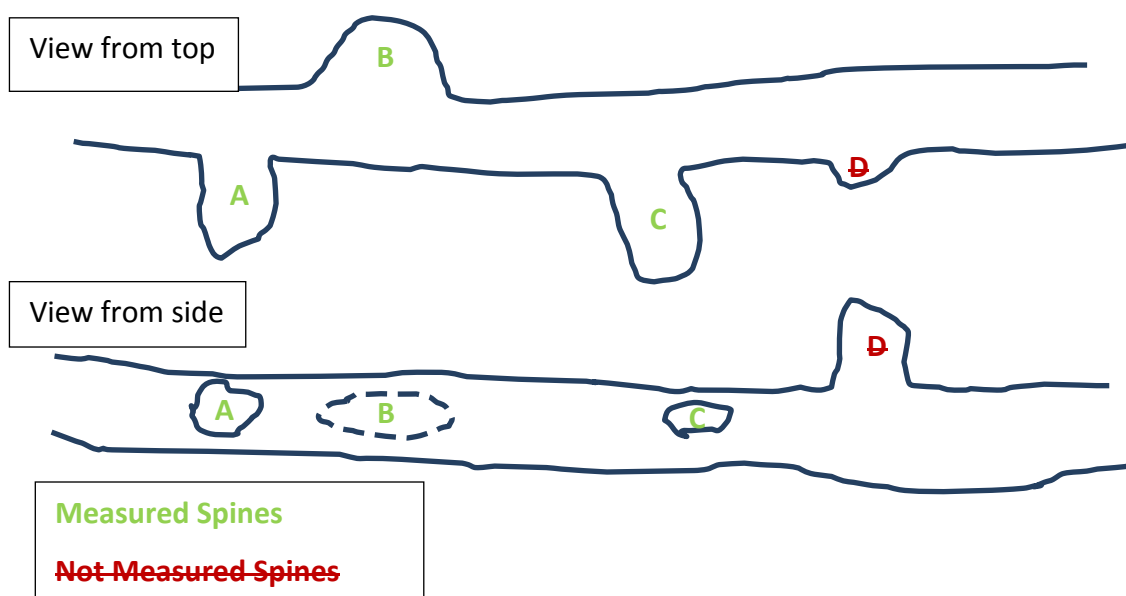


Figure III-10: Selection of spines to be measured

Top row: View from top. Bottom row: View from side. Courtesy of Clemens Blumer

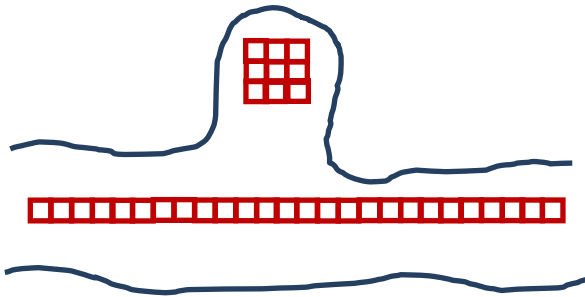


Figure III-11: Intensity measurement in two-photon or DRFI images

Red square represent voxels used to measure (normalized) spine intensities.

Courtesy of Clemens Blumer

H. Statistical analysis.

Analysis of the morphological and correlative data set comparison were performed with Graphpad prism v5.0. Correlation analysis between the parameters quantified was performed with non-parametric Spearman analysis since most parameters did not exhibit a normal distribution. Significant correlations were classified as weak (Spearman rho(r) value lower than 0.40), moderate ($0.4 < r < 0.7$) and strong ($r > 0.7$).

IV. Results

A. Direct measurement of coupling between dendritic spines and dendrites.

We examined the compartmentalization of dendritic spines in rat hippocampal pyramidal neurons. Neurons were filled with alexa dye via a patch pipette and diffused freely inside the neuron. Two-photon laser scanning microscopy with illumination at 810 nm was used to excite alexa 594 revealing dendrites and spines that fluoresce in the red spectrum (**Figure IV-1.A**). Following the fluorescence in individual spine with a line-scan mode, a brief focal increase in the laser power bleached alexa which led to a decrease in fluorescence restricted to the head. The fluorescence recovered as bleached and unbleached fluorophores mixed by diffusion through the spine neck. The decay of the fluorescent transient decrease in the spine head was well fitted by a single exponential yielding a time constant of equilibration for alexa $\tau_{\text{equ}}(\text{alexa})$. It can be noted that any given pair of spines that did not look noticeably different under two-photon microscopy could still had a huge difference in $\tau_{\text{equ}}(\text{alexa})$ (**Figure IV-1.A**). Repeated measurements in individual spines yielded consistent values of $\tau_{\text{equ}}(\text{alexa})$ with a coefficients of variation (CVs) of 10 to 15% (**Figure IV-1.B**). Conversely $\tau_{\text{equ}}(\text{alexa})$ varied over a broad range from spine to spine. Within the same neuron, measurement of $\tau_{\text{equ}}(\text{alexa})$ along a dendrite revealed a huge heterogeneity (**Figure IV-1.C**). In a population study $\tau_{\text{equ}}(\text{alexa})$ ranged from 4 to 408 ms with a median of 49 ms. The 25th and 75th percentiles were respectively 24 and 84 ms (**Figure IV-1 D**, n=5/287 cells/spines) which led to a 40 fold differences between weak and strongly compartmentalized spines.

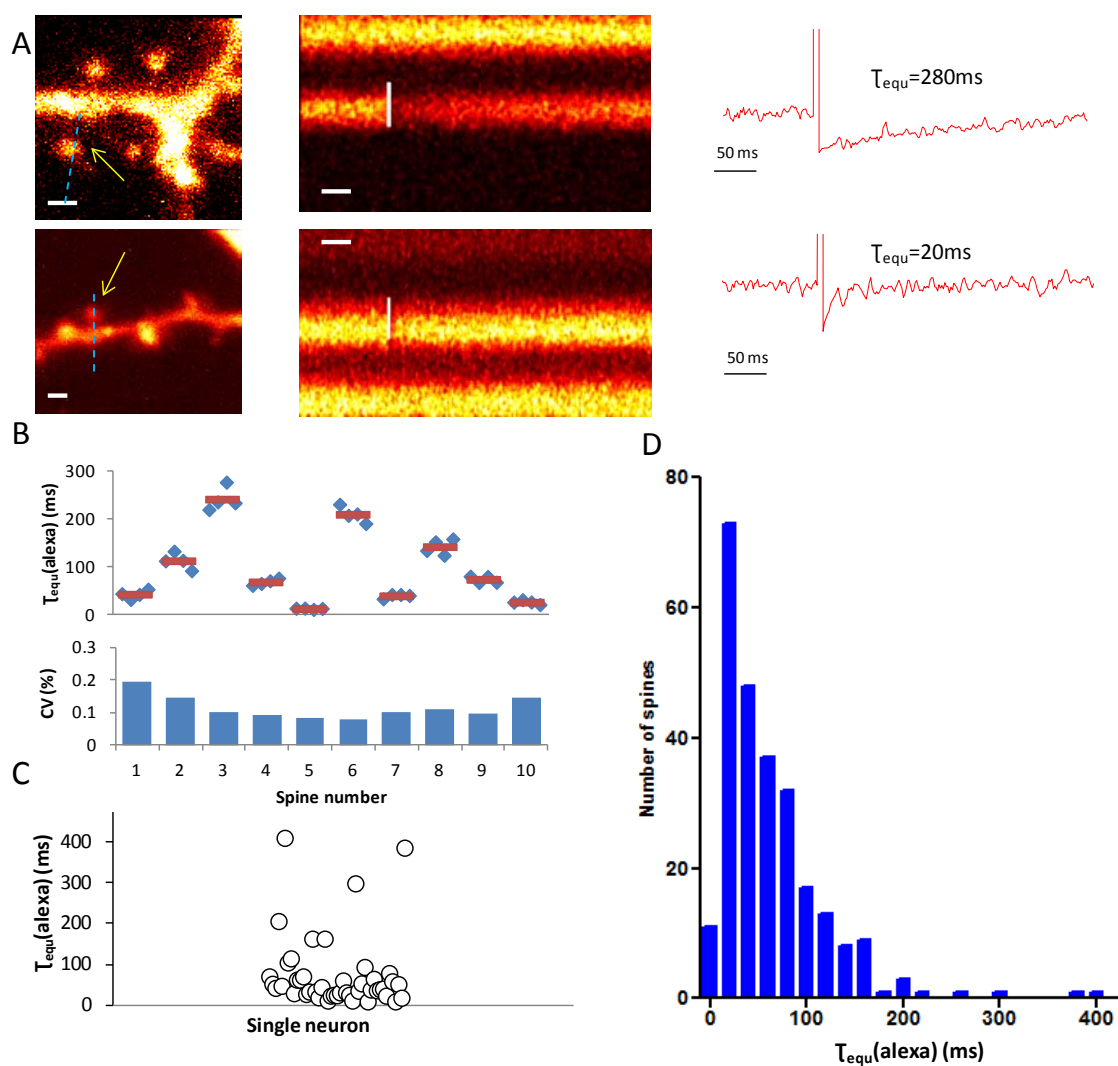


Figure IV-1: Measurement of Alexa 594 diffusion through the spine neck reveals heterogeneity of spine/dendrite diffusional coupling.

(A) images of spine/dendrite pairs that demonstrate weak (top) and strong (bottom) diffusional coupling. The arrow indicates the site of bleaching. Scale bar, 1 μm . Fluorescence measured with a high temporal resolution in line scans over regions indicated by a dashed line during the bleaching of Alexa in the spine head. Scale bar 50 ms. Quantification of the Alexa fluorescence decrease in the spine head. (B) Repeated measurements of $\tau_{\text{equ}}(\text{Alexa})$ (4x) in 10 spines. For each spine, the values of τ_{equ} obtained from each independent measurement (blue point), the average (red) and the CV of τ_{equ} (bottom) are shown. (D) Distribution of $\tau_{\text{equ}}(\text{Alexa})$ on the same neuron along the same dendrite. (E) Distribution of $\tau_{\text{equ}}(\text{Alexa})$ for spines diffusional coupling measured in several neurons.

B. Correlative microscopy

We hypothesized that the heterogeneity of $\tau_{\text{equ}}(\text{Alexa})$ was caused by the different morphology of the spines. A thin and/or a long spine neck should increase the time it takes for molecules to escape into the dendrite. Changes of spine morphology might account for the observed changes in $\tau_{\text{equ}}(\text{Alexa})$. However, spine neck parameters are not resolvable with two-photon microscopy. Only electron microscopy can resolve fine details of spine necks. We used a correlative approach combining $\tau_{\text{equ}}(\text{Alexa})$ measurements with two-photon microscopy and spine detail structural measurements by electron microscopy on the same spines to investigate the origin of $\tau_{\text{equ}}(\text{Alexa})$ heterogeneity. For this purpose we filled neurons with Alexa and neurobiotin through a patch pipette. Alexa 594 (fluorescent dye) was imaged with two-photon microscopy. The location of every spine was registered with series of image stacks along the dendrite, after which the neuron was fixed. **(Figure IV-2A.B.C)**. Neurobiotin, which is not visible by two-photon microscopy since it is not fluorescent allowed us to specifically stain the previously imaged neuron with an electron dense black precipitate using DAB staining, **(Figure IV-2.D)**. The neuron was completely black, making it possible to localize the previously imaged piece of dendrite that had to be trimmed for serial section imaging in the SBFSEM. Since the staining was electron dense it gave a very nice contrast against the surrounding tissue revealing spines fine structures. After 3D reconstruction, **(Figure IV-2.E)** spine detailed morphology was measured and the correlation with spine compartmentalization was possible **(Figure IV-2.F)**.

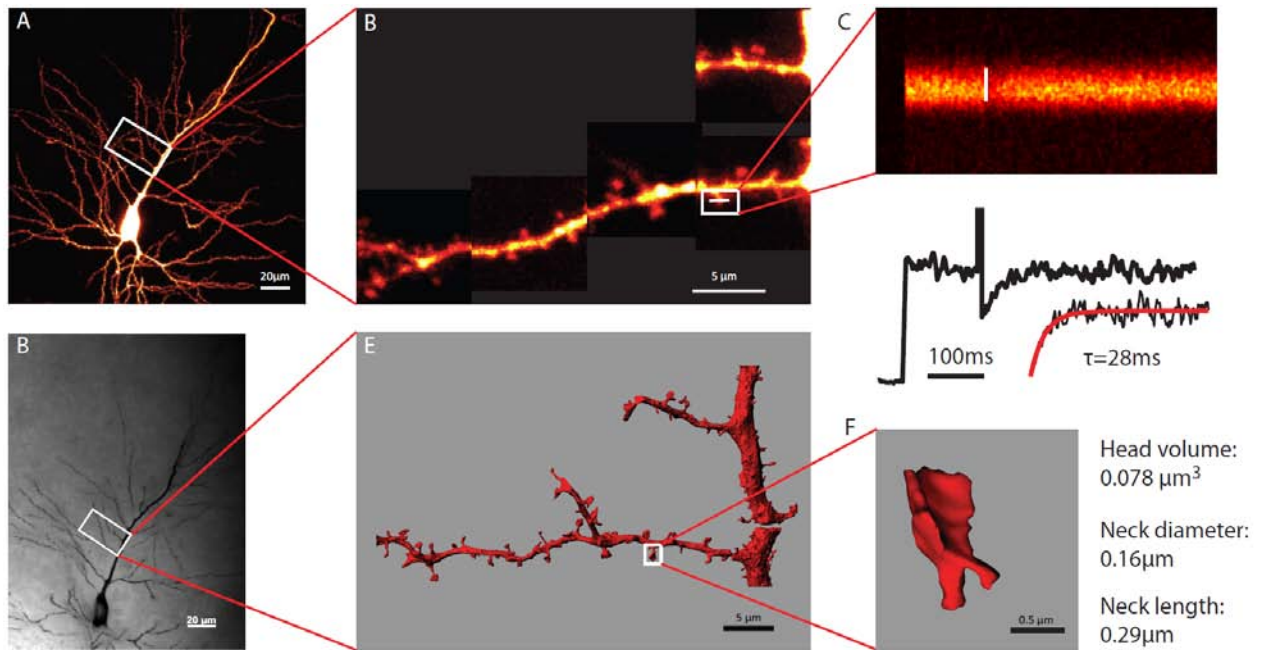


Figure IV-2: Correlative microscopy

(A) Max projection of a neuron filled with Alexa 594 and neurobiotin through a patch pipette. The location of a selected piece of dendrite where diffusional coupling measurements took place was recorded (B) Positions of dendritic spines on a piece of dendrite were documented by taking image stacks. (C) Diffusional measurement of spines along the dendrite. The fluorescence recovery was fitted by a single exponential. (D) After DAB staining against neurobiotin the previously imaged neuron was easily identifiable and the dendrite of interest could be easily located. (E) 3D reconstruction from high resolution image stack taken from SBFSEM. It was possible to identify spines where $\tau_{\text{equ}}(\text{Alexa})$ was measured. (F) 3D structure of a dendritic spine. Neck diameter and length could be measured precisely.

C. Analysis of ultrastructural reconstruction of dendritic spines in CA1 pyramidal neurons.

Since neurons were specifically stained, all reconstructed dendritic spines came from a known cell type and location: apical dendrites from 3-4 weeks old CA1 hippocampal pyramidal neurons. Dendritic spines exist in a huge variety of shapes and sizes even on the same dendrite. In our subset of reconstructed dendritic spines (30 spines from 4 cells) the spine head volume ranged from 0.01 to 0.34 μm^3 with an average of $0.11 \pm 0.096 \mu\text{m}^3$ (mean \pm SD). The neck length and diameter were also very variable. The spine neck length ranged from 0.11 to 1.84 μm with an average of $0.48 \pm 0.33 \mu\text{m}$. Since the neck diameter is not always constant along its length, we estimated the average diameter for each spine (see Materials and Methods). Spine neck diameter ranged from 0.09 to 0.38 with an average value of $0.21 \pm 0.06 \mu\text{m}$ (**Table 1**).

Table 1: Summary of spine morphological variables and compartmentalization

Spine parameters	N	Mean \pm SD	Range
Head volume (μm^3)	30	0.11 ± 0.096	0.01 - 0.34
Neck diameter (μm)	30	0.21 ± 0.06	0.09 - 0.38
Neck length (μm)	30	0.48 ± 0.33	0.11 - 1.84
Recovery time constant (ms)	30	61 ± 79	13 -372

Since spine morphology possibly regulates its degree of compartmentalization, we first examined if there was correlation between spine head and neck morphologies in our data set. For example, do spines with a big head have longer or wider necks? We plotted the spine head volume versus neck length and diameter. We detected a weak but significant correlation between head volume and neck diameter ($r=0.4$; $p<0.05$) whereas no correlation was found between head volume and neck length ($r=0.17$; $p=0.18$). Bigger spines seems to have wider necks on average. Spine neck length and diameter were not correlated ($r=-0.07$; $p=0.35$). Thus, for each spine it appears that the spine neck length and diameter were independently regulated (**Figure IV-3.A**)

For each reconstructed spine, we also knew the degree of compartmentalization. We tested whether specific morphological parameters dominantly, control the residence time

of small molecules inside the spine. For this purpose, we plotted the different spine parameters versus $\tau_{\text{equ}}(\text{Alexa})$. In this analysis, we found a moderate correlation between spine head volume and $\tau_{\text{equ}}(\text{Alexa})$ ($r=0.59$; $p<0.0005$) and a weak correlation between spine neck length and $\tau_{\text{equ}}(\text{Alexa})$ ($r=0.5062$; $p<0.005$). No correlation was found between spine neck diameter and $\tau_{\text{equ}}(\text{Alexa})$ ($r=0.02$; $p=0.45$) (**Figure IV-3.B**)

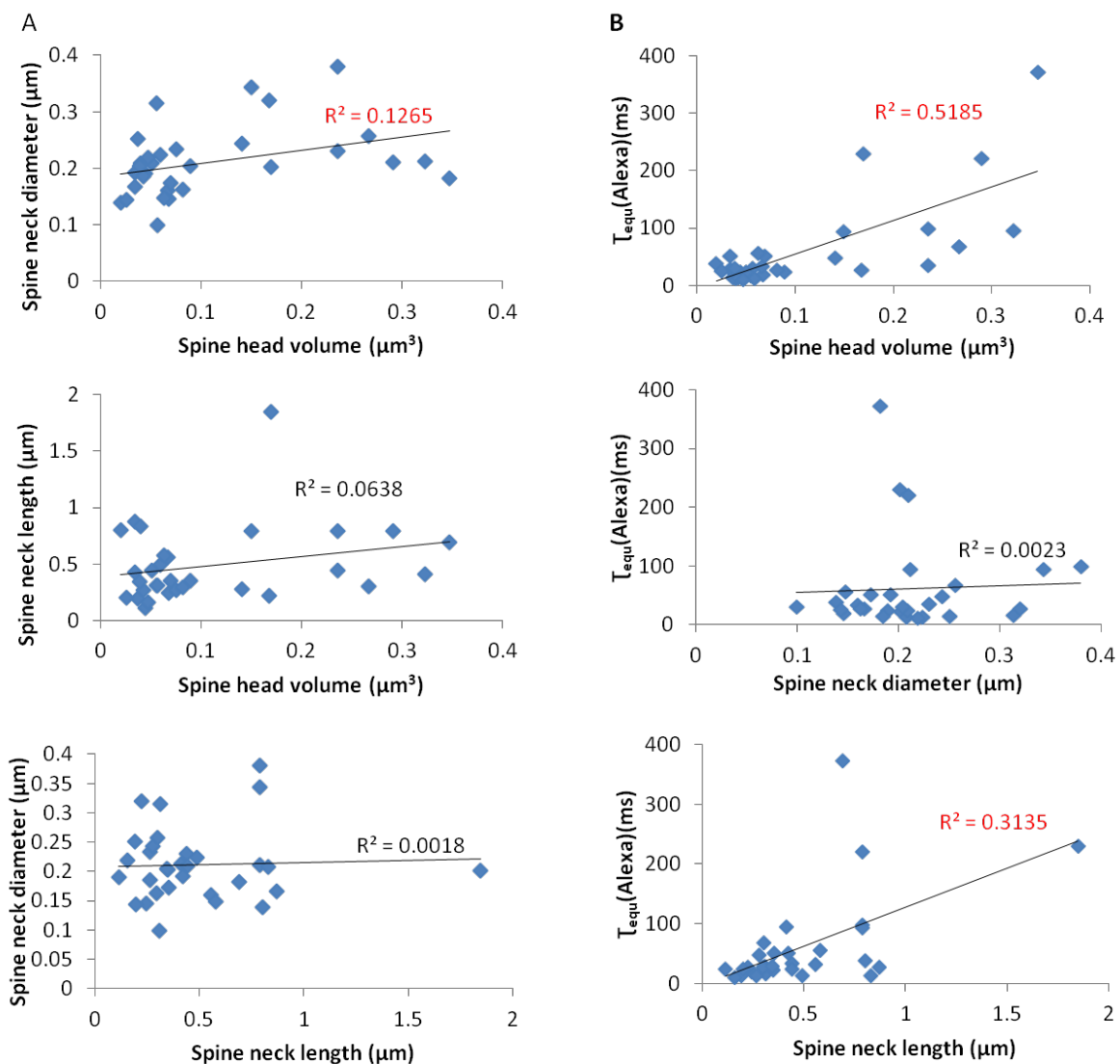


Figure IV-3: Relationship between spine morphological variables and compartmentalization.

Dendritic spine parameters are plotted versus each others to investigate potential co regulation of the spine morphology (B) Dendritic spine parameters are plotted versus the recovery time constant to investigate the role of spine parameters on compartmentalization. Linear regression fit and R^2 are plotted. R^2 in red are statistically significant.

Thus, spine head volume has a strong influence on $T_{\text{equ}}(\text{Alexa})$. This result was expected, since a bigger reservoir takes more time to fill it with unbleached fluorophores. A correlation with the spine neck length was also expected, as longer spine necks increase the distance that molecules have to travel between spine head and parent dendrite. The lack of correlation between $T_{\text{equ}}(\text{Alexa})$ and spine neck diameter seems to be counterintuitive, but theoretical studies have suggested that spine neck diameters does not influence particles movements inside the neck, but rather controls the times they spend in the head by setting the small windows where they can escape (Biess, Korkotian et al. 2007; Schuss, Singer et al. 2007) . The ratio spine head volume/neck diameter should strongly influence $T_{\text{equ}}(\text{Alexa})$. To test this hypothesis, we plotted the ratio head volume/neck diameter versus T_{equ} . Although there was no correlation between neck diameter and T_{equ} , taking both values into account improved the correlation from $R^2=0.51$ to $R^2=0.63$ ($r=0.61$; $p<0.0005$),(Figure IV-4).

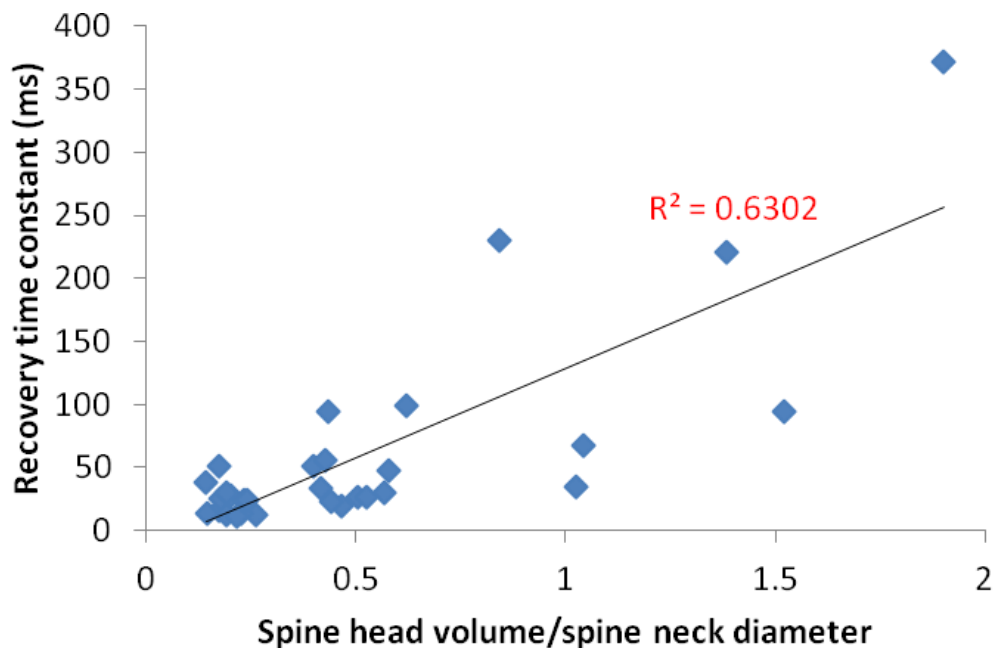


Figure IV-4: ratio spine head volume versus recovery time constant.

T_{equ} (alexa) was plotted versus spine head volume and spine neck diameter ratio. Linear regression fit and R^2 are plotted

D. Dendritic spine morphology predicts alexa diffusion out of the spine.

Compartmentalization inside dendritic spines is not well described by taking into account only one morphological parameter. The entire spine morphology has to be considered. The compartmentalization of freely diffusible molecules inside a spine has been studied theoretically and two similar equations have been suggested to calculate τ_{equ} (see methods):

According to Svoboda et al. τ_{equ} can be predicted according to equation (1) (Svoboda, Tank et al. 1996):

$$\tau_{equ} = \frac{V \cdot L}{A \cdot D} \quad (1)$$

Where V is the spine head volume in μm^3 , L is spine neck length in μm , A is the cross sectional area in μm^2 and D is the coefficient of diffusion for the measured particle in $\mu\text{m}^2 \cdot \text{s}^{-1}$.

According to Holcman τ_{equ} can be predicted according to equation (2) (Biess, Korkotian et al. 2007):

$$\tau_{equ} = \frac{V \cdot L}{4 \cdot D \cdot \alpha \cdot \epsilon^2} + \frac{L^2}{2 \cdot D} \quad (2)$$

τ_{equ} is described as the sum of the mean sojourn time of particles inside the head and inside the neck. The first product represents the time of particles inside the head where V is the spine head volume in μm^3 , L is spine neck length in μm , and D is the coefficient of diffusion of particles inside the head. The second product represents the time particles spend inside the spine neck where L is the spine neck length and D the coefficient of diffusion for the molecule inside the neck. We were able to test these formulas since we had detailed spine

morphology and the associated measurement of compartmentalization. The coefficient of diffusion of alexa has been measured in the cytoplasm (Nitsche, Chang et al. 2004) but neurons with this particular shape could have a cytoplasm with different properties, perhaps owing differences in their cytoskeletons. Change in the cytoplasm composition could interfere with the movements of molecules (Nitsche, Chang et al. 2004). As a consequence the coefficient of diffusion for Alexa 594 in a neuronal dendrite could differ from that measured in the cytoplasm of other cells. To measure the coefficient of diffusion in pyramidal neuron dendrites we bleached Alexa contained within the dendrite. We selected an aspiny dendrite to avoid any anomalous diffusion created by spines, which would make it difficult to measure the real coefficient diffusion for Alexa (Santamaria, Wils et al. 2006). A small portion of the dendrite was bleached which an increase in the laser power. We monitored the spread of bleached molecules along the dendrite with high temporal resolution. The calculated diffusion coefficient of Alexa (D_{Alexa}) within pyramidal neurons ranged from 130 to 240 $\mu\text{m}^2 \cdot \text{s}^{-1}$ with an average of $173.63 \pm 41 \mu\text{m}^2 \cdot \text{s}^{-1}$ (n=6), approximately 72% of the values previously measured (Weber, Chang et al. 2004).

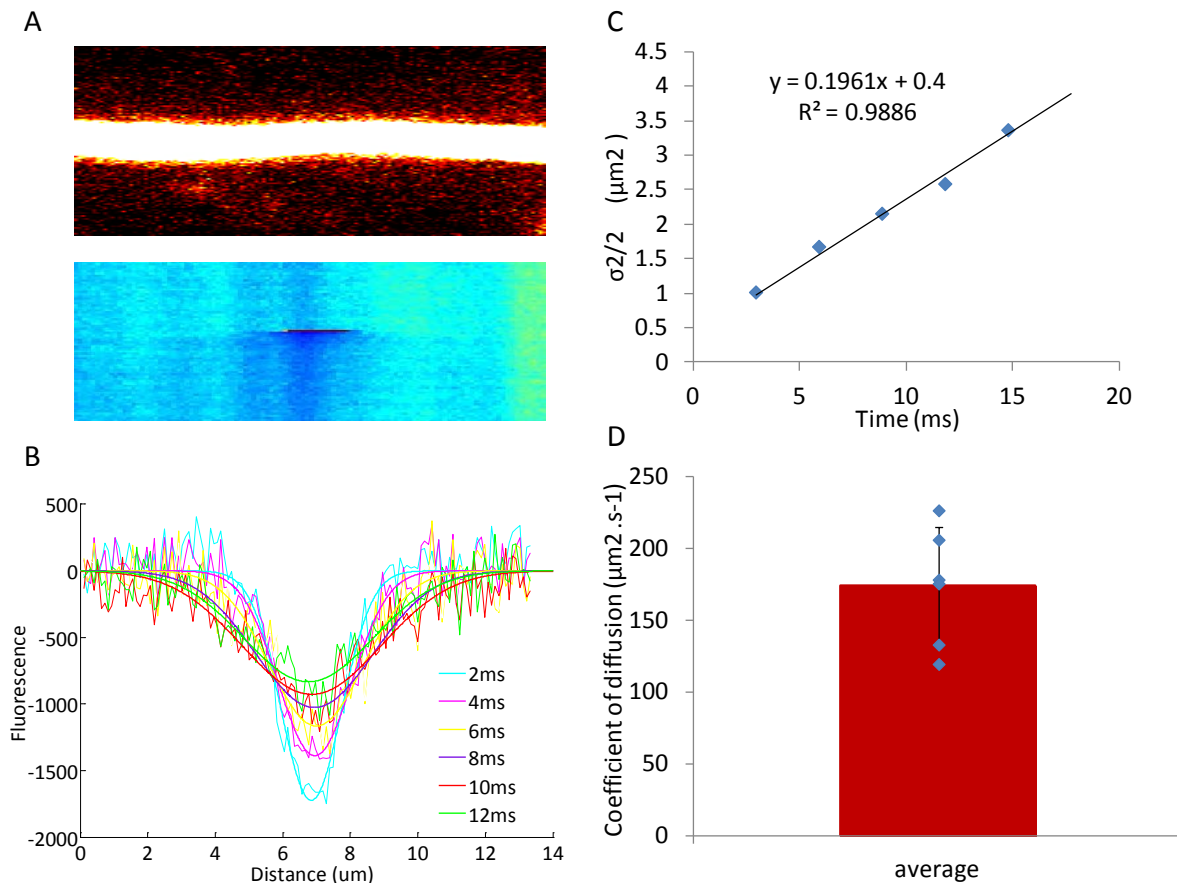


Figure IV-5: Measurement of coefficient of diffusion in dendrite.

(A) An aspiny dendrite was selected; major apical dendrite. The fluorescence along the dendrite was monitored using a line scan mode allowing high temporal resolution. A brief increase in the laser power bleached a small volume of fluorophores in the dendrite. The diffusion of bleached fluorophores is visible over time (B) Intensity profile along the dendrite at various time after photobleaching (noisy line). Smooth lines are Gaussian fit. (C) $\Delta(\sigma^2/2)$ versus time after photobleaching. The slope gives the coefficient of diffusion. (D) Coefficient of diffusion for Alexa from 6 different cells. (Average and standard deviation)

With the measurement of D_{Alexa} all the relevant parameters are known and we can investigate if spine morphology predicts the compartmentalization of molecules inside the head.

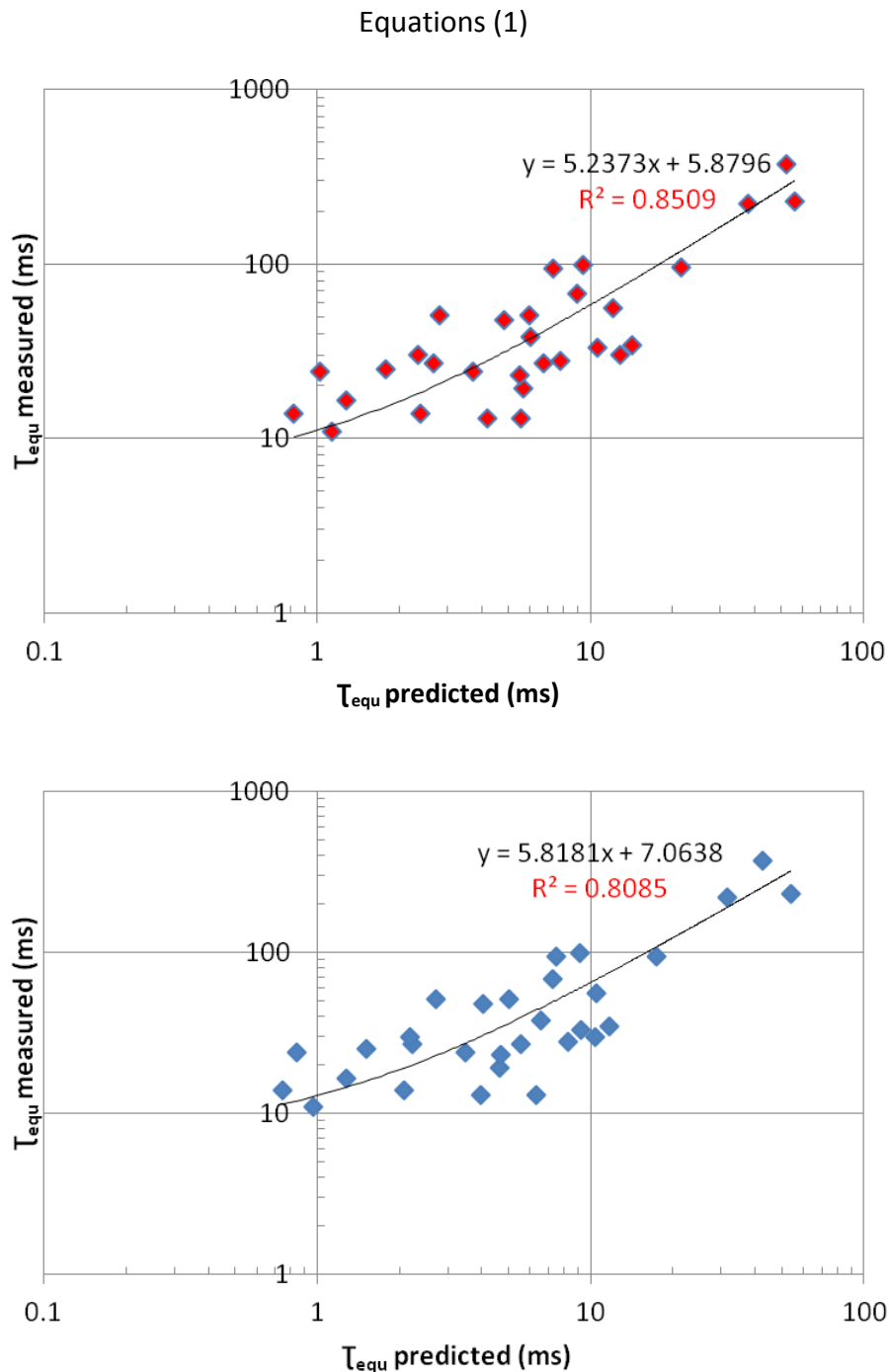


Figure IV-6: Spine morphology predicts the movements of Alexa.

T_{equ} predicted computed from equation (1) and (2) with morphological data for 3D EM reconstruction are plotted versus T_{equ} measured with two-photon microscopy

Spines morphologies are tested with equations (1) and (2). Using equation (1) T_{equ} predicted (alexa) ranged from 0.82 to 56 ms with an average of 10.27 ± 13.8 ms ($n=4/30$ cells/spines). Using Equation (2) T_{equ} predicted(Alexa) ranged from 0.74 to 54 ms with an average of 9 ± 12 ms ($n=30$). T_{equ} measured(Alexa) ranged from 11 to 371 ms with an average of 61 ± 79 ms .

To investigate if spine morphologies explain the heterogeneity of $\tau_{\text{equ}}^{\text{measured}}(\text{alexa})$ we plotted $\tau_{\text{equ}}^{\text{measured}}(\text{alexa})$ versus $\tau_{\text{equ}}^{\text{predicted}}(\text{alexa})$ for both equations. We found strong correlations with equation (1) ($r=0.7533$; $p<0.0001$) and equation (2) ($r=0.74$; $p<0.0001$). The linear regression was found slightly better with equation (1) than equation (2), 0.85 versus 0.80 (**Figure IV-1**). Strong correlation between $\tau_{\text{equ}}^{\text{measured}}(\text{Alexa})$ and $\tau_{\text{equ}}^{\text{predicted}}(\text{Alexa})$ indicates that the morphology of a dendritic spine predicts the time that alexa takes to diffuse out of the spine and also that Alexa diffuses freely inside the entire cytoplasm of a dendritic spine. However, the slope of the linear regression was not equal to 1, but 5.23 for equation (1) and 5.81 for equation (2). Thus $\tau_{\text{equ}}^{\text{measured}}(\text{Alexa})$ was 5.5 times slower than $\tau_{\text{equ}}^{\text{predicted}}(\text{Alexa})$. Going back to equations (1) and (2) this large difference is likely due to one parameter we could not directly measure, the coefficient of diffusion of Alexa inside the spine. D_{Alexa} was measured inside aspiny dendrites, assuming that it was homogenous inside the entire cell. D is defined by the equation (3):

$$D = kT (6\pi r \eta)^{-1} \quad (3)$$

Where K is the Boltzman constant in $\text{m}^2\text{kg}\cdot\text{s}^{-2}$, T is the absolute temperature, r is the Stokes radius of the molecule in μm , and η is viscosity in $\text{kg}/(\text{s}\cdot\text{m})$. We explain the difference between $\tau_{\text{equ}}^{\text{measured}}(\text{Alexa})$ and $\tau_{\text{equ}}^{\text{predicted}}(\text{Alexa})$ by a difference in D_{Alexa} between spines and dendrites. We could calculate D_{Alexa} inside the spine using equation 1, and in our reconstructed spines we found that D_{Alexa} ranged from 9 to $72 \mu\text{m}^2\cdot\text{s}^{-1}$ with an average of $32 \pm 27 \mu\text{m}^2\cdot\text{s}^{-1}$. The movement of Alexa inside spines is slowed down by a factor of 5.4 compared to dendrites. Since K is constant, the size of Alexa and temperature are all the same between dendrites and spines, the difference in D indicates a difference in cytoplasmic viscosity between spines and dendrites. Since the cytoplasm is a macromolecular complex and viscosity is most commonly used to describe the biophysical properties of homogeneous medium we prefer to talk about “apparent viscosity” increase. The cytoplasm inside dendritic spines must differ from that which is inside the dendrites.

E. Movements of larger and positively charged molecules are also slowed down inside spines.

We have seen previously that diffusion of Alexa dyes out of the spine was regulated by its morphology and also slowed down by a factor of 5.4. Alexa dyes are polar molecules with a Stokes radius of approximately 0.8 nm and carry 2 negative charges (Heyman and Burt 2008). We were interested to know if the movement of small biologically active particles such as small ions or bigger molecules such as small enzymes were also regulated by spine morphology and generally slowed down.

To get a closer look at the movement of ions we used a small dye: N,N,N-Trimethyl-2-[methyl(7-nitrobenzo[c][1,2,5]oxadiazol-4-yl)amino]ethanaminium Iodide (NBD-MTMA) (Aavula, Ali et al. 2006). This dye has a Stokes radius of approximately 0.43nm and carries one positive charge (Heyman and Burt 2008). The ionic radius of Na^+ is approximately 0.09 nm (Conway 1981), but in solution ions attract water molecules, which form a hydration sphere. The apparent stokes radius is increased and ions act like bigger molecules and thus their speed of diffusion is decreased. The stokes Radius of Na^+ in solution is approximately 0.36 nm (Conway 1981). Thus NBD-MTMA is close to Na^+ ions in terms of size and charge carried. We infused CA1 pyramidal neurons with an intracellular solution containing Alexa and NBD-MTMA . We successively bleached Alexa ($\tau_{\text{equ,measured}}(\text{Alexa})$) and NBD-MTMA ($\tau_{\text{equ,measured}}(\text{NBD-MTMA})$) in the same spine. In our population (n=5/61 cells / spines) $\tau_{\text{equ,measured}}(\text{Alexa})$ ranged from 22 to 241ms with an average of 95 ± 48 ms. $\tau_{\text{equ,measured}}(\text{NBD-MTMA})$ ranged from 8 to 66 ms with an average of 25 ± 13 ms. We plotted $\tau_{\text{equ,measured}}(\text{Alexa})$ versus $\tau_{\text{equ,measured}}(\text{NBD-MTMA})$. We found a strong correlation between $\tau_{\text{equ,measured}}(\text{Alexa})$ and $\tau_{\text{equ,measured}}(\text{NBD-MTMA})$ ($r=0.8609$; $p<0.0001$) (**Figure IV.7**). We have seen previously that compartmentalization of Alexa inside spines is dependent upon spine morphology. Strong correlation between both fluorophores indicates that the compartmentalization of small positively charged molecules is also controlled by spines shape. We were also interested to know if NBD-MTMA was also slowed down inside spines in a similar way as Alexa. Since the Stokes radius of both molecules has been described in the literature we could calculate $\tau_{\text{equ,predicted}}(\text{NBD-MTMA})$ (plotted as red square in figure III-7) from $\tau_{\text{equ,measured}}(\text{Alexa})$. We calculated that NBD-MTMA should be 1.7 times faster than Alexa, and measured 4 times faster diffusion. Since the Stokes radius of NBD-MTMA has not been measured experimentally, we cannot be

sure whether this difference is due to a poor estimate of the hydrodynamic radius or truly indicates strong charge effects inside the spine, retarding negatively charged particles more than positively charged ones.

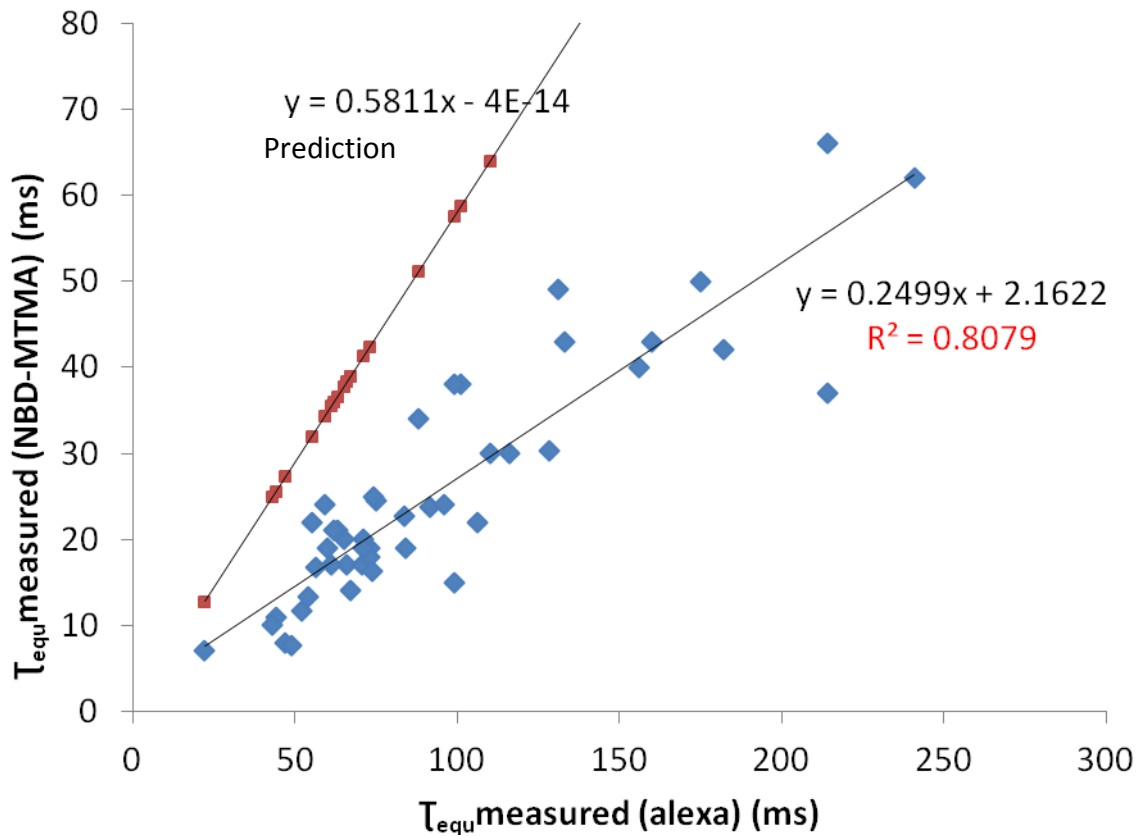


Figure IV-7: Correlation between Alexa and NBD-MTMA

$T_{equ} \text{ measured (NBD-MTMA)}$ is plotted versus $T_{equ} \text{ measured (Alexa)}$ (blue square) . Linear regression fit, R^2 and $T_{equ} \text{ predicted (NBD-MTMA)}$ are plotted (red square).

To investigate the compartmentalization of bigger molecules such as small enzymes, we used the following genetically encoded fluorophores: PA-GFP, RFP (27kDa) and Alexa coupled to 70 KDa dextran.

To begin with, we investigated whether large molecules of similar size have the same behavior inside dendritic spines. In CA1 pyramidal neuron transfected with PA-GFP and RFP, we photoactivated PA-GFP and bleached RFP at the same time in the same spine (**Figure IV.8.a**). In our population (n=3/110 cells spines) $T_{equ} \text{ measured (PA-GFP)}$ ranged from 44 to 502 ms with an average of 159 ± 103 ms and $T_{equ} \text{ measured (RFP)}$ ranged from 28 to 469 ms with an average of 161.47 ± 109 ms. We plotted $T_{equ} \text{ measured (PA-GFP)}$ versus

$\tau_{\text{equ}}^{\text{measured}}(\text{RFP})$ to investigate a possible correlation between both parameters. We found a strong correlation ($r=0.977$; $p<0.0001$, $n=110$) with a slope of the linear fit equal to 1, indicating that molecules of similar size behave in a similar way inside dendritic spine.

The cytoplasm of a cell is a highly crowded environment (Ellis 2001) and it has been shown that dendritic spines possess a very high concentration of actin (Fischer, Kaech et al. 1998). Large molecules can be more sensitive to a crowded environment than smaller molecules (Popov and Poo 1992) like Alexa. Thus molecules of different sizes could behave differently inside the cytoplasm of a dendritic spine. To test this hypothesis we measured the compartmentalization of molecules of different sizes. First, we infused Alexa into CA1 pyramidal neurons transfected with PA-GFP and RFP. We bleached Alexa and photoactivated PA-GFP successively in the same spine to measure compartmentalization for both fluorophores (**figure IV.8.b**). In our population ($n=3/55$ cells/spines), $\tau_{\text{equ}}^{\text{measured}}(\text{Alexa})$ ranged from 8 to 52 ms with an average of 25 ± 14 ms. $\tau_{\text{equ}}^{\text{measured}}(\text{PA-GFP})$ ranged from 21 to 414 ms with an average of 96 ± 83 ms. We plotted $\tau_{\text{equ}}^{\text{measured}}(\text{Alexa})$ versus $\tau_{\text{equ}}^{\text{measured}}(\text{PA-GFP})$ and found a moderate correlation ($r=0.57$; $p<0.0001$, $n=55$) with $R^2=0.40$. Since $\tau_{\text{equ}}^{\text{measured}}(\text{Alexa})$ was highly correlated with the morphology of the spine, a moderate correlation indicated that the compartmentalization of PA-GFP was regulated by spine morphology but also by other factors that differed from spine to spine. Based on the Stokes radius of Alexa and PA-GFP, we calculated $\tau_{\text{equ}}^{\text{predicted}}(\text{PA-GFP})$. Since literature values for the Stokes radius of PA-GFP are not consistent, we plotted two extreme predictions (fast and slow prediction). Although the majority of $\tau_{\text{equ}}^{\text{measured}}(\text{PA-GFP})$ were included inside this range, some measurements are out of bounds and appear even much slower (red point on the right side of slow prediction curve), indicating that some spines retain PA-GFP very efficiently. To confirm this observation we measured the diffusion of 70 kDa dextran coupled to a green Alexa dye.

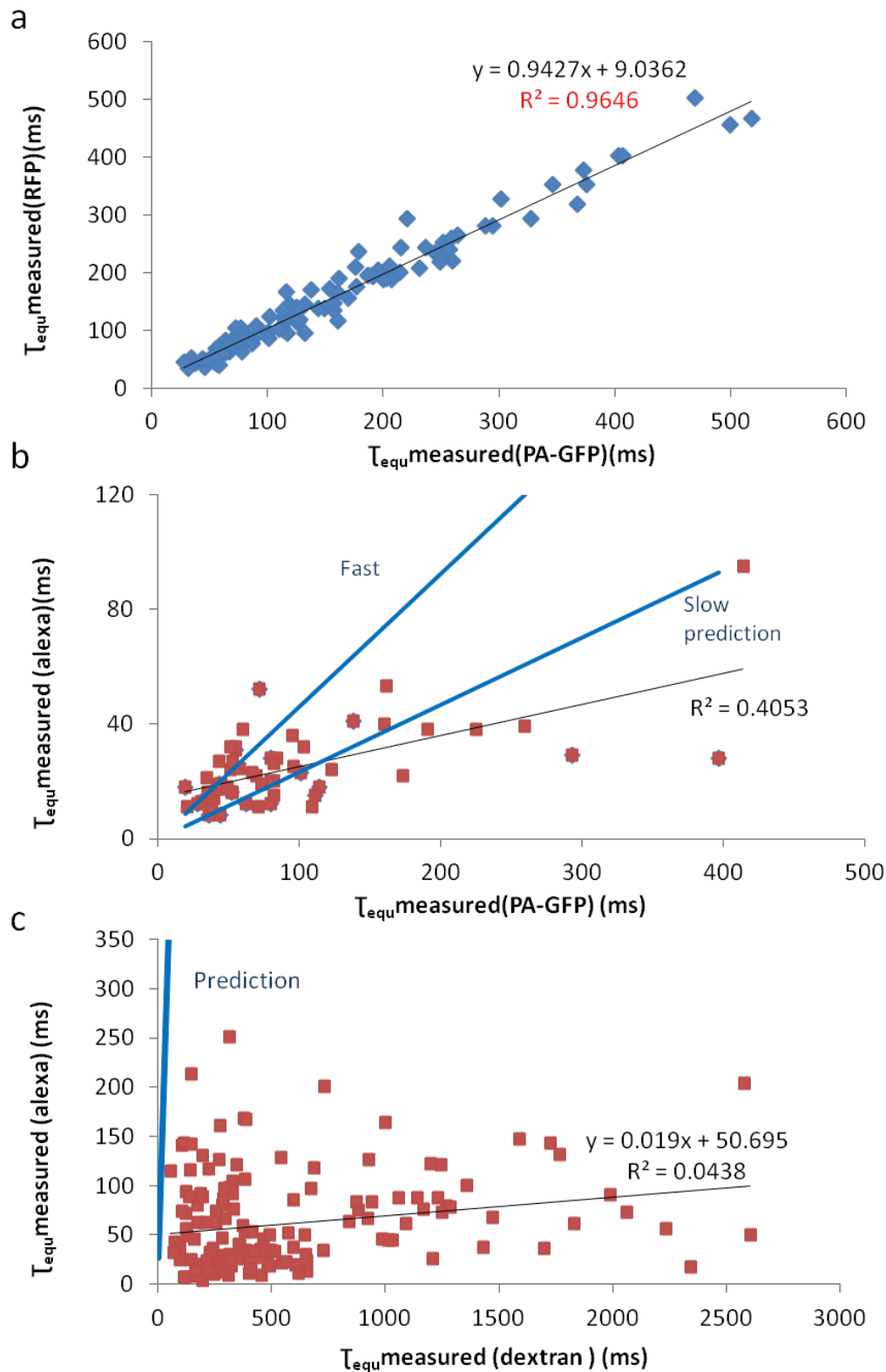


Figure IV-8: Diffusion of large molecules can not be predicted from spine shape.

(a) $T_{equ} \text{ measured (RFP)}$ is plotted versus $T_{equ} \text{ measured (PA-GFP)}$. Linear regression fit and R^2 are plotted. (b) $T_{equ} \text{ measured (alexa)}$ is plotted versus $T_{equ} \text{ measured (PA-GFP)}$. Linear regression fit, R^2 and $T_{equ} \text{ predicted (PA-GFP)}$ (in blue) are plotted. (c) $T_{equ} \text{ measured (alexa)}$ is plotted versus $T_{equ} \text{ measured (dextran)}$. Linear regression fit, R^2 and $T_{equ} \text{ predicted (dextran)}$ (in blue) are plotted. Dextran data were provided by Dr Michael Avermann.

We were able to FRAP red and green Alexa at the same time (**Figure IV.8.c**). In our population (n=3/154 cells/spines) $\tau_{\text{equ}}^{\text{measured}}(\text{Alexa})$ ranged from 7 to 250 ms with an average of 61 ± 48 ms. $\tau_{\text{equ}}^{\text{measured}}(\text{dextran})$ ranged from 127 to 2600 ms with an average of 570 ± 532 ms. Plotting $\tau_{\text{equ}}^{\text{measured}}(\text{Alexa})$ versus $\tau_{\text{equ}}^{\text{measured}}(\text{dextran})$ showed that diffusion of the two different probes was almost completely uncorrelated ($r=0.19$, $p<0.01$, $n=154$). We calculated $\tau_{\text{equ}}^{\text{predicted}}(\text{dextran})$ based on the Stokes radius of Alexa and dextran (70 KDa). The prediction was much faster than the measurements as all red points are on the right side of the prediction. Thus, the diffusion of large molecules is only weakly influenced by spine morphology. Large molecules seem to be retained inside spines for very long times, and their compartmentalization varies from spine to spine, indicating a filter or block in some spines that is invisible to the light microscope.

In conclusion, the compartmentalization of small molecules is controlled by the morphology of the spine, but diffusion is slowed down compared to the dendrite. On top of this effect that is likely caused by a uniformly high viscosity of spine cytoplasm, bigger molecules were subject to another level of regulation. This additional filter for large molecules seems to exist only in a subset of spines.

F. Estimation of dendritic spine neck resistance.

A close analogy exists between diffusion of small fluorophores driven by concentration gradients and electrical currents driven by electrical potentials gradients (Svoboda, Tank et al. 1996)(Berg 1993). Since we found that the compartmentalization of Alexa and NBD-MTMA are directly correlated with the morphology of dendritic spines we assumed that the cytoplasmic space is equally accessible to ions and small fluorophores. The coefficient of diffusion for alexa and NDB-MTMA were used to calculate the cytoplasmic resistivity (ρ_i) of dendritic spine. We calculated the resistance of the spine neck according to the cable equation as $R_{neck} = \rho_i \text{ spine } L/A$ (see materials and methods for details) assuming three different values for internal resistivity (**Figure IV-9**):

- $\rho_i = 250 \text{ ohm.cm}$: previous estimations of cytoplasmic resistivity (Fromherz and Muller 1994; Major, Larkman et al. 1994). In our population study R_{neck} ranged from 10 to 144 $M\Omega$ with an average of $42 \pm 36 M\Omega$ similar to values derived from morphometry(Harris and Stevens 1989) or diffusional coupling measurement (Svoboda, Tank et al. 1996).
- $\rho_i = 1985 \text{ ohm.cm}$ based on measurement of alexa diffusion inside dendritic spine. R_{neck} ranged from 63 to 824 $M\Omega$ with an average of $257 \pm 188 M\Omega$
- $\rho_i = 992 \text{ ohm.cm}$ based on prediction for diffusion of NBD-MTMA inside dendritic spine . R_{neck} ranged from 31 to 412 $M\Omega$ with an average of $128 \pm 93 M\Omega$.

Taking into account a higher resistance of the cytoplasm inside spines, our estimate of spine neck resistance is much higher than previously estimates, approaching 1 $G\Omega$ in some spines.

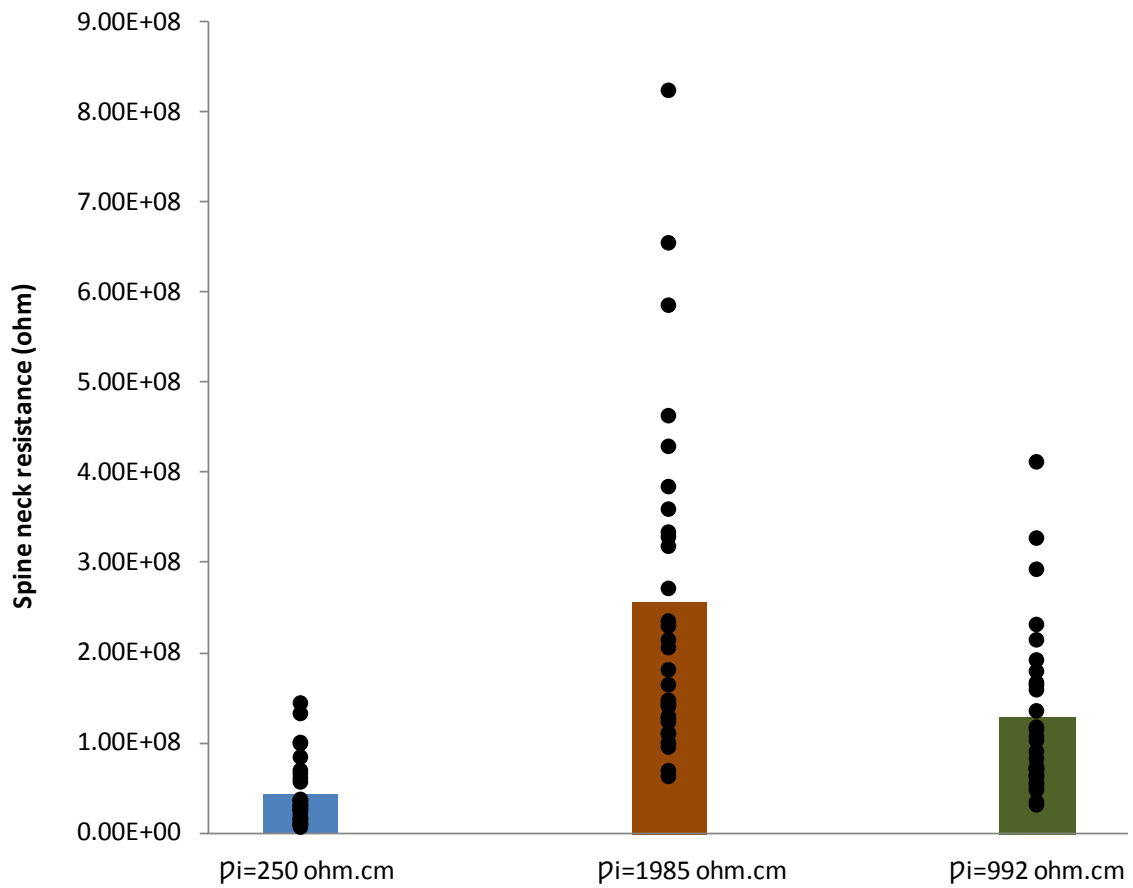


Figure IV-9: Spine neck resistance.

Spine neck resistance was calculated for $\rho_i=250$ ohm.cm, $\rho_i=1985$ ohm.cm, $\rho_i=992$ ohm.cm. Black circles represent individual data points, and bars represent averages.

G. Dendritic spines act as molecular enrichment devices.

We found that the cytoplasmic properties inside a neuron can vary between compartments. The movement of small molecules inside dendritic spines is around 5 times slower than in dendrites. A simple modeling study (data not shown) suggested that such heterogeneity in diffusion speed should result in different particle densities in spines and dendrites at equilibrium. To investigate this possibility, we used our correlative data sets to build synthetic two-photon images with a homogeneous distribution of particles inside (**Figure IV-10. b**). Intensity measurements between synthetic and real two-photon images revealed that dendritic spines are more fluorescent in the two-photon images (**Figure IV-10. c**) compared to the prediction. In our data set (n=2/30 cells/spines), spine intensity ratio between two-photon images and synthetic images ranged from 0.80 to 3.71 with an average of 1.51 ± 0.69 . Dendritic spines are 50% “too bright” in the two-photon images, indicating that the dye concentration is higher in spines than in dendrites. This is consistent with the idea that diffusion is slowed down in spines, and indicates that spines enrich all kinds of molecules by this biophysical mechanism.

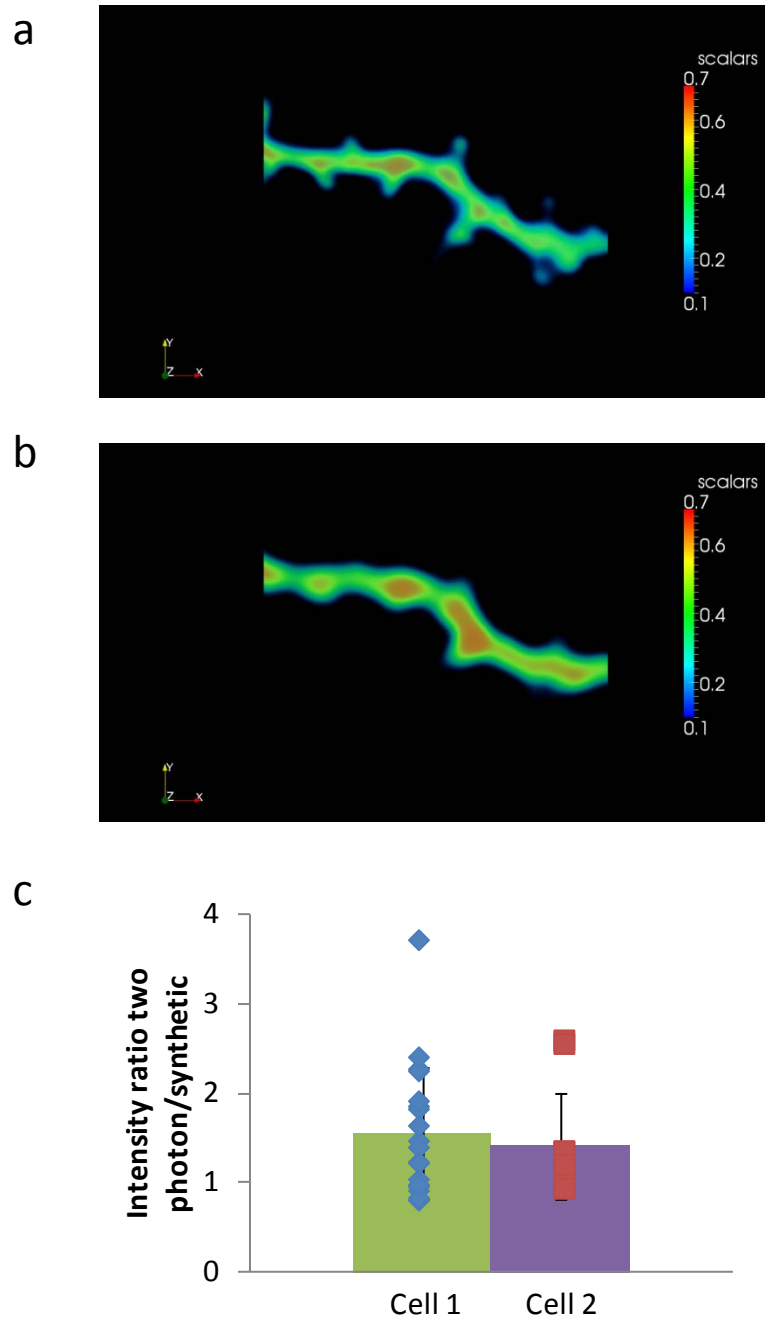


Figure IV-10: Simulated fluorescence images revealed increased concentration of particles inside dendritic spines.

(a) Two-photon volume rendering. (b) Synthetic volume rendering: EM reconstruction convolved by PSF of the microscope assuming a homogeneous distribution of Alexa inside dendrites and spines. (c) intensity ratio measurement between two-photon and synthetic volume rendering.

H. Activity induced change in diffusion.

Very recently it has been discovered that dendritic spine compartmentalization is plastic and can be regulated by neuronal activity. In slice cultures, a study has shown that coincident synaptic activation and postsynaptic action potentials rapidly restrict diffusion across the neck (Bloodgood and Sabatini 2005). A second study has shown in acute slices that strong depolarization of neurons can induce drastic changes in diffusional coupling between spine head and dendrite (Grunditz, Holbro et al. 2008). The mechanism of such a rapid change in dendritic spine diffusional coupling is unknown. It could be a rapid change in dendritic spine morphology or/and change in cytoplasmic properties, e.g. viscosity.

Dendritic spine diffusional coupling is different between acute slice and slice culture (Grunditz, Holbro et al. 2008). In a first step, we verified that rapid changes in diffusional coupling induce by step depolarization also occurs on slice cultures.

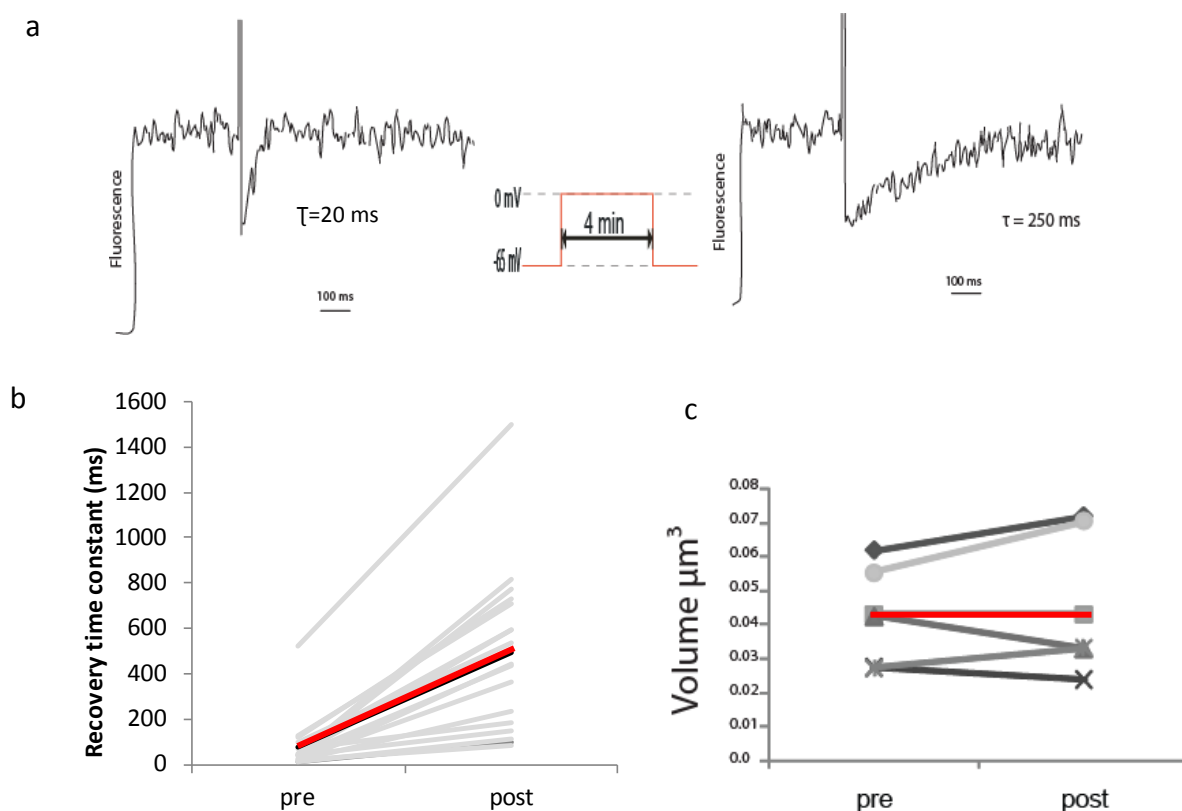


Figure IV-11: Postsynaptic depolarization changes diffusional coupling between spine head and dendrite.

(a) Example of a FRAP experiment in the same spine before and after strong depolarization of the neuron. Line scans across the spine head were used to follow fluorescence recovery. (b) Recovery time constant before and after depolarization in individual spines. Red line represent average. (c) Volume measurements in individual spine before and after depolarization. Red line represents average.

We therefore tested whether a step depolarization to 0 mV, evoked by current injection, would affect diffusional coupling in slice culture. After the end of a 4 min depolarization τ_{equ} (alexa) was increased on average by a factor of 7 (**Figure IV-11.b**). In our data set (n=4/18 cells/spines) τ_{equ} (alexa) before depolarization ranged from 9.5 to 122 ms with an average of 77 ± 119 ms. After depolarization τ_{equ} (alexa) ranged from 99 to 816 ms with an average of 490 ± 362 ms. Spine head volume did not significantly change in our experiments, suggesting that the drastic increase in τ_{equ} (alexa) was due to an increase in the L/A ratio of the spine neck or a change in the cytoplasmic properties inside the spine (**Figure IV-11.c**).

To determine whether cell-wide changes in cytoplasmic viscosity account for the changes in τ_{equ} (alexa), D_{alexa} was measured before (**Figure IV-12.a**) and after step depolarization (**Figure IV-12.b**). In the control D_{alexa} ranged from 120 to 227 $\mu\text{m}^2 \cdot \text{s}^{-1}$ with an average of $173 \pm 41 \mu\text{m}^2 \cdot \text{s}^{-1}$ (n=6). After depolarization D_{alexa} ranged from 27 to 55 $\mu\text{m}^2 \cdot \text{s}^{-1}$ with an average of $38 \pm 10 \mu\text{m}^2 \cdot \text{s}^{-1}$ (n=5) (**Figure IV-12.d**). Apparently, strong depolarization of a neuron changes dramatically the properties of the cytoplasm in the entire cell. This suggests that the changes in τ_{equ} (Alexa) that we and others observed after strong depolarization are probably due to a change in viscosity rather than rapid changes in morphology.

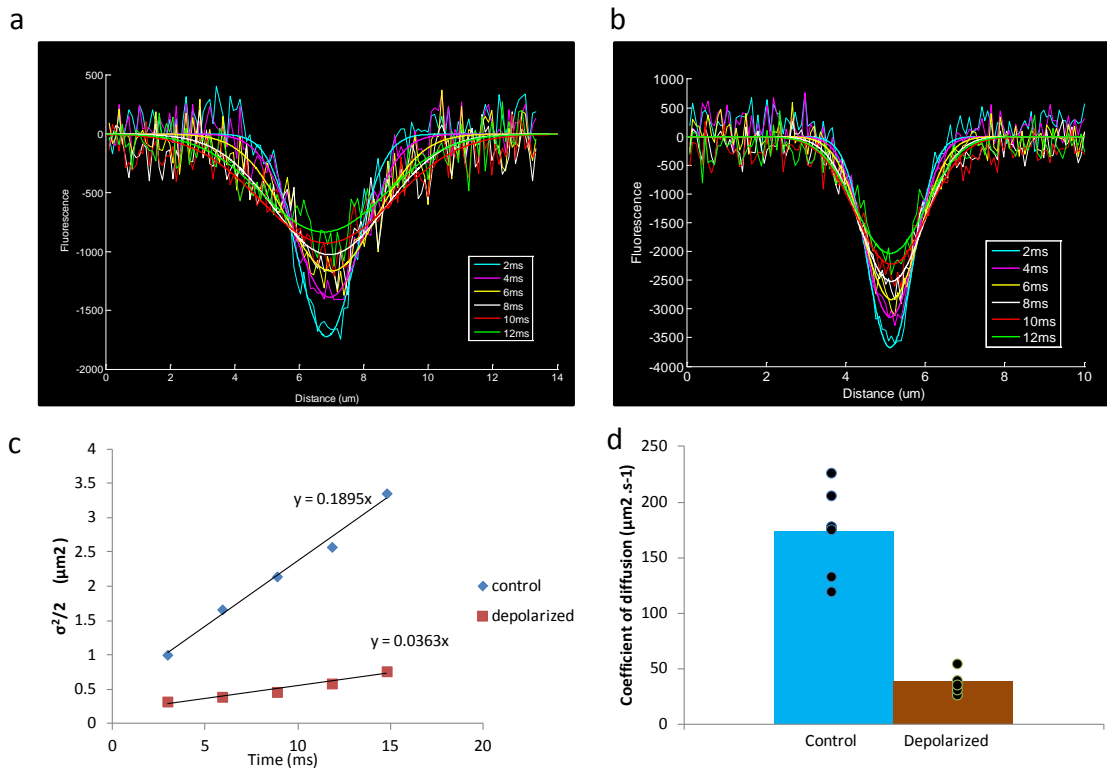


Figure IV-12: D_{alexa} is affected by strong depolarization of the neurons.

(a)(b) Intensity profile along the dendrite at various times after photobleaching (noisy line). Smooth lines are Gaussian fits before (a) and after depolarization (b) of the neuron. (c) $\Delta(\sigma^2/2)$ versus time after photobleaching for a control and a depolarized dendrite. The slope gives the coefficient of diffusion. (d) Coefficients of diffusion for Alexa in control and depolarized neuron. (Average and distribution)

V. Discussion

In this study, we used a correlative approach using EM and two-photon microscopy to investigate diffusional coupling between dendritic spine heads and their parent dendrites. We found that the morphology of dendritic spines predicts the residence time of small molecules. We calculated the coefficient of diffusion of a small fluorophore inside dendritic spines and found that diffusion was slowed down by a factor of 5 compared to the dendritic environment. Compartmentalization of bigger molecules like enzymes could not be predicted from the morphology of spines. We speculate that a size filter exists in some spines, regulating the motility of large molecules differently from spine to spine. Since the movement of small molecules is slowed down in spines, it is highly likely that the resistivity of spine cytoplasm is higher than previously thought, suggesting that spines could act as electrical compartments. A comparison of our two-photon images with synthetic images calculated from our EM reconstructions suggests that particles inside the neuron are not homogeneously distributed but rather concentrated in dendritic spines. We suggest a new function for dendritic spines as molecule enrichment device. Finally, the coefficient of diffusion inside neurons is not a static value, but intense activity can change the viscosity of the entire cytoplasm.

A. Diffusion of molecules is slowed down inside dendritic spines.

Thanks to our correlative approach, we have for the first time a measure of the diffusional coupling between spines and dendrites combined with detailed measurements of spines morphology on the same spines (**Figure IV-2**). We learned from these measurements that:

- The morphology of dendritic spines predicts diffusional coupling with an accuracy of 85% (**Figure IV-6**). Thus, the micro-viscosity of the cytoplasm is near identical in all spines of a given cell. Spine structures are extremely heterogeneous even on a small portion of dendrite (**Figure I-4**). We know now that this heterogeneity will have a direct impact on compartmentalization of small molecules.

- The coefficient of diffusion of small molecules inside dendritic spines is slowed down by a factor of 5 compared to their parent dendrites, indicating a high viscosity of spine cytoplasm.

It was generally assumed that the cytoplasm of spine and dendrite are identical (Harris and Stevens 1989; Svoboda, Tank et al. 1996). Since the spine neck diffusion time constants have been measured previously (Svoboda, Tank et al. 1996; Sabatini, Maravall et al. 2001; Harvey and Svoboda 2007) and dendritic spine morphology was also known, why was it not noted that diffusion in spines is unusually slow? Indeed, calculation of τ_{equ} from morphological data and direct τ_{equ} measurements gave similar values (Yasuda and Murakoshi 2011). But for several reasons, such a comparison led to wrong estimates of D:

- Measurements from different model systems were combined. Most of the measurements of τ_{equ} were made in acute slices whereas EM morphology came from perfusion fixed brains. We know that the average τ_{equ} is very different in acute slices and *in vivo* (Grunditz, Holbro et al. 2008): Median τ_{equ} jumps from 40 ms to 130 ms between acute hippocampal slices and cortical pyramidal cells *in vivo*, leading to error by a factor of 3 in calculation of diffusion coefficient inside dendritic spine.
- Dendritic spine morphology is extremely heterogeneous even on the same dendrite (**Table 1**)(Harris and Stevens 1989; Arellano, Benavides-Piccione et al. 2007). Since there are no correlations between spine morphological variables, there is no ‘typical spine’ (Harris and Stevens 1989; Arellano, Benavides-Piccione et al. 2007). τ_{equ} is also extremely variable between spines, spanning two orders of magnitude (Svoboda, Tank et al. 1996)(**Figure IV-1**). It is in consequence very hazardous to estimate the coefficient of diffusion of molecules from an average spine. It is necessary to know the morphology of individual spines and the associated τ_{equ} .

A restriction of small molecule mobility in neuron has also been described in cerebellar stellate cells (Soler-Llavina and Sabatini 2006). These neurons are capable of input-specific synaptic plasticity even without dendritic spines by compartmentalizing the diffusion of Ca^{2+} due to interaction with calcium buffers and general restriction of small molecule mobility in the entire dendrite by a factor of 10 compared to the cytoplasm of

hippocampal pyramidal neurons (Svoboda, Tank et al. 1996; Soler-Llavina and Sabatini 2006). In spiny neurons, dendritic spines have apparently trapped this “viscous cytoplasm”, leaving dendritic viscosity relatively low. The mechanism slowing down small molecule diffusion is unknown, but might result from molecular crowding or high tortuosity of the dendroplasm (Kushmerick and Podolsky 1969; Popov and Poo 1992; Ellis 2001; Soler-Llavina and Sabatini 2006) and is expected to retard the movement of all molecules, including second messengers and proteins.

To check if the numbers and signs of charges carried by molecules affect their diffusion inside spines we used the small, positively charged fluorophore NBD-MTMA. This fluorophore behaved similarly to alexa (**Figure IV-7**), but diffusion was faster. Unfortunately, we could not measure the diffusion of NBD-MTMA in the dendrite, as we approached the time resolution of our microscope and NBD-MTMA was difficult to bleach with two-photon excitation. Therefore, at this point, we cannot decide whether the smaller Stokes radius or the different charge of NBD-MTMA was responsible for its faster diffusion.

During our FRAP experiments, the entire spine and part of its neck were bleached. Thus, our measurements of D_{alexa} represent an average for the entire spine. It is possible that the diffusion of Alexa is different between the spine head and the spine neck. An ongoing study at the computer science department of Basel University (C. Blumer, T. Vetter) uses the correlative datasets produced in this thesis to model the diffusion of particles in 3D, with the goal to determine the speed of diffusion inside the spine neck and the spine head.

B. The controversy about spine neck resistance.

It is highly debated whether spines can be considered electrical compartments. A critical parameter determining the potential for electrical compartmentalization is the resistance of the spine neck (Koch and Poggio 1983). Studies investigating the morphology of dendritic spines with electron microscopic reconstructions of spine geometries or

indirectly by measuring the diffusional coupling through spine necks concluded that most spine neck are not thin and long enough (spine neck resistances are too small) to significantly modulate synaptic currents (Harris and Stevens 1989; Svoboda, Tank et al. 1996). Estimation ranged from 4 to 50 M Ω . However, an increasing number of recent studies using calcium and voltage imaging to investigate synaptic physiology of synapses located on dendritic spines concluded that the spine neck must affect the electrical signal (Araya, Jiang et al. 2006; Grunditz, Holbro et al. 2008; Bloodgood, Giessel et al. 2009; Palmer and Stuart 2009). Why is there such a discrepancy between studies investigating dendritic spines properties and those investigating synaptic physiology? In their calculation of spine neck resistance, morphological studies assumed that the cytoplasm inside dendritic spines is identical to dendrites. We know now that this is not the case, and we estimate spine neck resistance to be as high as 1 G Ω in some spines (**Figure IV-9**). Stimulation of synapses located on spines with such a high neck resistance would result in a very large voltage difference between spine head and dendrite (Segev and Rall 1988; Grunditz, Holbro et al. 2008).

C. Dendritic spines possess a size filter.

The general slowing down in diffusion inside dendritic spines also affects PA-GFP and 70 kDa dextran, but an additional filter seems to exist in a subset of spines to retain them longer in the spine head (**Figure IV-8**). A study shown that the diffusional coupling of PA-GFP in individual spine can spontaneously change within minutes in slice cultures and can be shifted toward higher values by chronic activity (Bloodgood and Sabatini 2005), thus the ability to retain large molecules could reflect the history of a particular spine. Such a filter could be created by a mesh of actin. It is known that dendritic spine heads are full of actin filaments (Fischer, Kaech et al. 1998). One could test this hypothesis by depolarizing actin and to see if the correlation between $\tau_{\text{equ}}(\text{alexa})$ and $\tau_{\text{equ}}(\text{PA-GFP})$ improves.

Second messengers and many proteins involved in spines and synapses regulation are similar in size to PA-GFP (28 kDa) or bigger. Synaptic plasticity is typically induced by repetitive stimulation (Bliss and Lomo 1973) of synapses, lead to the activation of second messenger cascades. The ability to retain more or less these messengers could influence the threshold for the induction of synaptic plasticity. Dendritic spines which retain large

molecules could be primed for plasticity. Using glutamate uncaging, one could investigate if the retention of big molecules inversely correlates with the strength of the protocol needed to induce plasticity.

D. Dendritic spines concentrate particles.

Although it was always assumed that spines and dendrites distribute dye evenly (Svoboda 2004), the heterogeneity in diffusion speed between spines and dendrites affects particle distribution (**Figure IV.10**). This new function of dendritic spines could have implications from a technical and biological point of view.

- In fluorescence microscopy, the measurement of spine volumes assumes a homogeneous distribution of fluorophores. Since spines concentrate particles, dendritic spines appears brighter (and, in consequence, bigger) than their real size. Microscopists will have to take this enrichment into account when analyzing spine size.
- Dendritic spines represent a very small volume compare to the entire dendritic tree (data not shown). Concentrating proteins inside the spines would decrease the quantity of these proteins that the neuron has to produce to reach the desired concentration inside the spine head since there is no need to fill the entire dendritic tree.

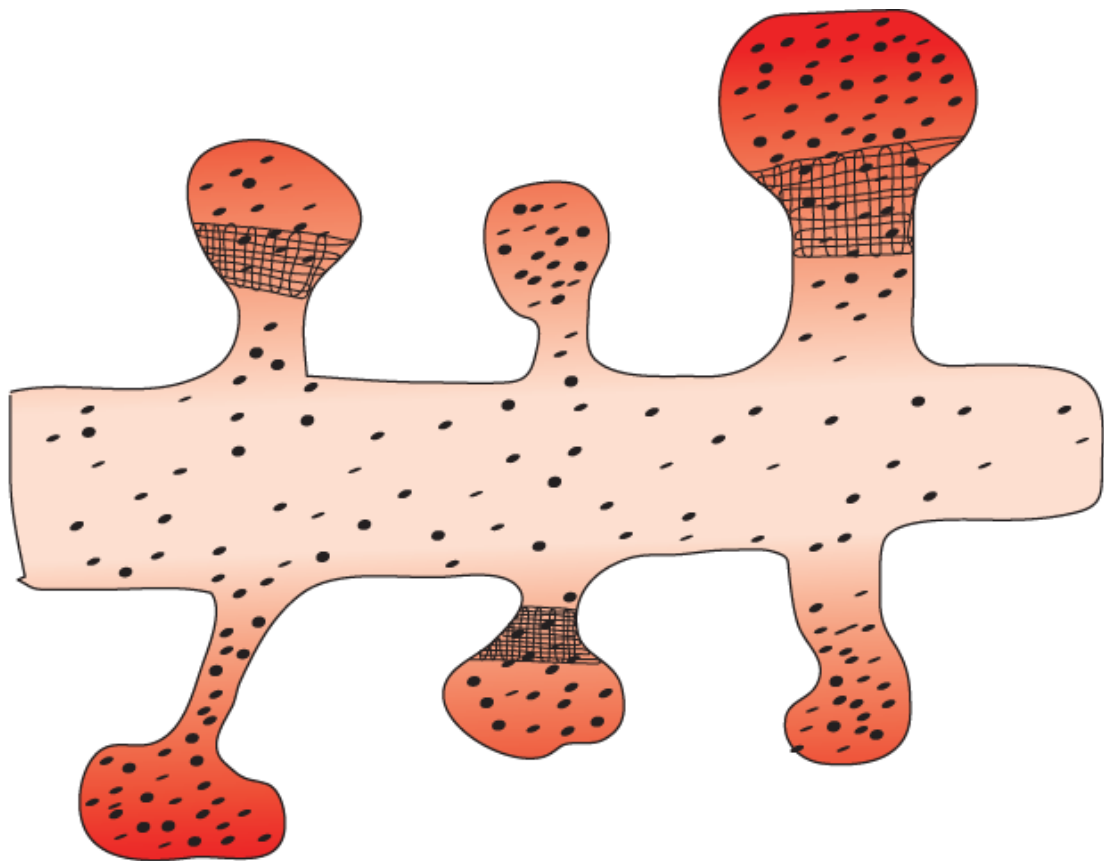
E. Activity induced changes in diffusion speed.

Recently it has been discovered that diffusional coupling can be changed by activity, at the level of a single spine by pairing synaptic stimulation and bAPs (Bloodgood and Sabatini 2005), or in all spines with a strong depolarization of the postsynaptic neuron (Grunditz, Holbro et al. 2008). Since diffusional changes was not accompanied by changes in spine head volume, it was thought that strong activity could change the morphology of the spine neck. We know now that strong depolarization of the postsynaptic neuron changes the coefficient of diffusion in the entire dendrite (**Figure III.11**). The electrical resistivity of the cytoplasm will increase at the same time, providing electrical and chemical compartmentalization. Increased electrical compartmentalization would lead to activation

of voltage dependent channels boosting spine depolarization, and consequently increase calcium influx into the spine. The amplitude of calcium signals has been shown to be correlated with the magnitude of change in synaptic strength (Nevian and Sakmann, 2006). Increased spine neck resistance could therefore drastically facilitate or even be a prerequisite for the induction of LTP.

This thesis was started with the goal to distinguish between activity-dependent changes in spine morphology and activity-dependent changes of cytoplasmic properties. The strong differences in cytoplasmic properties between spines and dendrites at baseline (before stimulation) came as an unexpected surprise. In addition, we could clearly show that depolarization does change cytoplasmic properties. In the future, it would be very interesting to perform correlative experiments on stimulated cells to address the question whether the outside shape of spines does change in response to strong activity. The fact that only one time point can be morphologically reconstructed is of course a severe limitation of electron microscopy and makes it impossible to do 'before/after' measurements of individual spines. Very likely, super-resolution light microscopy (e.g. STED) will eventually be applied to visualize changes in spine morphology during activity at nanometer resolution. From the point of view of the synapse, it might not even matter whether active second messengers are retained due to a constricted spine neck diameter or due to a high viscosity plug in the neck. How exactly biochemical reactions inside the spine are affected by altered mobility of the reactants we don't know yet, but in this thesis it became clear that the postsynaptic milieu is physically very different from the cuvette of the biochemist, and even from the rest of the neuron.

In conclusion dendritic spines appear to be even more complex than previously thought, as we found a new function and a new level of regulation in their functionality. By integrating informations from diffusion and ultrastructure measurements on the same dendritic spines we have gained new insights on the regulation of compartmentalization in spines. These insights could help to resolve contradiction in previous studies and also supplement the model of dendritic spine functionality (**Figure V-1**).



• Molecules

Viscosity
- +

Size filter

- Figure V-1: New model of dendritic spine compartmentalization.**
- The diffusion of molecules is slowed down inside dendritic spines.
 - A subset of spines possess a size filter.
 - Dendritic spines concentrate particles.

VI. Annexe

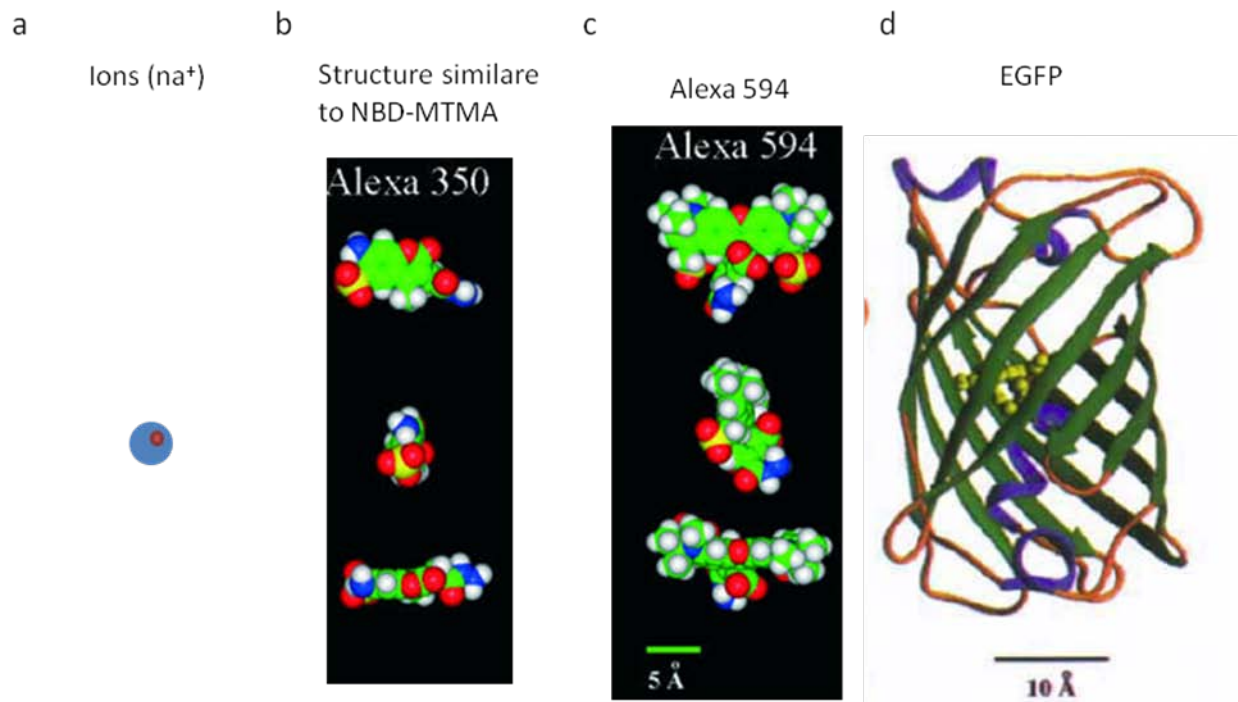


Figure VI-1: Scale of an ion and different fluorophores.

(a) An atom of sodium is represented (red ball) surrounded by its hydration sphere. (b) (c) structure Alexa series. Space-filling models showing each axial face (separated by 90 degrees rotations), Atoms are represented by color: Carbon(green), hydrogen(white), nitrogen (blue), oxygen (red), and sulfur (yellow)(Nitsche, Chang et al. 2004). (d)The overall shape of GFP where β -sheet (green) and α -helices can be visualized(Yang, Moss et al. 1996).

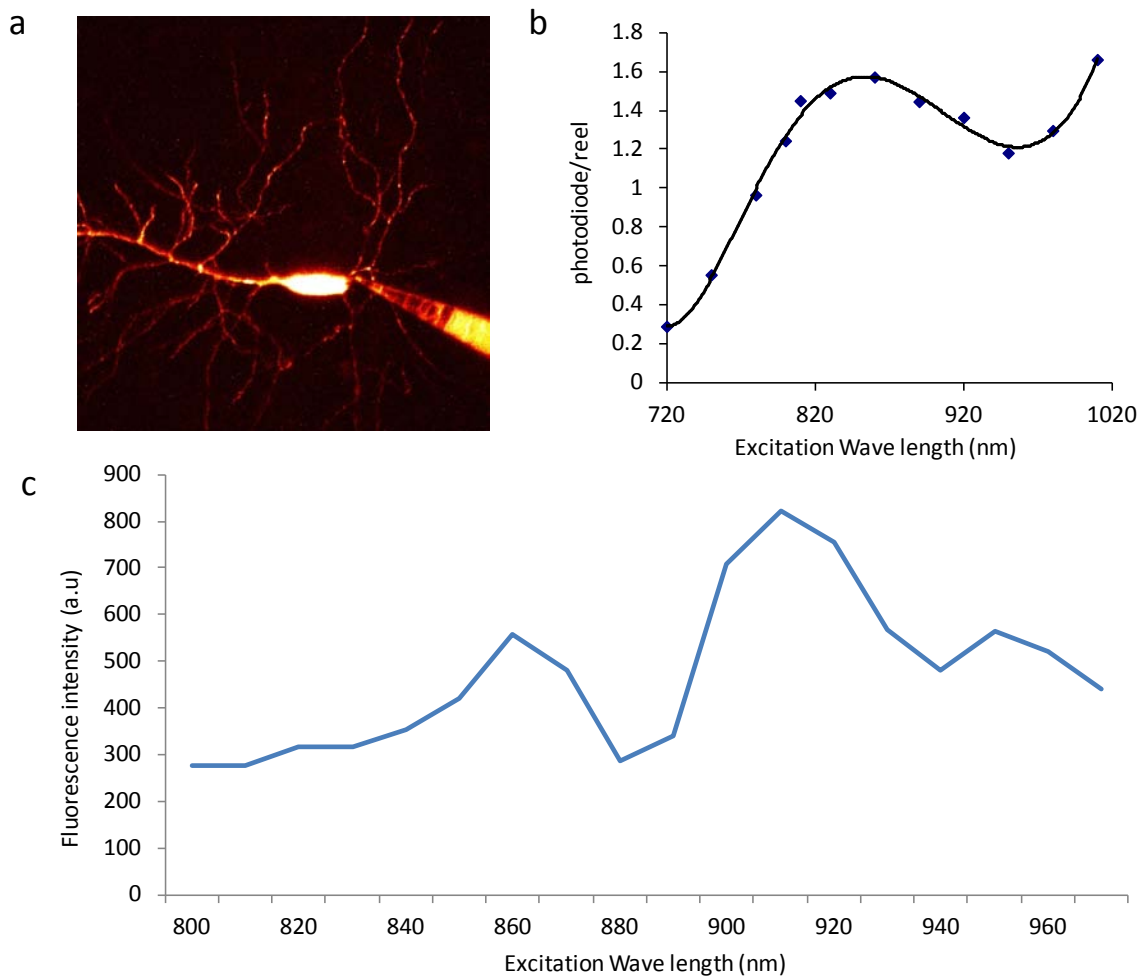


Figure VI-2: Two-photon excitation spectrum of NDB-MTMA.

(a) Max projection of a CA1 neuron filled with NBD-MTMA through a patch pipette. (b) Graphic representing the ratio of the laser power measured with photodiode and real power measured in the back focal plane versus the excitation Wavelength. (c) Graphic representing the fluorescence excitation spectra for NBD-MTMA.

Fluorescence Image Segmentation by using Digitally Reconstructed Fluorescence Images

Clemens Blumer¹, Cyprien Vivien², Thomas G. Oertner², Thomas Vetter¹

¹Department of Mathematics and Computer Science, University of Basel, Switzerland
{clemens.blumer, thomas.vetter}@unibas.ch

²Friedrich Miescher Institute for Biomedical Research, Basel, Switzerland
{cyprien.vivien, thomas.oertner}@fmi.ch

Abstract— In biological experiments fluorescence imaging is used to image living and stimulated neurons. But the analysis of fluorescence images is a difficult task. It is not possible to conclude the shape of an object from fluorescence images alone. Therefore, it is not feasible to get good manual segmented nor ground truth data from fluorescence images. Supervised learning approaches are not possible without training data. To overcome this issues we propose to synthesize fluorescence images and call them 'Digitally Reconstructed Fluorescence Images' (DRFI). We propose how DRFIs are computed with data from 'Serial Block-Face Scanning Electron Microscopy' (SBFS-EM). As novelty, we use DRFIs to learn a distribution model of dendrite intensities and apply it to classify pixels into spine and non-spine pixels. By using DRFIs as test data we also have the ground truth of spine and non-spine pixels and can validate the results. With DRFIs supervised learning of fluorescence images is feasible.

images are highly anisotropically blurred. Therefore, the use of classical 3D image analysis is not feasible. Even for experienced biologists it is very challenging to segment objects or structures in fluorescence images. Fluorescence images are difficult to be analyzed automatically. The evaluation of results is very ambitious because there does not exist real ground truth data. Automated image analysis using supervised learning requires training data. In the domain of fluorescence images the generation of training data is very difficult. In contrast, the manual reconstruction of specially prepared, fixed dendrites in electron microscopy (EM) images is possible. These reconstructions have the correct geometrical properties of the dendrites. It is feasible to (manually) identify different structures (e.g. spines) in the reconstructions. This motivates to compute training data from EM reconstructions.

I. INTRODUCTION

In the biological field the bottleneck moved from data generation to data analysis. Neurobiologists heavily use microscopy to investigate how neurons communicate. Thanks to fluorescence imaging (neurons are filled with fluorescent dyes as a volume marker) it becomes possible to image live cells over time with a high resolution resolving dendrites and spines (Fig. 1 shows schematic neurons).

Fluorescence images are intensity images. In the sample, proteins are excited and emit photons that are counted. No optical mapping of an object to its fluorescence image exists (this means, there is no direct reflection of light). The emission and the point spread function (PSF) of e.g. 2-photon imaging is large and blurry. The resulting images lack of edges respectively surfaces. It is not possible to conclude the object shape from the fluorescence image. 3D fluorescence

In our approach we combine 2-photon imaging and electron microscopy and transfer a-priori knowledge from EM reconstructions to the 2-photon imaging modality. The conjunction of the two modalities is realized by computing synthetic fluorescence images that we call 'Digitally Reconstructed Fluorescence Images' (DRFI). This enables automated fluorescence image analysis algorithms based on supervised learning.

Furthermore, EM reconstructions and DRFIs provide the possibility to study dendrites and its fluorescence images in different aspects. It is possible to visualize the effect of enclosed structures (e.g. mitochondria) on imaging and how different spines are represented in fluorescence images. Therefore, beside the computation of the statistical variability of the fluorescence response also different (biologically inspired) questions can be studied.

In our studies we focus on the classification into spine and non-spine voxels in fluorescence images. Different approaches exist but none of them uses supervised learning. Many approaches are based on the use of a full skeleton or backbone ([1], [2], [3], [4], [5]) or use the skeleton represented in a different way, e.g. Zhang et al. [6] use vector flows. Shi et al. [7] use the center line to compute a surface. Other approaches like Rodriguez et al. [8] use local threshold methods. We propose a novel approach and model fluorescence intensity of dendrites. Therefore, we propose how a statistical model for fluorescence images can be computed and overcomes the drawbacks of fluorescence images. In the application we model dendrites and segmentations by using Principal Component Analysis (PCA).

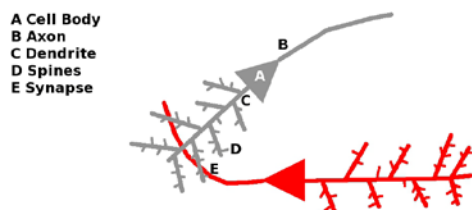


Fig. 1. Signals are sent from cell to cell over axons (B) to dendrites (C). The connection between axons and dendrite is often located at spines (D) and is called synapse (E).

Section II introduces the raw data generation. In section III we describe how DRFIs are computed. In section IV we explain the knowledge transfer, a 2D model and its application and in section V we discuss our approach.

II. RAW DATA GENERATION

We image neurons and are interested in dendrites and spines. Dendrites have the size of some μm . We can image with high magnification such that fine structures like spines are visible.

Many spines are visible by 2-photon imaging but it is difficult to conclude the geometrical shape from fluorescence images. Therefore, we use electron microscopy and DRFIs.

Since years electron microscopy is used to image small structures like spines in high resolution. Classical electron microscopes like Transmission Electron Microscopy have the disadvantage that the image stack must be aligned and corrected for distortion. In 2004 Denk and Horstmann [9] presented the 'Serial Block-Face Scanning Electron Microscopy' (SBFS-EM). The data does not require an alignment. Image analysis can be done without preprocessing. By the preparation the tissue and neurons are fixed (not possible to do time-lapse imaging). The samples get trimmed to a few hundred μm and are then ready for imaging (for more details about preparations and SBFS-EM in general see [9]).

We imaged with 2-photon imaging and SBFS-EM the same piece of dendrite. This enables us to visually compare the DRFIs with imaged fluorescence images. By a special preparation one cell becomes distinguishable (labeled) from background in SBFS-EM. Then we can easily reconstruct the dendrite of interest (see III-A).

III. DIGITALLY RECONSTRUCTED FLUORESCENCE IMAGES (DRFI)

Our data set resolves fine structures like spines in all details in the SBFS-EM modality. But live neurons can only be imaged with fluorescence imaging. It is time consuming and not trivial to acquire both data sets from the same piece of dendrite. We would like to analyze only fluorescence images. Therefore, the knowledge about structures and segmentations must be transferred from the SBFS-EM to the 2-photon imaging modality. We use synthetic fluorescence images to transfer a-priori knowledge.

The goal of the DRFI approach is to model information in the 2-photon imaging modality that is very difficult to detect in fluorescence images directly but easily in SBFS-EM data (like e.g. spines and its segmentation).

A. Manual Dendrite Reconstruction in SBFS-EM

Data from the SBFS-EM is used without any previous alignment nor distortion correction. An experienced biologist manually thresholds the data to a binary image. The largest connected object is kept and all others (background noise) are removed. This first reconstruction has enclosed structures which can be divided into artifacts and mitochondria. The artifacts are regions where the labeling failed (in Fig. 2 D an artifact is highlighted with an "X"). The special labeling does not stain mitochondria. To correct the enclosed structures

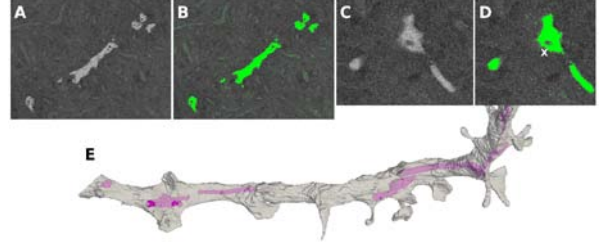


Fig. 2. A,C) Two examples of raw data of SBFS-EM. B,D) Examples with overlaid segmentation (an enclosed structure is at "X"). E) 3D EM reconstruction with visualized mitochondria (pink).

all of them are filled and mitochondria volumes are subtracted from the reconstruction. This yields to correct reconstructions of dendrites which exclude mitochondria. This is important because in 2-photon imaging mitochondria is not fluorescent. Fig. 2 shows the raw data and the reconstruction of the dendrite with visualized mitochondria (E).

B. Point Spread Function of Fluorescence Images

The response of an imaging system to a point source is called point spread function (PSF). In many imaging systems the spatial extension of the PSF is negligible. But not in 2-photon imaging and similar microscopes. These imaging systems have a large PSF. Furthermore, the PSF is elongated along the optical axis (laser- or z-direction). The PSF can be measured or synthetically approximated. We use a synthetic PSF. This enables us to compute new data (and so new models) for any possible microscope configuration.

Zhang et al. [10] show that a 3D Gaussian distribution approximates the PSF quite accurate:

$$\text{PSF}(x, y, z) = g_{\sigma_p, \sigma_z}(x, y, z) = \exp\left(-\frac{x^2 + y^2}{2\sigma_p^2} - \frac{z^2}{2\sigma_z^2}\right) \quad (1)$$

where σ_p is the standard deviation in x,y-direction (plane), σ_z in z-direction and x, y, z is the position relative to the center of the PSF.

Furthermore, Zipfel et al. [11] show a dependency between the $1/e$ width ω_p and ω_z . It is valid that

$$\sigma = \frac{\text{FWHM}}{2\sqrt{2\ln 2}} = \frac{2\sqrt{\ln 2}\omega}{2\sqrt{2\ln 2}} = \frac{\omega}{\sqrt{2}} \quad (2)$$

Where FWHM is the full width at half maximum. Therefore, we get for the standard deviations

$$\sigma_p = \begin{cases} \frac{0.320\lambda}{2\text{NA}} & \text{if } \text{NA} \leq 0.7 \\ \frac{0.325\lambda}{2\text{NA}^{0.91}} & \text{else} \end{cases} \quad (3)$$

And

$$\sigma_z = \frac{0.532\lambda}{2(n - \sqrt{n^2 - \text{NA}^2})} \quad (4)$$

where NA is the numerical aperture, n is the refraction index and λ is the wave length of the laser. The constants are given by Zipfel et al. [11].

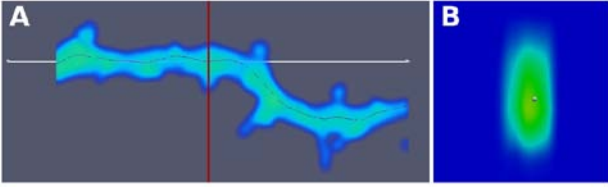


Fig. 3. A) Volume rendering of DRFI with overlaid backbone, visualized backbone-orthogonal plane (red line) and normal of the plane (arrow). B) Backbone-orthogonal slice extracted from DRFI.

C. Computing Digitally Reconstructed Fluorescence Images
The EM reconstruction is the correct geometrical shape of the objects (dendrites). We assume a homogeneous filled neuron and exclude mitochondria volume. Given the synthetic PSF it is known how every object point is mapped to the 2-photon imaging modality. A convolution of the shape with the PSF gives the DRFI

$$F_d(i, j, k) = R_d(i, j, k) * \text{PSF}_{\text{NA}, \lambda, n}(x, y, z) \quad (5)$$

where $R_d(i, j, k)$ is the binary image of the reconstruction. Both images must be sampled at the same rate. This is achieved by resampling or computing the PSF with the required sampling frequency.

IV. APPLICATION

In the application we use the computed data to build a PCA model to classify pixels into spine or non-spine. To simplify the classification the model is trained on 2D data extracted from the 3D images.

Dendrites can be illustrated with central curves, also known as backbone. This backbone is the elongation of the dendrite in space. We use 2D images orthogonal to the (manually generated) backbone (see Fig. 3).

Finally, for any 2D backbone-orthogonal slice image a prediction of spines can be done. As a-priori knowledge we use DRFIs of dendrites and spine segmentations which are computed like presented in section III. We use DRFI test data. This enables us to validate the results on pixel level. Therefore, the advantages and disadvantages of our approach can be studied in all details. Also some first 2-photon imaging data is analyzed.

Fig. 4 shows the process pipeline. Offline, the training data is computed from the reconstructions and a synthetic PSF in 3D. From the training data then also offline the PCA models are computed. In the testing phase online the 3D fluorescence image (every backbone-orthogonal slice) is approximated with the dendrite model and from this the approximation for the spine probability model is computed. With the parameters for the spine probability model a segmentation of spines in the 3D space is computed. In the following sections the computation and combination of the 2D models is introduced and detailed results for synthetic 3D test data in backbone-orthogonal slices presented. Furthermore, we show some first results on a 3D fluorescence image from 2-photon microscopy where the prediction results are transferred from the backbone-orthogonal slices to the 3D space.

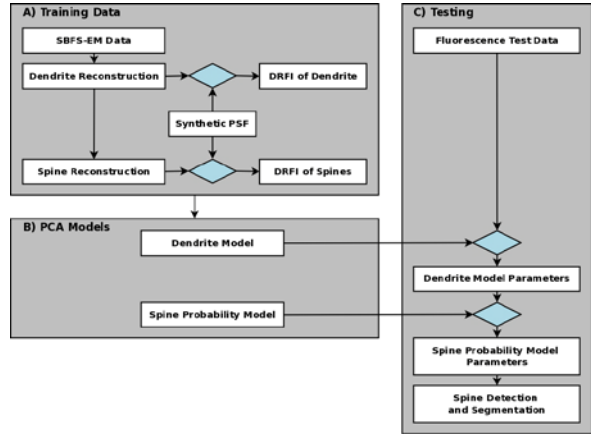


Fig. 4. A) Offline computation of training data. B) Offline Computation of the PCA models. C) Testing Pipeline: For test data the parameters of the dendrite model are computed. Then the parameters for the spine probability model are estimated. Using these parameters the spines are detected and segmented.

A. Transfer of a-priori Knowledge

In EM reconstructions spines and other structures are detectable. The goal of the knowledge transfer is to transfer this information to fluorescence images. Given an EM reconstruction $R_d(i, j, k)$ of the dendrite (including spines) and a manual segmentation $R_s(i, j, k)$ of its spines we can compute the DRFI $F_d(i, j, k)$ of the dendrite including spines reconstruction and a fluorescence image $F_s(i, j, k)$ of the spine segmentation. Because both images are computed with the same PSF the probability for every pixel the intensity is from spine is given by:

$$P_s(i, j, k) = \begin{cases} F_s(i, j, k) / F_d(i, j, k) & \text{if } F_d(i, j, k) > 0 \\ 0 & \text{else} \end{cases} \quad (6)$$

This probability map corresponds to a segmentation in fluorescence images and is the knowledge transfer. It is to mention that there is a smooth transition between spine and dendrite pixels. Therefore, for a final segmentation in fluorescence images a threshold (e.g. > 50% of intensity from spine) must be applied.

B. PCA Model Computation

From DRFI F_d and the probability image P_s backbone-orthogonal slices $F_{d,i}$ and $P_{s,i}$ with $i = \{1, 2, \dots, n\}$ are extracted. The slices are scaled. The scaling is per axis (x/y- and z-axis) to compensate the elongated PSF. The intensity is normalized to $\{0, 1\}$. Then we compute a dendrite model $\text{PCA}(F_{d,i})$ and a spine probability model $\text{PCA}(P_{s,i})$. The computation for both PCA models is the same and we present it for $\text{PCA}(F_{d,i})$.

First we compute the mean of all n examples as

$$\mu_d = \frac{1}{n} \sum_{i=1}^n F_{d,i} \quad (7)$$

and construct the mean-free data matrix:

$$X_d = [F_{d,1} - \mu_d \dots F_{d,n} - \mu_d] \quad (8)$$

Then we do a singular value decomposition of matrix X_d :

$$X_d = U_d D_d V_d^T \quad (9)$$

An arbitrary slice s_d can be written as

$$s_d = \mu_d + U_d \alpha_d \quad (10)$$

where α_d are the PCA-coefficients.

C. PCA Model Combination and Prediction

The goal of model combination and prediction is to approximate a test slice by the PCA-coefficients of the dendrite model and compute the PCA-coefficients of the spine probability model. This yields the prediction maps $s_{s,j}$.

The dendrite model and the spine probability model are constructed of the same slices. Furthermore, any linear combination of principal components u_k can be expressed as linear combination of the example data and vice versa. We assume that a slice of dendrite respectively spine probabilities can be represented by the same linear combination of examples of dendrite slices respectively spine probability maps. Given the assumption it becomes possible to predict the PCA-coefficients of one model by the other one. First we right-multiply eq. (9) with $V_d D_d^{-1}$:

$$X_d V_d D_d^{-1} = U_d \quad (11)$$

$\alpha_d = (\alpha_{d,1}, \dots, \alpha_{d,\bar{n}})^T$ and $\beta_d = (\beta_{d,1}, \dots, \beta_{d,\bar{n}})^T$ are coefficient vectors. Then

$$\sum_{i=1}^{\bar{n}} \alpha_{d,i} u_{d,i} = U_d \alpha_d = X_d V_d D_d^{-1} \alpha_d = X_d \beta_d = \sum_{i=1}^{\bar{n}} \beta_{d,i} x_{d,i} \quad (12)$$

and we have the relations

$$\beta_d = V_d D_d^{-1} \alpha_d \quad (13)$$

and

$$\alpha_d = D_d V_d^T \beta_d \quad (14)$$

Given the assumption above introduced about same linear combinations of examples it is valid that $\beta_s = \beta_d$ and we get

$$\alpha_s = D_s V_s^T V_d D_d^{-1} \alpha_d \quad (15)$$

The prediction map s_s for a 2D dendrite image s_d is given by projecting s_d to the dendrite PCA model using

$$\alpha_d = U_d^T (s_d - \mu_d) \quad (16)$$

and retrieve α_s with eq. (15). Finally, the prediction is:

$$s_s = \mu_s + U_s \alpha_s \quad (17)$$

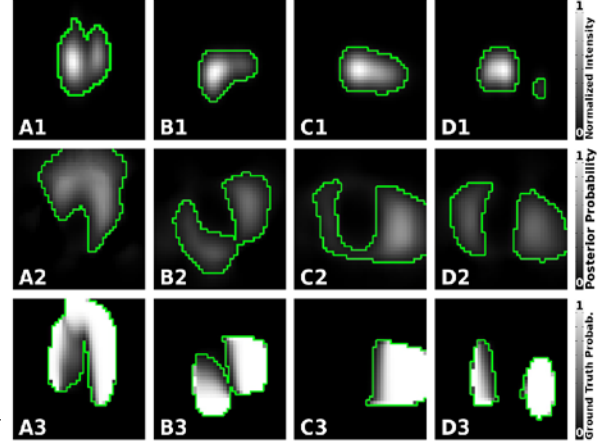


Fig. 5. The first row shows examples of DRFI test slices ($F_{d,i}$) and the second row shows the corresponding prediction maps ($s_{s,i}$). The third row shows the ground truth probability maps ($P_{s,i}$). The outlines (green, 10% of intensity) are marked for better visibility.

D. Results

We used different EM reconstructions for training and testing. First, we present results of synthetic data. This enables us to validate the results with ground truth data. As training data we used an EM reconstruction with 17 spines. The dendrite was rotated along its main axis in 10° steps to compute spines at different orientation relative to the optical axis. Then every $0.02\mu\text{m}$ backbone-orthogonal slices (about 20000) with a side length of $4\mu\text{m}$ were extracted. The slices were resampled at $0.1\mu\text{m}$. From these 20000 slices the PCA model was computed and the first 25 components kept.

Fig. 5 shows results for the test image. From the DRFI of the test dendrite backbone-orthogonal slices $F_{d,i}$ (first row) were extracted and the posterior probabilities $s_{s,i}$ computed (second row, third row shows ground truth probability maps $P_{s,i}$). The posterior probabilities have similar local maxima like the computed ground truth data. With further processing of these posterior probabilities it is possible to conclude from fluorescence images the existence and location of spines and its segmentations.

Furthermore, we computed a binary segmentation of the slices. For the ground truth data we used a threshold of 0.5.

all slices as $0.5 * \sum_{i=1}^{\bar{n}} \text{iosmax}(s_{s,i}) \approx 0.23$. This parameter can be tuned. Fig. 6 shows the slices (same examples like in Fig.

5). The binary results for our predictions are shown in the first row. The second row shows the binary result for the ground truth data. The third row shows a classification into correct background (dark gray), correct foreground (white), missed foreground (light gray) and incorrectly as spine classified (black) pixels.

In the 544 test slices 92.4% pixels are correctly classified (88.2% background and 4.2% foreground pixels). 4.4% are wrongly classified as spine pixels and 3.2% are missed foreground pixels. Changing the threshold value and further changes improve the results.

Furthermore, the approach was tested with the same piece of

T

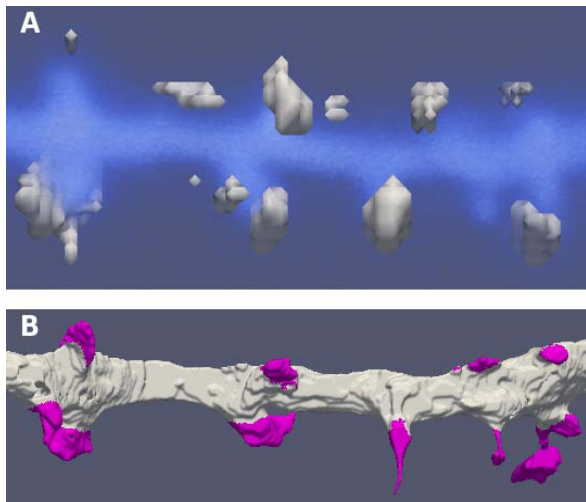


Fig. 7. A) Volume rendering of the fluorescence image and the surface reconstruction of the segmentation. B) Manual aligned reconstruction of the SBFS-EM data with highlighted spines (pink).

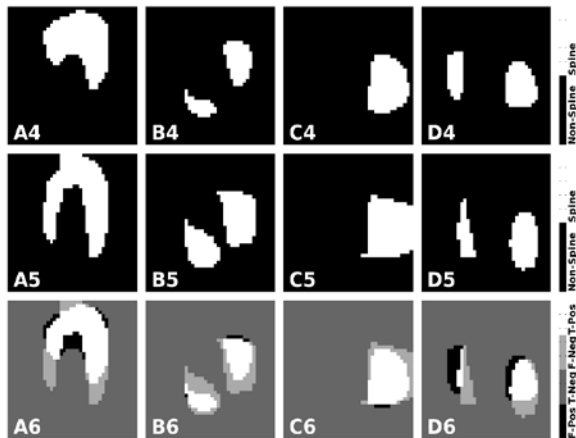


Fig. 6. Binarized results of prediction maps $s_{s,i}$ (first row) and of ground truth data $P_{s,i}$ (second row). The third row shows a comparison between correct (dark gray and white) and wrong (light gray and black) classified pixels.

dendrite like in the synthetic case but imaged with 2-photon microscopy. The backbone was approximated automatically (using a thinning algorithm) and 2D slices extracted. Then the model was applied to generate a prediction for these 2D images. The predictions of the 2D images were transformed back to the 3D space and then binarized with a manually selected threshold $t = 0.35$. Fig. 7 shows the results. The first row shows a volume rendering of the fluorescence image and in grey a surface reconstruction of the segmentation. The second row shows for the same piece of dendrite the reconstruction of the SBFS-EM data (spines are highlighted in pink). This direct comparison of the segmentation with the geometrically correct reconstruction is possible because of the correlative data set. The use of the same piece of dendrite in the synthetic and the real case shows that the approach can be transferred from synthetic data to real fluorescence images. The application to real fluorescence data shows the power of

the supervised learning approach trained with synthetic data.

V. CONCLUSION

We presented a novel approach to compute 2D models for fluorescence data that uses a-priori knowledge from electron microscopy reconstructions. The information transfer from reconstructions to fluorescence images and the combined models enabled us to classify pixels of 2D slices orthogonal to the backbone into spine or non-spine.

The synthetic and real fluorescence examples illustrated how to model the distribution of fluorescence intensity from dendrites and spine probabilities in 2D thanks to DRFIs. Enough training data can easily be computed in 2D.

The process pipeline is working with real fluorescence images. Furthermore, by the use of a correlative data set it became possible to compare the results with the geometrical correct reconstruction of dendrite and spines. This showed also

that the approach gives similar predictions for synthetic data and real fluorescence images.

ACKNOWLEDGMENTS

This work was supported by an IPHD grant of the SystemsX.ch initiative evaluated by the Swiss National Science Foundation.

REFERENCES

- [1] Jie Cheng, Xiaobo Zhou, Eric Miller, Rochelle M. Witt, Jinmin Zhu, Bernardo L. Sabatini, and Steven T.C. Wong, "A novel computational approach for automatic dendrite spines detection in two-photon laser scan microscopy," *J. Neurosci. Methods*, vol. 165, no. 1, pp. 122-134, 2007.
- [2] Firdaus Janoos, Kishore Mosaliganti, Xiaoyin Xu, Raghu Machiraju, Kun Huang, and Stephen T.C. Wong, "Robust 3d reconstruction and identification of dendritic spines from optical microscopy imaging," *Medical Image Analysis*, vol. 13, no. 1, pp. 167-179, 2009.
- [3] Xiaosong Yuan, Joshua T. Trachtenberg, Steve M. Potter, and Bradinath Roysam, "Mdl constrained 3-d grayscale skeletonization algorithm for automated extraction of dendrites and spines from fluorescence confocal images," *Neuroinformatics*, vol. 7, no. 4, pp. 213-232, 2009.
- [4] Yong Zhang, Xiaobo Zhou, Rochelle M. Witt, Bernardo L. Sabatini, Donald Adjero, and Stephen T.C. Wong, "Automated spine detection using curvilinear structure detector and lda classifier," in *Proc. of ISBI*, 2007, pp. 528-531.
- [5] Wengang Zhou, Houqiang Li, and Xiaobo Zhou, "3d dendrite reconstruction and spine identification," in *Proc. of MICCAI*, 2008, pp. 18-26.
- [6] Yong Zhang, Kun Chen, Matthew Baron, Merilee A. Teylan, Yong Kim, Zhihuan Song, Paul Greengard, and Stephen T.C. Wong, "A neurocomputational method for fully automated 3d dendritic spine detection and segmentation of medium-sized spiny neurons," *NeuroImage*, vol. 50, no. 4, pp. 1472-1484, 2010.
- [7] Peng Shi, Xiaobo Zhou, Qing Li, Matthew Baron, Merilee A. Teylan, Yong Kim, and Stephen T.C. Wong, "Online three-dimensional dendritic spines morphological classification based on semi-supervised learning," in *Proc. of ISBI*, 2009, pp. 1019-1022.
- [8] Alfredo Rodriguez, Douglas B. Ehlenberger, Dara L. Dickstein, Patrick R. Hof, and Susan L. Wearne, "Automated three-dimensional detection and shape classification of dendritic spines from fluorescence microscopy images," *PlosOne*, vol. 3, no. 4, 2007.
- [9] Winfried Denk and Heinz Horstmann, "Serial block-face scanning electron microscopy to reconstruct three-dimensional tissue nanostructure," *PLoS Biol*, vol. 2, no. 11, pp. 1900-1909, 2004.
- [10] Bo Zhang, Josiane Zerubia, and Jean-Christophe Olivo-Marin, "Gaussian approximations of fluorescence microscope psf models," *Applied Optics*, vol. 46, no. 10, pp. 1819-1829, 2007.
- [11] Warren R. Zipfel, Rebecca M. Williams, and Watt W. Webb, "Nonlinear magic: multiphoton microscopy in the biosciences," *Nature Biotechnology*, vol. 21, no. 11, pp. 1369 - 1377, 2003.

VII. References

- Aavula, B. R., M. A. Ali, et al. (2006). "Synthesis and fluorescence of N,N,N-trimethyl-2-[methyl (7-nitrobenzo[c][1,2,5]oxadiazol-4-yl) amino]ethanaminium iodide, a pH-insensitive reporter of organic cation transport." Synthetic Communications **36**(6): 701-705.
- Amaral, D. G. and M. P. Witter (1989). "The three-dimensional organization of the hippocampal formation: a review of anatomical data." Neuroscience **31**(3): 571-591.
- Araya, R., J. Jiang, et al. (2006). "The spine neck filters membrane potentials." Proceedings of the National Academy of Sciences of the United States of America **103**(47): 17961-17966.
- Arellano, J. I., R. Benavides-Piccione, et al. (2007). "Ultrastructure of dendritic spines: correlation between synaptic and spine morphologies." Frontiers in neuroscience **1**(1): 131-143.
- Bannister, N. J. and A. U. Larkman (1995). "Dendritic morphology of CA1 pyramidal neurones from the rat hippocampus: II. Spine distributions." The Journal of comparative neurology **360**(1): 161-171.
- Biess, A., E. Korkotian, et al. (2007). "Diffusion in a dendritic spine: the role of geometry." Physical review. E, Statistical, nonlinear, and soft matter physics **76**(2 Pt 1): 021922.
- Bliss, T. V. and T. Lomo (1973). "Long-lasting potentiation of synaptic transmission in the dentate area of the anaesthetized rabbit following stimulation of the perforant path." The Journal of physiology **232**(2): 331-356.
- Bloodgood, B. L., A. J. Giessel, et al. (2009). "Biphasic synaptic Ca influx arising from compartmentalized electrical signals in dendritic spines." PLoS biology **7**(9): e1000190.
- Bloodgood, B. L. and B. L. Sabatini (2005). "Neuronal activity regulates diffusion across the neck of dendritic spines." Science **310**(5749): 866-869.
- Bloodgood, B. L. and B. L. Sabatini (2007). "Ca(2+) signaling in dendritic spines." Current opinion in neurobiology **17**(3): 345-351.

- Bourne, J. N., K. E. Sorra, et al. (2007). "Polyribosomes are increased in spines of CA1 dendrites 2 h after the induction of LTP in mature rat hippocampal slices." Hippocampus **17**(1): 1-4.
- Burnashev, N., H. Monyer, et al. (1992). "Divalent ion permeability of AMPA receptor channels is dominated by the edited form of a single subunit." Neuron **8**(1): 189-198.
- Calabrese, B., M. S. Wilson, et al. (2006). "Development and regulation of dendritic spine synapses." Physiology **21**: 38-47.
- Campbell, R. E., O. Tour, et al. (2002). "A monomeric red fluorescent protein." Proceedings of the National Academy of Sciences of the United States of America **99**(12): 7877-7882.
- Chang, H. T. (1952). "Cortical neurons with particular reference to the apical dendrites." Cold Spring Harbor symposia on quantitative biology **17**: 189-202.
- De Simoni, A., C. B. Griesinger, et al. (2003). "Development of rat CA1 neurones in acute versus organotypic slices: role of experience in synaptic morphology and activity." The Journal of physiology **550**(Pt 1): 135-147.
- Deller, T., M. Korte, et al. (2003). "Synaptopodin-deficient mice lack a spine apparatus and show deficits in synaptic plasticity." Proceedings of the National Academy of Sciences of the United States of America **100**(18): 10494-10499.
- Denk, W. and H. Horstmann (2004). "Serial block-face scanning electron microscopy to reconstruct three-dimensional tissue nanostructure." PLoS biology **2**(11): e329.
- Denk, W., J. H. Strickler, et al. (1990). "Two-photon laser scanning fluorescence microscopy." Science **248**(4951): 73-76.
- Dillon, C. and Y. Goda (2005). "The actin cytoskeleton: integrating form and function at the synapse." Annual review of neuroscience **28**: 25-55.
- Ellis, R. J. (2001). "Macromolecular crowding: obvious but underappreciated." Trends in biochemical sciences **26**(10): 597-604.
- Fischer, M., S. Kaech, et al. (1998). "Rapid actin-based plasticity in dendritic spines." Neuron **20**(5): 847-854.
- Fromherz, P. and C. O. Muller (1994). "Cable properties of a straight neurite of a leech neuron probed by a voltage-sensitive dye." Proceedings of the National Academy of Sciences of the United States of America **91**(10): 4604-4608.

- Gahwiler, B. H., S. M. Thompson, et al. (2001). "Preparation and maintenance of organotypic slice cultures of CNS tissue." Current protocols in neuroscience / editorial board, Jacqueline N. Crawley ... [et al.] Chapter 6: Unit 6 11.
- Gamble, E. and C. Koch (1987). "The dynamics of free calcium in dendritic spines in response to repetitive synaptic input." Science **236**(4806): 1311-1315.
- Geiger, J. R., T. Melcher, et al. (1995). "Relative abundance of subunit mRNAs determines gating and Ca²⁺ permeability of AMPA receptors in principal neurons and interneurons in rat CNS." Neuron **15**(1): 193-204.
- Gray, E. G. (1959). "Electron microscopy of synaptic contacts on dendrite spines of the cerebral cortex." Nature **183**(4675): 1592-1593.
- Grunditz, A., N. Holbro, et al. (2008). "Spine neck plasticity controls postsynaptic calcium signals through electrical compartmentalization." The Journal of neuroscience : the official journal of the Society for Neuroscience **28**(50): 13457-13466.
- Harris, K. M. and J. K. Stevens (1988). "Dendritic Spines of Rat Cerebellar Purkinje-Cells - Serial Electron-Microscopy with Reference to Their Biophysical Characteristics." Journal of Neuroscience **8**(12): 4455-4469.
- Harris, K. M. and J. K. Stevens (1989). "Dendritic spines of CA 1 pyramidal cells in the rat hippocampus: serial electron microscopy with reference to their biophysical characteristics." The Journal of neuroscience : the official journal of the Society for Neuroscience **9**(8): 2982-2997.
- Harvey, C. D. and K. Svoboda (2007). "Locally dynamic synaptic learning rules in pyramidal neuron dendrites." Nature **450**(7173): 1195-1200.
- Heyman, N. S. and J. M. Burt (2008). "Hindered diffusion through an aqueous pore describes invariant dye selectivity of Cx43 junctions." biophysical journal **94**(3): 840-854.
- Holtmaat, A. J. G. D., J. T. Trachtenberg, et al. (2005). "Transient and persistent dendritic spines in the neocortex in vivo." Neuron **45**(2): 279-291.
- Kennedy, M. B., H. C. Beale, et al. (2005). "Integration of biochemical signalling in spines." Nature reviews. Neuroscience **6**(6): 423-434.
- Koch, C. and T. Poggio (1983). "A theoretical analysis of electrical properties of spines." Proceedings of the Royal Society of London. Series B, Containing papers of a Biological character. Royal Society **218**(1213): 455-477.

- Kornau, H. C., L. T. Schenker, et al. (1995). "Domain Interaction between Nmda Receptor Subunits and the Postsynaptic Density Protein Psd-95." Science **269**(5231): 1737-1740.
- Kugler, S., L. Meyn, et al. (2001). "Neuron-specific expression of therapeutic proteins: evaluation of different cellular promoters in recombinant adenoviral vectors." Molecular and cellular neurosciences **17**(1): 78-96.
- Kushmerick, M. J. and R. J. Podolsky (1969). "Ionic mobility in muscle cells." Science **166**(3910): 1297-1298.
- Lee, S. J. R., Y. Escobedo-Lozoya, et al. (2009). "Activation of CaMKII in single dendritic spines during long-term potentiation." Nature **458**(7236): 299-U258.
- Li, Z., K. Okamoto, et al. (2004). "The importance of dendritic mitochondria in the morphogenesis and plasticity of spines and synapses." Cell **119**(6): 873-887.
- Maeda, S. and T. Tsukihara (2011). "Structure of the gap junction channel and its implications for its biological functions." Cellular and molecular life sciences : CMLS **68**(7): 1115-1129.
- Major, G., A. U. Larkman, et al. (1994). "Detailed passive cable models of whole-cell recorded CA3 pyramidal neurons in rat hippocampal slices." The Journal of neuroscience : the official journal of the Society for Neuroscience **14**(8): 4613-4638.
- Man, H. Y., J. W. Lin, et al. (2000). "Regulation of AMPA receptor-mediated synaptic transmission by clathrin-dependent receptor internalization." Neuron **25**(3): 649-662.
- Markram, H., J. Lubke, et al. (1997). "Regulation of synaptic efficacy by coincidence of postsynaptic APs and EPSPs." Science **275**(5297): 213-215.
- Matsuzaki, M., G. C. R. Ellis-Davies, et al. (2001). "Dendritic spine geometry is critical for AMPA receptor expression in hippocampal CA1 pyramidal neurons." Nature Neuroscience **4**(11): 1086-1092.
- Mayer, M. L. (2011). "Structure and mechanism of glutamate receptor ion channel assembly, activation and modulation." Current opinion in neurobiology **21**(2): 283-290.
- Milani, H., U. U. Uemura, et al. (1998). "Loss of CA1 cells following global ischaemia correlates with spatial deficits in the circular platform task." Journal of neuroscience methods **80**(1): 19-27.

- Miyawaki, A. (2003). "Visualization of the spatial and temporal dynamics of intracellular signaling." Developmental cell **4**(3): 295-305.
- Murakoshi, H., H. Wang, et al. (2011). "Local, persistent activation of Rho GTPases during plasticity of single dendritic spines." Nature **472**(7341): 100-104.
- Neves, G., S. F. Cooke, et al. (2008). "Synaptic plasticity, memory and the hippocampus: a neural network approach to causality." Nature reviews. Neuroscience **9**(1): 65-75.
- Nitsche, J. M., H. C. Chang, et al. (2004). "A transient diffusion model yields unitary gap junctional permeabilities from images of cell-to-cell fluorescent dye transfer between *Xenopus* oocytes." Biophys J **86**(4): 2058-2077.
- Nitsche, J. M., H. C. Chang, et al. (2004). "A transient diffusion model yields unitary gap junctional permeabilities from images of cell-to-cell fluorescent dye transfer between *Xenopus* oocytes." biophysical journal **86**(4): 2058-2077.
- Nowak, L., P. Bregestovski, et al. (1984). "Magnesium gates glutamate-activated channels in mouse central neurones." Nature **307**(5950): 462-465.
- Nusser, Z., R. Lujan, et al. (1998). "Cell type and pathway dependence of synaptic AMPA receptor number and variability in the hippocampus." Neuron **21**(3): 545-559.
- Oertner, T. G. (2002). "Functional imaging of single synapses in brain slices." Experimental physiology **87**(6): 733-736.
- Palmer, L. M. and G. J. Stuart (2009). "Membrane potential changes in dendritic spines during action potentials and synaptic input." The Journal of neuroscience : the official journal of the Society for Neuroscience **29**(21): 6897-6903.
- Parpura, V., T. A. Basarsky, et al. (1994). "Glutamate-mediated astrocyte-neuron signalling." Nature **369**(6483): 744-747.
- Patterson, G. H. and J. Lippincott-Schwartz (2002). "A photoactivatable GFP for selective photolabeling of proteins and cells." Science **297**(5588): 1873-1877.
- Pologruto, T. A., B. L. Sabatini, et al. (2003). "ScanImage: flexible software for operating laser scanning microscopes." Biomedical engineering online **2**: 13.
- Popov, S. and M. M. Poo (1992). "Diffusional transport of macromolecules in developing nerve processes." The Journal of neuroscience : the official journal of the Society for Neuroscience **12**(1): 77-85.

- Racca, C., F. A. Stephenson, et al. (2000). "NMDA receptor content of synapses in stratum radiatum of the hippocampal CA1 area." The Journal of neuroscience : the official journal of the Society for Neuroscience **20**(7): 2512-2522.
- Reed, J. M. and L. R. Squire (1997). "Impaired recognition memory in patients with lesions limited to the hippocampal formation." Behavioral neuroscience **111**(4): 667-675.
- Rempel-Clower, N. L., S. M. Zola, et al. (1996). "Three cases of enduring memory impairment after bilateral damage limited to the hippocampal formation." The Journal of neuroscience : the official journal of the Society for Neuroscience **16**(16): 5233-5255.
- Ryu, J., L. Liu, et al. (2006). "A critical role for myosin IIb in dendritic spine morphology and synaptic function." Neuron **49**(2): 175-182.
- Sabatini, B. L., M. Maravall, et al. (2001). "Ca(2+) signaling in dendritic spines." Current opinion in neurobiology **11**(3): 349-356.
- Sabatini, B. L., T. G. Oertner, et al. (2002). "The life cycle of Ca(2+) ions in dendritic spines." Neuron **33**(3): 439-452.
- Santamaria, F., S. Wils, et al. (2006). "Anomalous diffusion in Purkinje cell dendrites caused by spines." Neuron **52**(4): 635-648.
- Schneider, M., S. Barozzi, et al. (2005). "Two-photon activation and excitation properties of PA-GFP in the 720-920-nm region." biophysical journal **89**(2): 1346-1352.
- Schuss, Z., A. Singer, et al. (2007). "The narrow escape problem for diffusion in cellular microdomains." Proceedings of the National Academy of Sciences of the United States of America **104**(41): 16098-16103.
- Segev, I. and W. Rall (1988). "Computational study of an excitable dendritic spine." Journal of neurophysiology **60**(2): 499-523.
- Sheng, M. and C. C. Hoogenraad (2007). "The postsynaptic architecture of excitatory synapses: a more quantitative view." Annual review of biochemistry **76**: 823-847.
- Shigemoto, R., A. Kinoshita, et al. (1997). "Differential presynaptic localization of metabotropic glutamate receptor subtypes in the rat hippocampus." The Journal of neuroscience : the official journal of the Society for Neuroscience **17**(19): 7503-7522.
- Soler-Llavina, G. J. and B. L. Sabatini (2006). "Synapse-specific plasticity and compartmentalized signaling in cerebellar stellate cells." Nature neuroscience **9**(6): 798-806.

- Spacek, J. and K. M. Harris (1997). "Three-dimensional organization of smooth endoplasmic reticulum in hippocampal CA1 dendrites and dendritic spines of the immature and mature rat." The Journal of neuroscience : the official journal of the Society for Neuroscience **17**(1): 190-203.
- Stepanyants, A., P. R. Hof, et al. (2002). "Geometry and structural plasticity of synaptic connectivity." Neuron **34**(2): 275-288.
- Steward, O. and W. B. Levy (1982). "Preferential localization of polyribosomes under the base of dendritic spines in granule cells of the dentate gyrus." The Journal of neuroscience : the official journal of the Society for Neuroscience **2**(3): 284-291.
- Svoboda, K. (2004). "Do spines and dendrites distribute dye evenly?" Trends in Neurosciences **27**(8): 445-446.
- Svoboda, K., D. W. Tank, et al. (1996). "Direct measurement of coupling between dendritic spines and shafts." Science **272**(5262): 716-719.
- Svoboda, K. and R. Yasuda (2006). "Principles of two-photon excitation microscopy and its applications to neuroscience." Neuron **50**(6): 823-839.
- Takumi, Y., V. Ramirez-Leon, et al. (1999). "Different modes of expression of AMPA and NMDA receptors in hippocampal synapses." Nature neuroscience **2**(7): 618-624.
- Tanaka, J., Y. Horiike, et al. (2008). "Protein synthesis and neurotrophin-dependent structural plasticity of single dendritic spines." Science **319**(5870): 1683-1687.
- Walikonis, R. S., O. N. Jensen, et al. (2000). "Identification of proteins in the postsynaptic density fraction by mass spectrometry." The Journal of neuroscience : the official journal of the Society for Neuroscience **20**(11): 4069-4080.
- Weber, P. A., H. C. Chang, et al. (2004). "The permeability of gap junction channels to probes of different size is dependent on connexin composition and permeant-pore affinities." Biophys J **87**(2): 958-973.
- Westrum, L. E. and T. W. Blackstad (1962). "An electron microscopic study of the stratum radiatum of the rat hippocampus (regio superior, CA 1) with particular emphasis on synaptology." The Journal of comparative neurology **119**: 281-309.
- Wilson, C. J. (1984). "Passive cable properties of dendritic spines and spiny neurons." The Journal of neuroscience : the official journal of the Society for Neuroscience **4**(1): 281-297.

- Yang, F., L. G. Moss, et al. (1996). "The molecular structure of green fluorescent protein." Nat Biotechnol **14**(10): 1246-1251.
- Yang, Y., W. Ge, et al. (2003). "Contribution of astrocytes to hippocampal long-term potentiation through release of D-serine." Proceedings of the National Academy of Sciences of the United States of America **100**(25): 15194-15199.
- Yasuda, R. and H. Murakoshi (2011). "The mechanisms underlying the spatial spreading of signaling activity." Current Opinion in Neurobiology **21**(2): 313-321.
- Yuste, R. and W. Denk (1995). "Dendritic Spines as Basic Functional Units of Neuronal Integration." Nature **375**(6533): 682-684.
- Zipfel, W. R., R. M. Williams, et al. (2003). "Nonlinear magic: multiphoton microscopy in the biosciences." Nature biotechnology **21**(11): 1369-1377.

VIII. List of abbreviations:

EPSP	Excitatory Postsynaptic Potential
IPSP	Inhibitory Postsynaptic Potential
AP	Action Potential
bAP	Back propagating Action Potential
PSD	Post Synaptic Density
AMPA	α -amino-3-hydroxy-5-methyl-4-isoxazolepropionate
NMDA	<i>N</i> -Methyl-D-aspartic acid or <i>N</i> -Methyl-D-aspartate
SER	Smooth Endoplasmic Reticulum
LTD	Long term depression
LTP	Long-term potentiation
VSCC	Voltage sensible calcium channel
ACSF	Artificial cerebrospinal fluid
DAB	Diaminobenzidine
NBD-MTMA	N,N,N-Trimethyl-2-[methyl(7-nitrobenzo[c][1,2,5]oxadiazol-4-yl)amino]ethanaminium Iodide
FRAP	fluorescence recovery after photo-bleaching
DRFI	Computation of Digitally Reconstructed Fluorescence Images
2PLPA	Two photon photoactivation
PA-GFP	Photoactivable GFP

IX. Table of figures

Figure I-1: The anatomy of the hippocampus.	8
Figure I-2. CA1 pyramidal cell.	9
Figure I-3:Chemical synapse	11
Figure I-4 3D reconstruction of dendrite from CA1 pyramidal cell.	13
Figure I-5:Some important components of dendritic spines.....	17
Figure I-6: Calcium transient in a dendritic spine of a CA1 pyramidal cell.	22
Figure III-1:Hippocampal slice cultures.	27
Figure III-2: One versus two photons fluorescence.	30
Figure III-3: Scheme of fluorescence detection system used in two-photon setup.	31
Figure III-4: Measuring diffusional coupling by bleaching spine head fluorescence.....	33
Figure III-5: Serial block face SEM.....	36
Figure III-6: Correlative between light and electron microscopy.....	39
Figure III-7: 3D EM reconstruction.....	41
Figure III-8: Volume reconstruction of dendritic structure from SBF-SEM raw data.	43
Figure III-9: Images used for computation of the DRFI.....	45
Figure III-10: Selection of spines to be measured.....	46
Figure III-11: Intensity measurement in two-photon or DRFI images.....	47
Figure IV-1: Measurement of Alexa 594 diffusion through the spine neck reveals heterogeneity of spine/dendrite diffusional coupling.	49
Figure IV-2: Correlative microscopy	51
Figure IV-3: Relationship between spine morphological variables and compartmentalization.	53
Figure IV-4: ratio spine head volume versus recovery time constant.	54
Figure IV-5: Measurement of coefficient of diffusion in dendrite.	57
Figure IV-6:Spine morphology predicts the movements of Alexa.	58
Figure IV-7: Correlation between Alexa and NBD-MTMA.....	61
Figure IV-8:Diffusion of large molecules can not be predicted from spine shape.	63
Figure IV-9: Spine neck resistance.	66

Figure IV-10: Simulated fluorescence images revealed increased concentration of particles inside dendritic spines.	68
Figure IV-11: Postsynaptic depolarization changes diffusional coupling between spine head and dendrite.	69
Figure IV-12: D_{alexa} is affected by strong depolarization of the neurons.	71
Figure V-1: New model of dendritic spine compartmentalization.	78
Figure VI-1: Scale of an ion and different fluorophores.	79
Figure VI-2: Two-photon excitation spectrum of NDB-MTMA.	80

X. Acknowledgments

I would like to thank my advisor Prof. Thomas Oertner, for giving me an exciting project, for his support, guidance during this time and for his help on this thesis.

Thanks to my committee member, Prof. Peter Scheiffele, Prof Michael Frotscher and Dr Rainer Friedrich for their scientific advices, critical discussions and helpful comments.

Thanks to Clemens Blumer for his collaboration on this project.

Thanks to Christel Genoud for her help with electron microscopy.

I would like to thank all past and present members of the Oertner laboratory for suggestions, comments, advices and especially Daniela Gerosa for the very nice cultures and Niklaus Holbro and Michael Avermann with who I enjoyed to share the rig.

I would like to specially thank my parents, my sister and Cella for their support and encouragement.

XI. Curriculum vitae

Name	Cyprien Vivien
Address	41 Ahornstrasse 4055 Basel
Phone	+41 (0)78 661 14 36
E-mail	cyprien.vivien@gmail.com
Nationality	French
Date of Birth	8 th of October 1982

Education

2008-2012	PhD in Neurobiology, Friedrich Miescher Institute in Basel, Switzerland.
2003-2007	Master of Science (biology), University of Caen, France.
2001-2003	Medical school, University of Caen, France.
1998-2001	High school, Scientific A-level , option physic-chemistry. La Ferte Mace, France.

Research experience.

2008-2012	PhD, Thomas Oertner's laboratory at the Friedrich Miescher Institute in Basel, Switzerland. Title/project: Study of dendritic spine compartmentalization, a correlative fluorescence light microscopy-electron microscopy approach.
2007-2008	Internship at Thomas Oertner's laboratory at the Friedrich Miescher Institute in Basel, Switzerland.
Feb.2007-oct.2008	MSc project, neuroscience, CINAPS institute, UMR CNRS 6232: Neurodegenerescence: models and therapeutic strategies.

Title/project: NMDA modulation by chronic disturbance of glutamatergic neurotransmission.

Information Technology

Programming languages: Matlab

Data and Mathematics

treatment tools: Matlab, Imaris,

Document edition Word, Excel, PowerPoint, Illustrator

Experimental, Technical experiences

Two-photon microscopy, electron microscopy, patch clamp.

Cellular and molecular biology; western blot, real-time PCR.

Cellular culture

Publications

Blumer, C. Vivien, T. G. Oertner, T. Vetter (2011) **Fluorescence image segmentation by using digitally reconstructed fluorescence images**. Proceedings of the Sixth Workshop on Microscopic Image Analysis with Applications in Biology (MIAAB 2011), Heidelberg.(peer reviewed)

Presentations

Vivien C., Genoud C., Frotscher M., Oertner T.G **Regulation of spine neck resistance** Amsterdam, Netherland: Forum of European Neuroscience, 2010. Online

Vivien C., Blumer C., Genoud C., Frotscher M., Vetter T., Oertner T.G **Compartmentalization inside dendritic spines**. Washington: Society for Neuroscience, 2011. Online

References :

- Pr Thomas Oertner
Friedrich Miescher Institute for Biomedical Research, Basel
Tel: (41) 6 16 97 82 73
Email: thomas.oertner@fmi.ch

- Pr Alain Buisson
Université de Caen-CNRS:UMR 6232 centre CINAPS
Tel : (33) 2 31 47 01 05
Email : buisson@cyceron.fr

- Olivier Nicole, PhD
CNRS :UMR 6232 centre CINAPS
Tel (33) 2 31 47 01 32
Email : nicole@cyceron.fr